

---

# Phase-Stabilized Dual-Comb Spectroscopy

Zaijun Chen

---



München 2019



---

# Phase-Stabilized Dual-Comb Spectroscopy

Zaijun Chen

---

Dissertation  
an der Fakultät für Physik  
der Ludwig-Maximilians-Universität  
München

vorgelegt von  
Zaijun Chen  
aus Guangdong

München, den 22.10.2019

Erstgutachter: Prof. Dr. Theodor W. Hänsch

Zweitgutachter: Prof. Dr. Wolfgang Zinth

Tag der mündlichen Prüfung: 10.12.2019

# Contents

Zusammenfassung	xi
Abstract	xii
<b>1 Introduction</b>	<b>1</b>
<b>2 Laser frequency comb and molecular spectroscopy</b>	<b>5</b>
2.1 Laser frequency comb . . . . .	5
2.1.1 Principle of laser frequency comb . . . . .	5
2.1.2 Molecular spectroscopy with laser frequency comb . . . . .	7
2.2 Dual-comb spectroscopy . . . . .	8
2.2.1 Principle of dual-comb spectroscopy . . . . .	8
2.2.2 Brief review of dual-comb spectroscopy . . . . .	11
2.2.3 Motivation of the work of this thesis . . . . .	12
<b>3 Feed-forward coherent dual-comb spectroscopy</b>	<b>15</b>
3.1 Background . . . . .	15
3.1.1 Phase noise perturbations . . . . .	15
3.1.2 Mutual coherence requirements . . . . .	17
3.2 Principle of feed-forward dual-comb spectroscopy . . . . .	19
3.2.1 Mutual coherence establishment . . . . .	19
3.2.2 Feed-forward control . . . . .	20
3.2.3 Dual-comb stabilization . . . . .	21
3.3 Experimental setup . . . . .	22
3.4 Experimental results . . . . .	24
3.4.1 Interferogram . . . . .	24
3.4.2 Feed-forward dual-comb spectra . . . . .	26
3.4.3 Assessment of the spectra . . . . .	29

---

3.5	Conclusion . . . . .	31
<b>4</b>	<b>Attenuated-total-reflectance dual-comb gas-phase spectroscopy</b>	<b>33</b>
4.1	Background . . . . .	34
4.1.1	Evanescent-wave sample interrogation . . . . .	34
4.1.2	Gas-phase attenuated-total-reflectance spectroscopy . . . . .	34
4.2	Principle . . . . .	35
4.2.1	Tapered-fiber evanescent waveguide . . . . .	35
4.2.2	Attenuated-total-reflectance spectroscopy . . . . .	37
4.3	Experimental setup . . . . .	38
4.4	Experimental results . . . . .	39
4.4.1	Dual-comb attenuated-total-reflectance spectra . . . . .	39
4.4.2	Analysis of molecules in small volumes . . . . .	43
4.5	Conclusion . . . . .	44
<b>5</b>	<b>Mid-infrared feed-forward dual-comb spectroscopy</b>	<b>47</b>
5.1	Background . . . . .	47
5.1.1	Challenges of mid-infrared dual-comb spectroscopy . . . . .	48
5.1.2	Current state of mid-infrared dual-comb spectroscopy . . . . .	48
5.2	Principle . . . . .	49
5.3	Experimental setup . . . . .	51
5.4	Experimental results . . . . .	52
5.5	Conclusion and discussion . . . . .	59
<b>6</b>	<b>Summary and Outlook</b>	<b>61</b>
<b>A</b>	<b>Appendix Figures</b>	<b>65</b>
<b>B</b>	<b>Appendix Tables</b>	<b>75</b>
	<b>Bibliography</b>	<b>85</b>
	<b>List of Publications</b>	<b>98</b>
	<b>Conference Contributions</b>	<b>101</b>
	<b>Acknowledgements</b>	<b>103</b>

# List of Figures

2.1	Time- and frequency-domain representation of a frequency comb. . . . .	6
2.2	Principle of dual-comb spectroscopy. . . . .	9
3.1	Simulation of averaging dual-comb interferograms. . . . .	18
3.2	Scheme of mutual coherence establishment. . . . .	19
3.3	Feed-forward control of the carrier-envelope offset frequency of a frequency comb. . . . .	20
3.4	Feed-forward dual-comb stabilization. . . . .	21
3.5	Experimental setup of near-infrared feed-forward dual-comb spectroscopy. .	23
3.6	Experimental near-infrared feed-forward dual-comb interferogram. . . . .	25
3.7	Experimental dual-comb spectrum around 190 THz with a resolution of 100 MHz. . . . .	26
3.8	Experimental spectrum around 190 THz with resolved comb lines. . . . .	28
3.9	Evolution of the average signal-to-noise ratio in the near-infrared feed-forward dual-comb spectra with the measurement time. . . . .	29
3.10	Near-infrared acetylene experimental transmittance spectrum and its fitted result. . . . .	30
4.1	Schematic configurations of sample interrogation with attenuated-total-reflectance spectroscopy. . . . .	34
4.2	Intensity distribution of the guided fundamental mode at the cross-section of a fused-silica fiber in the vacuum. . . . .	36
4.3	Experimental setup of dual-comb attenuated-total-reflectance gas-phase spectroscopy. . . . .	38
4.4	Experimental dual-comb attenuated-total-reflectance spectrum in the region of the $2\nu_3$ band of $^{12}\text{CH}_4$ . . . . .	40
4.5	Characterization of the dual-comb attenuated-total-reflectance spectrum. .	41
4.6	Dual-comb attenuated-total-reflectance spectrum with resolved comb lines.	42

4.7	Dual-comb attenuated-total-reflectance spectrum in the region of $\nu_1 + \nu_3$ absorption band of $^{12}\text{C}_2\text{H}_2$ with low gas pressure. . . . .	44
5.1	Scheme of mid-infrared feed-forward dual-comb spectroscopy. . . . .	50
5.2	Principle of difference frequency generation between a single-frequency laser and a frequency comb. . . . .	50
5.3	Experimental setup of mid-infrared feed-forward dual-comb spectroscopy. .	51
5.4	Feed-forward mid-infrared dual-comb interferogram. . . . .	54
5.5	Experimental mid-infrared dual-comb spectrum at around 92 THz with resolved comb lines. . . . .	55
5.6	Experimental spectrum in the region of the $\nu_9$ and $\nu_{11}$ fundamental bands of $^{12}\text{C}_2\text{H}_4$ around 92 THz. . . . .	56
5.7	Experimental spectrum in the region of the $\nu_3$ fundamental band of $^{12}\text{C}_2\text{H}_2$ with a resolution of 100 MHz. . . . .	57
5.8	Evolution of the average signal-to-noise ratio in the experimental mid-infrared dual-comb spectra over 2,000 s. . . . .	58
5.9	Experimental transmittance spectrum of ethylene and the fitted molecular profiles. . . . .	59
A.1	Spectral broadening of an erbium comb in a highly nonlinear fiber. . . . .	65
A.2	Radio-frequency power spectrum of the phase-locked in-loop beat signals. .	66
A.3	Experimental feed-forward dual-comb spectrum in the 180-THz region with a resolution of 100 MHz. . . . .	67
A.4	Experimental dual-comb spectra with resolved comb lines in the region of the $2\nu_3$ band of $^{12}\text{CH}_4$ around 180 THz. . . . .	68
A.5	The fraction $\eta(f)$ of the total intensity propagating in the evanescent field.	69
A.6	Penetration depth of the evanescent field around a tapered fiber at different guided laser frequencies. . . . .	70
A.7	Dual-comb attenuated-total-reflection spectrum at around 225 THz with the $\nu_2 + 2\nu_3$ band of $\text{CH}_4$ . . . . .	71
A.8	Results of mid-infrared frequency comb generation. . . . .	72
A.9	Mid-infrared dual-comb spectrum with resolved comb lines in the region of the $\nu_3$ band of $^{12}\text{C}_2\text{H}_2$ around 98 THz. . . . .	73

# List of Tables

B.1	Experimental center frequencies of the molecular lines in the $\nu_1 + \nu_3$ band of $^{12}\text{C}_2\text{H}_2$ . . . . .	76
B.2	Line center positions of the $2\nu_3$ band of $^{12}\text{CH}_4$ . . . . .	77
B.3	Line positions of the $\nu_9$ band of $^{12}\text{C}_2\text{H}_4$ . . . . .	78
B.4	Experimental line center positions of the $\nu_{11}$ band of Ethylene ( $^{12}\text{C}_2\text{H}_4$ ) . .	82
B.5	Line center positions of the $\nu_2 + \nu_{12}$ band of Ethylene ( $^{12}\text{C}_2\text{H}_4$ ) . . . . .	84
B.6	List of line positions of the $2\nu_{10} + \nu_{12}$ band of Ethylene ( $^{12}\text{C}_2\text{H}_4$ ). . . . .	84



# Zusammenfassung

Optische Frequenzkämme zeichnen sich durch ihre phasenkohärenten, äquidistanten Laserlinien im Spektrum aus. Gegenwärtig werden sie unter anderem neben ihrem ursprünglichen Verwendungszweck für Frequenzmessungen verwendet. Molekulare Spektroskopie profitiert von der großen spektralen Bandbreite. Die hier vorliegende Arbeit trägt zum Fortschritt von Zwei-Kamm-Spektroskopie bei, einer frequenzkammbasierten Spielart der Fourierinterferometrie ohne bewegliche Teile.

Zwei-Kamm-Spektroskopie beruht darauf, Interferenzen in der Zeit-Domäne zwischen zwei Frequenzkämmen mit gering voneinander abweichenden Wiederholraten zu messen. Die Fouriertransformierte des Interferenzmusters spiegelt dabei das Spektrum wider. Die Technik erfordert den kohärenten Betrieb zwischen beiden Frequenzkämmen über die Dauer der Messung. In dieser Arbeit wird eine neue Technik dafür vorgestellt, die auf feed-forward Kontrolle der Differenz im Versatz der Trägerwellenfrequenzen, welche oftmals das hochfrequente Rauschen der Frequenzgeneratoren tragen. Wir zeigen die Möglichkeit, im nahinfraroten Bereich durch direkte Mittelung Interferogramme mit über 2 000 Sekunden Messzeit ohne Abstriche beim Signal-zu-Rausch-Verhältnis und ohne analoge oder digitale Datenkorrektur zu erhalten. Dadurch ergibt sich eine Verbesserung von drei Größenordnungen gegenüber den vormals besten Methoden direkter Mittelung, was eine verbesserte Kontrolle systematischer Effekte bedeutet. Die Ergebnisse konnten durch doppler-verbreiterte Spektrum der  $\nu_1 + \nu_3$ -Kombination an gasförmigem Acetylen validiert werden.

Wir verwenden das entwickelte nahinfrarote Spektrometer, um Spektrope durch abgeschwächte Totalreflexion an Gasphasen zu demonstrieren. Wir benutzen dabei die Wechselwirkung des evaneszenten Feldes an gezogenen Fasern mit wenigen Molekülen, um Gasvolumina von wenigen Zehn Pikolitern zu untersuchen. Die hohe Auflösung sowie die große spektrale Bandbreite durch Zwei-Kamm-Spektroskopie bleibt dabei erhalten.

Wir erweitern die Technik von vorwärtsgerichteten Zwei-Kamm-Spektroskopie in die mittlere Infrarotregion von  $3 \mu\text{m}$ , in der fundamentale Streckschwingungen von CH-, NH- und OH-Gruppen in Molekülen zu finden sind. Anhand von Spektren der  $\nu_9/\nu_{11}$ -dyad von Ethylen demonstrieren wir die gleichen Fähigkeiten des Mitteln von Interferogrammen über einen Zeitraum einer halben Stunden wie im Nahinfrarotbereich. Die Spektren haben eine Frequenzskala, die direkt an einem Wasserstoff-Maser kalibriert wurde mit einer instrumentellen Linienbreite, die drei Größenordnungen schmalbandiger ist als durch Dopplerverbreiterung gegebene Linienbreiten kleiner Moleküle bei Raumtemperatur. Diese Ergebnisse ermöglichen die präzise Bestimmung von spektralen Linien und deren Form in der mittleren Infrarotregion.

# Abstract

Optical frequency combs are spectra of phase-coherent evenly spaced laser lines. They currently find applications beyond their initial purpose, frequency metrology. They advance techniques of molecular spectroscopy over broad spectral bandwidths. This thesis is a contribution to the progress of dual-comb spectroscopy, a comb-based technique of Fourier transform interferometry without moving parts.

Dual-comb spectroscopy relies on measuring the time domain interference between two frequency combs of slightly different repetition frequencies. The Fourier transform of the interference pattern reveals the spectrum. The technique implies maintaining coherence between the two frequency combs over the time of a measurement. Here, a new technique for achieving this objective is explored: it is based on feed-forward control of the difference in carrier-envelope offset frequencies of the combs, which often carry the high-frequency noise of the synthesizers. In the near-infrared region, we show the possibility to directly average the time-domain interferograms over 2,000 seconds without any loss in signal-to-noise ratio and without any analog or digital corrections to the data. This represents an improvement of three orders of magnitude over the previous best direct averaging capabilities and this may therefore enable a better control of systematic effects. These developments are validated with Doppler-broadened spectra of the  $\nu_1+\nu_3$  combination band of gaseous acetylene.

We use the developed near-infrared spectrometer to demonstrate gas-phase attenuated-total-reflectance spectroscopy over broad spectral bandwidths. We use the interaction of the evanescent wave at a fiber taper with small molecules to interrogate gas volumes as little as a few tens of picoliters. The features of high resolution and broad spectral bandwidth brought by dual-comb spectroscopy are preserved.

We extend the technique of feed-forward dual-comb spectroscopy to the mid-infrared 3- $\mu\text{m}$  region, where the fundamental CH, NH, OH stretches in molecules are found. With spectra of the  $\nu_9/\nu_{11}$  dyad of ethylene, we demonstrate the same capabilities of averaging interferograms during half-an-hour as in the near-infrared. The spectra have a frequency scale directly calibrated to a hydrogen maser, an instrumental line shape that is three orders of magnitude narrower than the Doppler width of small molecules at room temperature. These results open up the prospect of precise determination of line positions and line shapes in the mid-infrared range.

# Chapter 1

## Introduction

Each molecule has characteristic absorptions, which allow one to unambiguously identify the species and quantify its abundance, and to reveal its physical properties including structure and dynamics. Such molecular fingerprints can be measured, e.g., with the intensity of light transmitted through a sample as a function of its frequency in the electromagnetic spectrum [1]. The spectra of molecules provide rich information for the studies relevant to fundamental or applied molecular science. For instance, precise frequency measurements in simple molecules enable tests of fundamental laws of physics [2], while broadband analysis of complex spectra of large molecules enhances our understanding of their vibrational and rotational motions [3]. Various techniques of molecular spectroscopy have been developed to improve the spectral accuracy, resolving power, spectral coverage, and measurement speed, etc. However, trade-offs occur and each technique has its own range of applications. Breakthroughs rely on new light sources, new concepts of instruments and new measurement techniques.

Laser frequency combs, as developed in the late 90s, have enabled optical frequency metrology [4, 5]. As a broadband spectrum composed of millions of discrete, equally-spaced, and phase-coherent laser lines, a frequency comb offers a link between optical- and radio-frequencies, enabling optical frequency measurements across their spectral span with an accuracy set by a radio-frequency atomic clock. Beyond the initial motivation of precision spectroscopy [6] and optical frequency measurements [7], frequency combs have found a variety of intriguing yet unforeseen applications, such as calibration of astronomical spectrographs [8], synthesis of optical arbitrary waveforms [9], and generation of attosecond pulses [10], etc.

For over a decade, frequency combs have been utilized to measure complex molecular spectra [11], in schemes where they interrogate a large number of transitions directly and

simultaneously. Among the various techniques developed for frequency comb spectroscopy [12–20], the dual-comb scheme has attracted considerable interest in recent years. Dual-comb spectroscopy exploits the time-domain interference of two laser frequency combs of slightly different repetition frequencies. Based on Fourier transform interferometry, it measures all the spectral elements simultaneously using a single detector; without moving parts, it potentially enables rapid, high-resolution and precise measurements over broad spectral ranges.

With these prospects, the dual-comb technique holds much promise to improve the performance of spectroscopic measurements; however, most of the time in practice, the quality of the dual-comb spectra fails in many aspects to compete with those recorded with, e.g., scanning Michelson Fourier spectrometers, for which the technique has been perfected over decades [21]. Several fundamental challenges had been hampering the development of dual-comb spectroscopy at the time when this thesis started. The work in this thesis tackles some of the difficulties of dual-comb instrumentation. The advantages of our techniques are exploited for molecular spectroscopy.

Before getting into the work of this thesis, **Chapter 2: Laser frequency comb and molecular spectroscopy** introduces the fundamental principle of frequency combs and their applications in broadband molecular spectroscopy. A brief review of dual-comb spectroscopy provides the background to this thesis.

The main accomplishments of the work in this thesis are divided into three chapters (Chapter 3-5):

**Chapter 3: Feed-forward coherent dual-comb spectroscopy** deals with the essential challenge of dual-comb instrumentation. As a two-beam interferometer, the phase difference in a dual-comb system is automatically scanned by means of two asynchronous trains of laser pulses. Therefore preserving the mutual coherence between the two pulse trains over the experimental times is a key requirement—this implies that the relative timing and phase fluctuations of the two combs should be precisely controlled. If this requirement is not achieved, relative phase variations result in chromatic distortions and decrease of signal-to-noise ratio and resolution, preventing precise quantitative analysis. Before this thesis, a mutual coherence time between the two combs of 1 s had been reached [22]. Longer measurement times relied on numerical phase correction techniques, which often lead to artifacts and worsened precision. In this thesis, an original dual-comb scheme [23], based on feed-forward relative stabilization of the carrier-envelope frequencies of the two combs, is proposed and demonstrated to establish such a coherence. An illustration of phase-stabilized dual-comb spectroscopy is provided with two spectrally broadened mode-

---

locked erbium-fiber laser combs in the near-infrared region.

**Chapter 4: Attenuated-total-reflectance dual-comb gas-phase spectroscopy** explores the potential of dual-comb spectroscopy for analyzing gas molecules of small amounts. Attenuated-total-reflectance spectroscopy harnesses sample interaction with evanescent waves, which form when the light experiences an internal total reflection in a medium. With a characteristic penetration depth on the micrometer scale, the evanescent waves provide a unique platform to study molecular samples with interrogation volumes below a nanolitre [24]. This sampling technique is widely used in analytical spectroscopy of condensed-phase samples. However, extending it to broadband analysis of multiple gas-phase absorbers has never been performed to our knowledge because combining a broadband spectrometer with an long internal reflection element for high-resolution gas-phase measurements is instrumentally challenging. So far, almost all the realizations of gas-phase attenuated-total-reflectance spectroscopy are based on tunable continuous-wave laser spectroscopy with a narrow spectral bandwidth targeting a few transitions of a gas species [25–27]; their capability of simultaneously diagnosing various molecules or complex mixtures is limited. In this chapter, the performance of feed-forward dual-comb spectrometer is exploited for attenuated-total-reflectance spectroscopy in gas-phase molecules over broad spectral bandwidth.

**Chapter 5: Mid-infrared feed-forward dual-comb spectroscopy** performs phase-stabilized broadband dual-comb spectroscopy in the mid-infrared region. Laser frequency comb technology is well-developed in the near-infrared region; as a result, dual-comb spectroscopy has been mostly demonstrated on the overtone transitions in this domain. However, the fundamental molecular ro-vibrational transitions are located in the mid-infrared range. Their absorption cross-section is typically one or two orders of magnitude larger than that of the overtone transitions, which leads to improvements of detection sensitivity. The Michelson-based Fourier spectrometer is currently a common option for mid-infrared broadband molecular spectroscopy; however, they often harness a mechanical scanning arm in combination with an incoherent light source of low brilliance, and consequently they are slow for high-resolution measurements. Dual-comb spectrometers hold potential for technical improvements in this region. Yet, their implementation still encounters multiple complications due to the complex laser systems and the difficulty of maintaining the relative phase stability of the two combs. In this chapter, the feed-forward dual-comb technique is extended to provide a solution to mid-infrared dual-comb spectroscopy, with a demonstration in the important  $3\text{-}\mu\text{m}$  spectral window.

**Chapter 6: Summary and Outlook** concludes the main findings and discusses the prospects of this thesis.

# Chapter 2

## Laser frequency comb and molecular spectroscopy

This chapter introduces some fundamental concepts and principles of laser frequency combs and their applications in broadband molecular spectroscopy. The technique of dual-comb spectroscopy is illustrated in detail, with a brief review providing the background and motivation for this thesis.

### 2.1 Laser frequency comb

#### 2.1.1 Principle of laser frequency comb

An optical frequency comb can be produced by a train of short laser pulses, for instance, emitted by a mode-locked laser [4, 5, 28]. The pulse train output from a laser cavity (Figure 2.1) has a repetition rate  $f_r = c/(2L)$ , corresponding to the inverse of the cavity round-trip time, where  $c$  is the speed of the light and  $L$  is the cavity length. The dispersion in the cavity induces a pulse-to-pulse phase slippage  $\Delta\varphi$  of the carrier wave relative to the pulse envelope, which shifts the comb spectrum from the harmonic frequencies of  $f_r$  by an amount called carrier-envelope offset frequency  $f_{ce} = f_r\Delta\varphi/2\pi$ . As a result, the frequencies in a frequency comb can be determined by two degrees of freedom: the repetition frequency  $f_r$  and the carrier-envelope offset frequency  $f_{ce}$ . The frequency of the  $n$ -th comb line can be written as

$$f_n = nf_r + f_{ce}, \quad (2.1)$$

where  $n$  is an integer usually on the order of  $10^6$ .

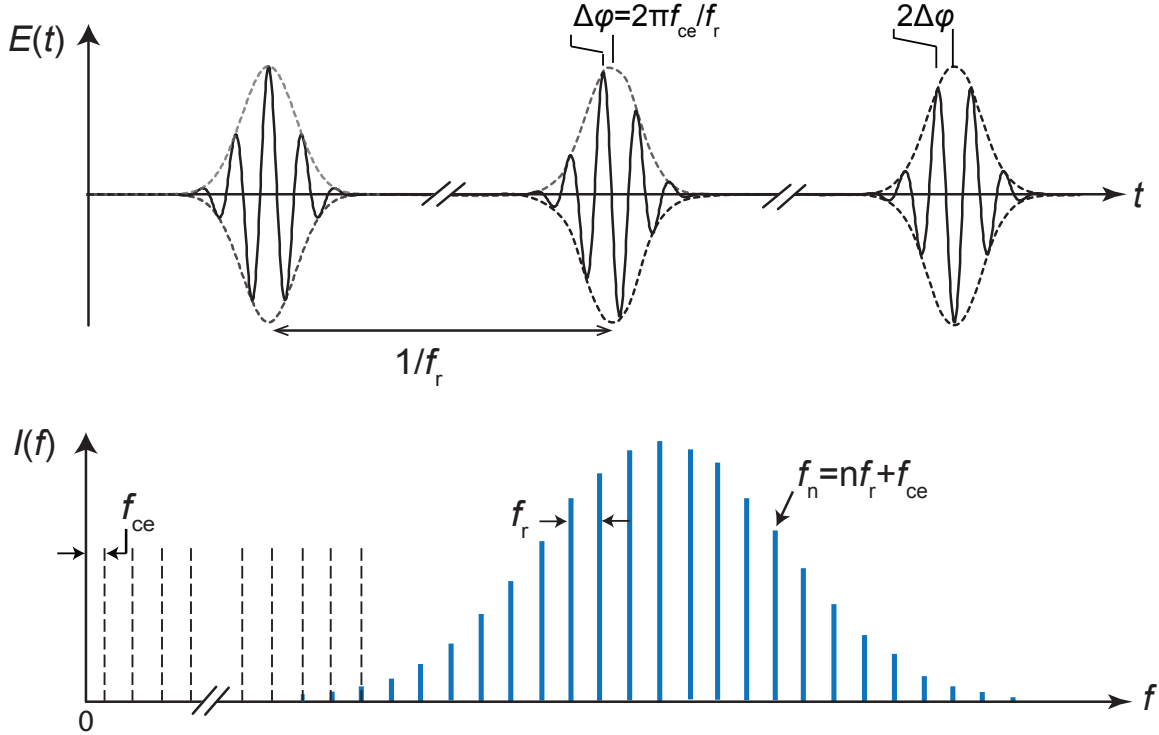


Figure 2.1: Time- and frequency-domain representation of a frequency comb.

In reality, the frequency comb sources are perturbed by different kinds of noise (the noise sources and the consequent phase fluctuations in mode-locked laser frequency combs will be discussed in Chapter 3), which lead to fluctuations of  $f_r$  and  $f_{ce}$ . For realizing a frequency comb, these two degrees of freedom ( $f_r$  and  $f_{ce}$ ) should be detected and stabilized. The pulse repetition frequency  $f_r$ , which is usually in the radio-frequency range (e.g., on the order of tens of MHz to several GHz), can be monitored directly with a fast photodetector. On the other hand, accessing the carrier-envelope offset frequency  $f_{ce}$  is not as straightforward because it involves interferometric measurements. This complication was overcome, e.g., with the frequency comb self-referencing technique using an octave-spanning comb, where the  $f_{ce}$  can be measured with an  $f-2f$  interferometer [4, 28]. Once  $f_r$  and  $f_{ce}$  are both detected, they can be stabilized to a radio-frequency or microwave clock with phase-lock loops and counted precisely with electronic instruments, so the frequency of the  $n$ -th comb lines can be known with Eq. 2.1. Therefore, the frequency comb can directly compare a radio-frequency (or microwave) to an optical one, enabling optical frequency metrology with high precision.

Frequency combs were initially realized with Kerr-lens mode-locked Ti-sapphire laser sources with a spectrum across the visible and near-infrared regions [4, 5]. Now the mode-

locked laser sources have become more reliable and compact in the near-infrared region. For instance, fiber lasers (e.g., with all polarization-maintaining fibers based on passive mode-locking using a saturable absorber [29]), are highly robust and becoming widespread. Doped with a different active medium, e.g., ytterbium, erbium, or thulium, they emit around  $1.0\ \mu\text{m}$ ,  $1.5\ \mu\text{m}$ , and  $2.2\ \mu\text{m}$ , respectively. Benefiting from the high peak power of the short laser pulses in nonlinear frequency conversion and supercontinuum generation, the frequency combs have been extended to wide spectral regions of interest, for instance, extreme ultraviolet [30][31], mid-infrared [32], and terahertz regions [33].

### 2.1.2 Molecular spectroscopy with laser frequency comb

Laser frequency combs has been initially developed for optical frequency metrology, permitting absolute frequency measurements over the entire optical spectrum. Now they are widely used as precise measurement tools, enabling new applications [34]. For broadband molecular spectroscopy, the frequency combs are harnessed to interrogate a vast number of transitions simultaneously, providing technical improvements and new spectroscopic approaches [11]. In general, independently from the spectroscopic techniques, when the resolution of the spectrometer is sufficient to resolve the individual comb lines, the frequency scale of the spectrum can be calibrated within the accuracy of an atomic clock (e.g., with a fractional instability of  $10^{-13}$  at 1 s [23]). The spectral resolution is limited by the spacing of the comb lines  $f_r$  (e.g., 100 MHz); using spectral interleaving with stepped  $f_{ce}$  or  $f_r$  [35], the resolution can be improved to below  $f_r$ , and ultimately it is limited only by the intrinsic width of the comb lines. Moreover, different from other spectroscopic techniques, where the instrumental line shape that convolves the molecular lines is often of similar width of the transitions, in frequency-comb spectrometers, the width of the instrumental line shape may be determined by the width of the individual comb lines. At best, its contribution to the molecular profiles is negligible when the comb-line width is several orders of magnitude narrower than the width of Doppler-broadened transitions.

Diverse spectroscopic techniques have been developed to reveal the spectral content of the frequency combs, permitting high-precision molecular spectroscopy over a broad bandwidth.

Several techniques based on dispersive spectroscopy are developed, for instance, using Vernier spectrometers [14], cross dispersers with virtually imaged phased array etalons [15], and fiber spectrometers [20]. These techniques rarely allow to resolve the comb lines [14, 15, 20] because geometric limitations occur, e.g., a long dispersing distance is required for establishing a high spectral resolution, and a large amount of pixels in the detector array

is demanded for simultaneous acquisitions of an increasing number of spectral elements, etc. Besides, performing these techniques in the mid-infrared molecular fingerprint region is complicated because the detector arrays or cameras are not as advanced as those in the near-infrared or the visible regions.

A different path to broadband frequency comb spectroscopy is yielded by Fourier transform spectroscopy. With a setup based on a Michelson interferometer, the Fourier spectrometers are highly multiplexed and widely used in molecular spectroscopy [36]. With all the spectral elements measured simultaneously using a single photo-detector, they are compatible with any light sources and implementable in any spectral regions. In a scanning Michelson interferometer, e.g., using a monochromatic light source with frequency  $f$ , owing to the Doppler effect, the frequency of the light in the moving arm is shifted by an amount  $-2fv/c$ , where  $v$  is the velocity of the moving mirror. The interference is recorded as a function of the optical delay between the two arms, and the spectrum is revealed by Fourier analysis. The optical spectrum is down-converted by a factor of  $c/(2v)$  to the audio-frequency range. Frequency combs have been harnessed as light sources in Michelson interferometers [3, 16, 37], providing Fourier transform spectroscopy with absolute frequency calibration and signal-to-noise-ratio improvements. However, the spectral resolution of the Michelson interferometers is determined by the maximum path difference of the two arms (e.g., 3 m is required for a resolution of 100 MHz), therefore achieving a high resolution usually trades off the compactness of the instrument. Besides, the scanning speed of the moving mirror must be restricted for avoiding spectral artifacts, thus the data refreshing rate is limited.

As the major shortcomings of the Michelson-based Fourier spectrometers are related to the mechanical parts which induce the optical delays of the two arms, a way to perform Fourier transform interferometry without moving parts is to use a dual-comb interferometer [12, 17, 18]; harnessing the interference of two frequency combs of slightly different repetition rates, the optical delays are automatically scanned. As dual-comb spectroscopy is the main topic of this thesis, this technique will be discussed in detail next.

## 2.2 Dual-comb spectroscopy

### 2.2.1 Principle of dual-comb spectroscopy

A simplified optical layout of a dual-comb spectrometer is depicted in Fig. 2.2a. Two frequency combs of slightly different repetition frequencies are utilized. One comb interacts with the sample. The two combs are overlapped with a beam splitter and beat onto

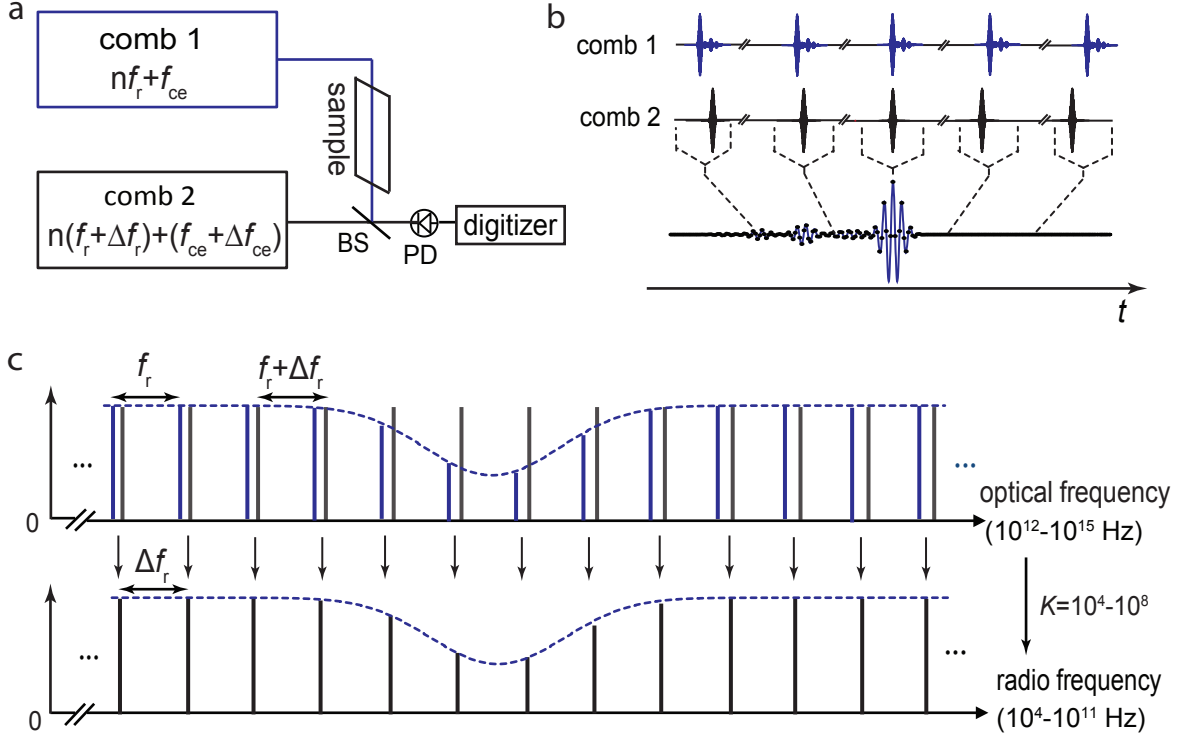


Figure 2.2: **Principle of dual-comb spectroscopy.** **a.** A simplified setup of dual-comb spectroscopy. BS: beamsplitter, PD: photodetector. **b–c.** Time- and frequency- domain picture of dual-comb spectroscopy.

a photodetector. In the time domain (Figure 2.2b), the pulse train of comb 1 excites the molecular free-induction decay. The comb 2, emitting pulses with a slightly different repetition rate, scans the decay with a linear optical delay increment; the interference of two combs results in a dual-comb interferogram, which is similar to the interferogram acquired with a scanning Michelson interferometer, except that the optical delays are automatically induced without moving parts.

The repetition frequency and carrier-envelope frequency of the comb 1 and the comb 2, are  $f_r$  and  $f_{ce}$ , respectively, and  $f_r + \Delta f_r$  and  $f_{ce} + \Delta f_{ce}$ , respectively. The sample introduces an attenuation  $\exp(-\alpha_n)$  and a phase shift  $\exp(-i\phi_n)$  to the electric field of the  $n$ -th comb line of the comb 1. The electric field of each comb can be written as

$$E_1(t) = \sum_n A_{1,n} \exp[-(\alpha_n + i\phi_n)] \exp[-i2\pi(nf_r + f_{ce})t] + c.c., \quad (2.2)$$

$$E_2(t) = \sum_n A_{2,n} \exp[-i2\pi[n(f_r + \Delta f_r) + (f_{ce} + \Delta f_{ce})]t] + c.c., \quad (2.3)$$

where  $A_{1,n}$ , and  $A_{2,n}$  denote the amplitude of the  $n$ -th comb mode of the comb 1 and

comb 2, respectively. *c.c.* denotes the complex conjugate. The interference of the two combs on the detector is

$$S(t) \propto [E_1(t) + E_2(t)] \times [E_1(t) + E_2(t)]^*. \quad (2.4)$$

This signal contains many mixing terms, including the the high-order harmonic and the sum-frequency terms. We only consider the term at the lowest frequency, which corresponds to the beat of pairs of neighboring comb lines, one line from each comb (e.g., with the same mode number). It can be isolated from  $S(t)$  by implementing a low-pass electronic filter. The resulting dual-comb interferogram is,

$$I(t) = \sum_n A_{1,n} A_{2,n}^* \exp[-(\alpha_n + i\phi_n)] \exp[-i2\pi(n\Delta f_r + \Delta f_{ce})t] + c.c.. \quad (2.5)$$

A complex Fourier transform on  $I(t)$  reveals the amplitude and phase of the dual-comb spectrum,

$$B(f) = \sum_n A_{1,n} A_{2,n}^* \exp[-(\alpha_n + i\phi_n)] \delta[f - (n\Delta f_r + \Delta f_{ce})] + c.c., \quad (2.6)$$

where  $\delta(f)$  is a Dirac delta function. The absorption and dispersion of the sample can be retrieved from the spectrum.

The principle of dual-comb spectroscopy can be interpreted in the frequency domain, as shown in Figure 2.2c. The multi-heterodyne beat of pairs of comb lines of the two optical combs, with a repetition frequency  $f_r$  and  $f_r + \Delta f_r$ , respectively, leads to a radio-frequency comb with a line spacing of  $\Delta f_r$  (Eq. 2.6). The molecular absorption is converted to the radio-frequency domain, where the signal can be detected and digitized. With the knowledge of the comb parameters, the radio-frequency spectrum can be rescaled to the optical domain unambiguously. A down-conversion factor  $K = f_r / \Delta f_r$  links the optical scale and the radio-frequency scale. An optical comb with a span  $W$  is mapped down to the radio-frequency span of  $W/K$ , which should be kept smaller than the radio-frequency free spectral range  $f_r/2$  for avoiding aliasing, thus the difference of the repetition frequencies of the two combs should be chosen  $\Delta f_r < f_r^2 / (2W)$ .

To sum up, harnessing Fourier transform spectroscopy without moving parts, the dual-comb spectrometer potentially permits measurements with resolved comb lines in any spectral ranges that the frequency combs reach, providing self-calibration to the frequency scale and broad spectral bandwidth. Compared to the dispersive methods of frequency comb spectroscopy, the dual-comb technique records all the spectral elements simultaneously

with a single fast photodetector; without the geometric limitations, it theoretically enables unlimited spectral spans and resolutions. Different from the scanning Michelson interferometers, the optical delay between pairs of pulses in the dual-comb interferometers is induced with a static device; therefore, its resolution and measurement speed are not limited by moving parts.

### 2.2.2 Brief review of dual-comb spectroscopy

The first interferometry harnessing the interference of two frequency combs of slightly different repetition frequencies was exploited for rapid-scanning optical coherence tomography in 2001 [38], and its implementation for Fourier spectrometer was demonstrated with free-running combs in 2004 [12]. Then the potential of dual-comb spectroscopy has been explored by a series of work of linear [17, 18] and nonlinear spectroscopy [35, 39–41]. In recent years, this technique has attracted the interest of dozens of research groups. Several comprehensive reviews [11, 32, 42, 43] cover different aspects of this active field. A brief review introducing the background of this thesis is provided here.

The first challenge to dual-comb spectroscopy is to avoid the spectral distortions resulting from the relative phase instabilities between the two combs; similar to any two-beam interferometer, the temporal coherence between the the electric field of the two beams should be maintained over the time of a measurement. In the near-infrared spectral range, several dual-comb techniques have been implemented to preserve [22, 44] or reconstruct [45–49] the phase scans. A powerful approach is to lock the two frequency combs to a pair of cavity-stabilized continuous-wave lasers of Hertz linewidth, where the mutual coherence time achievable is given by the inverse linewidth of the continuous-wave lasers, on the order of 1 s. The measurement time can be extended to tens of minutes with phase correction [22]. Alternatively, various schemes correcting phase errors based on digital processing [45, 46], analog electronics [48], or computer algorithm [49] were developed, permitting dual-comb measurements even with free-running combs. A third trend is to build systems with passive mutual coherence, e.g., with electro-optic modulators (EOM) [50, 51] or with two frequency-comb lasers emitting from a shared laser cavity [52–55]; notably, EOM dual-comb systems [50] reach a mutual coherence time of 1 s, but their spectral bandwidth (e.g., up to 10,000 comb lines) is more than two orders of magnitude narrower than that of mode-locked lasers [22, 44].

Combining the advantages of the coherent frequency comb sources and Fourier transform spectroscopy without moving parts, dual-comb spectroscopy is compatible with dif-

ferent sampling techniques and likely to enable new applications. For example, using an enhancement cavity [18, 51] or a hollow-core fiber [50] for sample interrogations, rapid spectroscopic measurements are achieved with high detection sensitivity. Harnessing the capability of laser beams in long-distance propagation, dual-comb spectroscopy has been performed for open-path environmental gas monitoring [56, 57].

Regarding the spectral regions, most dual-comb results are obtained on the near-infrared overtone transitions with mode-locked frequency comb generators, exploiting the well-established frequency comb technology in this region. Nevertheless, all spectral ranges provide interesting opportunities for spectroscopy [11]; dual-comb spectroscopy has been reported in different regions, including visible [47], mid-infrared [12, 58–66], and terahertz [49, 67–69] ranges.

### 2.2.3 Motivation of the work of this thesis

Although various proofs of principle have exploited dual-comb spectroscopy in different aspects, the fundamental difficulty of dual-comb instrumentation—the demanding requirement of maintaining the mutual coherence between the two combs over the measurement times—had been hindering the development of this technique at the time when this thesis started. The most powerful approach of mutual coherence establishment, which locks two frequency combs to common references, achieves a mutual coherence time of 1 s [22]. But it represents a limitation: phase correction must be implemented to extend the measurement times. Unfortunately, numerical correction techniques are complicated and often lead to computation errors and spectral artifacts [70–72]; moreover, they are not always implementable, for example, emission spectra with scarce lines in coherent-Raman [39, 40, 73] or two-photon excitation spectroscopy [35] are difficult to correct [74]. Therefore, breaking the barrier of mutual coherence time of 1 s is crucial for an increasing number of exciting applications that require high precision, such as spectroscopic measurements of weak lines, broadband Doppler-free spectroscopy [35], and determination of refractive indices [75], etc.

Secondly, dual-comb spectroscopy is versatile and its attractive strength of multi-heterodyne measurements over broad spectral spans can be exploited for different sample interrogating techniques [18, 50, 51] to provide overall spectral consistency and measurement speeds. Attenuated-total-reflectance spectroscopy is a sampling technique widely used in analytical spectroscopy; harnessing sample interaction with evanescent waves, it studies sample volumes below a nanolitre. Exploiting this technique for broadband high-resolution measurements has interesting possibility to analyze multiple gas molecules in

small amounts. However, almost all the attenuated-total-reflectance gas-phase analysis is based on tunable continuous wave laser spectroscopy, limiting its capabilities for broadband measurements. A new approach is enabled by dual-comb spectroscopy, where the well-collimated laser beam of the frequency comb source can be coupled into an evanescent waveguide for sample interrogation. With a multi-heterodyne interferometric measurement, the absorption and dispersion information of sub-nanoliter gas samples can be retrieved simultaneously.

Another interest of dual-comb spectroscopy is to implement the technique in the mid-infrared region, accessing the molecular fundamental ro-vibrational transitions [12, 58–66]. Due to the complex mid-infrared frequency-comb laser systems and the relatively immature photonics tools (e.g. narrow linewidth continuous-wave lasers), establishing the mutual coherence between two mid-infrared combs for broadband molecular spectroscopy is technically more challenging than that in the near-infrared region. Techniques based on numerical phase correction have been successfully extended to the mid-infrared region [64]; however, as explained above, phase correction techniques are complicated and often introduce artifacts. Therefore, although difficult to achieve, a system with experimental coherence control of the two combs, permitting precise broadband measurements without corrective processing, would further ascertain the frequency precision and validate possible systematic artifacts. New prospects to broadband high-resolution molecular spectroscopy may be opened up.



# Chapter 3

## Feed-forward coherent dual-comb spectroscopy

Dual-comb spectroscopy holds much promise for molecular science. However, the realization of its potential has been hampered by the difficulty of preserving the relative stabilities of the two combs over the time of a measurement. In this chapter, an original dual-comb technique based on feed-forward stabilization addresses this difficulty, with the demonstration of a phase-stable dual-comb interferometer in the near-infrared domain.

### 3.1 Background

#### 3.1.1 Phase noise perturbations

A train of short pulses emitting from a laser cavity is very sensitive to intracavity and environment noises. For example, slight instabilities of the cavity length lead to variations of the pulse repetition rate, fluctuations of the power of the pump laser modify the cavity dispersion and result in variations of the carrier-envelope phase, and noises from the environment, such as acoustic noises and mechanical vibrations, perturb both the amplitude and the phase of the pulses. These noise sources and their related influences on the mode-locked laser frequency combs have been thoroughly studied [76, 77]. Due to these perturbations, the width of the comb lines is not infinitely narrow. Generally, for a free-running mode-locked erbium fiber laser, the linewidth is on the order of hundreds of kHz within an integration time of 1 s (e.g., 260 kHz within 1.3 s [48]). Radio-frequency stabilization techniques, relying on piezo and current modulation, remove the low-frequency fluctuations efficiently and render comb lines on the order of 100 kHz in width [48, 77].

The rapid (high-frequency) fluctuations, which are averaged out through long integration times in optical frequency metrology, however, create phase distortions in dual-comb spectroscopy.

The phase distortions in dual-comb interferometers are the same as those with the interferometric phase errors in Michelson-based Fourier transform spectroscopy. In a Michelson interferometer, a slight asymmetry or misalignment of the two arms causes sampling errors in the interferogram and results in chromatic artifacts in the spectrum, e.g., a subtle position asymmetry leads to the distortion of the instrumental line shape [78]. These artifacts degrade the spectral precision and prevent quantitative spectroscopic analysis.

In a dual-comb system, the pulses of a comb initiate the molecular free-induction decay (e.g., on the nanosecond scale for transitions in the gas phase). And the other comb samples the decay at even time delays automatically and periodically. The molecular information is encoded in the dual-comb interferogram with a time scale stretched by a factor  $K=f_r/\Delta f_r$  (e.g.,  $K = 10^6$  when  $f_r = 100$  MHz and  $\Delta f_r = 100$  Hz). Ideally, if the two combs are mutually coherent, the exciting pulse train is sampled accurately by the sampling pulses. The resulting interferometric waveform can be digitized with a constant clock rate at the repetition frequency  $f_r$ , where the time interval between the two consecutive samples  $1/f_r$  corresponds to an increment in optical delays (optical sampling interval) between the two optical pulses of  $\Delta f_r/f_r^2$  (e.g., 10 fs). The molecular information can then be revealed correctly without any instrumental artifacts by a Fourier transform. In the real world, the interferogram is perturbed by the dual-comb fluctuations, which originate from the relative instability of the two degrees of freedom, namely the repetition frequencies and the carrier-envelope offset frequencies, of the two combs. The effect of the phase and timing fluctuations in dual-comb interferometers has been discussed in [48]. The dual-comb optical sampling interval on the femtosecond scale is sensitive to the relative timing variations between the interrogating pulses and the sampling pulses, which result from the relative instability of the pulse repetition rates. These timing variations are stretched by the same factor  $K$  and appear as distortions in the dual-comb interferograms. On the other hand, in a dual-comb spectrometer, a relative carrier-envelope frequency difference  $\Delta f_{ce}$  exist (e.g. originating from the different cavity dispersion of the two combs). If  $\Delta f_{ce}$  is constant, it is not a problem because it induces a stable phase slip  $\Delta\varphi_s = 2\pi\Delta f_{ce}/\Delta f_r$  between the consecutive interferometric samples, which translates the dual-comb spectrum in the Fourier domain by a constant frequency  $\Delta f_{ce}$ . This value can be measured precisely with a frequency counter during the measurements for calibrating the frequency scale of the dual-comb spectrum. However, it is practically challenging to control the relative instabilities in  $\Delta f_{ce}$  due to the perturbation of the high-frequency jitters (e.g., up to hundreds of kHz).

These residual fluctuations of  $\Delta f_{ce}$  induce variations in the phase slip in the interferogram, which generate artifacts spoiling the precision of the dual-comb spectra.

Since relative instabilities lead to problematic interferometric errors and artifacts, a necessity in dual-comb spectroscopy is to keep the two combs mutually coherent during the measurements. In the next section, the requirements for realizing such a mutual coherence are discussed.

### 3.1.2 Mutual coherence requirements

The dual-comb spectrometers potentially enable a self-calibrated frequency scale within the accuracy of an atomic clock and a resolution limited only by the spacing of the comb lines (in a spectrum without interleaving). However, these are achievable only when the mutual coherence time of the two combs is sufficiently long to resolve the individual comb lines. In principle, the position of the comb lines can be determined in a single complete sampling period  $1/\Delta f_r$  (e.g., 10 ms when  $\Delta f_r=100$  Hz), and the two combs should be kept mutually coherent over this period for achieving the comb-line resolution. This is demanding because the mutual coherence of free-running or radio-frequency locked combs on the order of tens of microseconds is far insufficient to enable accurate measurements on the millisecond scale, thus unable to resolve the individual lines. For acquiring a spectrum with well-resolved comb lines, the relative jitters of the two sequential pulses must be controlled within the attosecond scale (the combs are at optical frequencies of hundreds of THz).

Moreover, an extended mutual coherence time is required to improve the resolution of the dual-comb spectra. At best, the resolution in a single non-interleaved dual-comb spectrum is intrinsically limited by the comb lines spacing only. Spectra with high resolution (e.g., less than 1 MHz) is demanded in some exciting applications, e.g., broadband Doppler-free multiplex spectroscopy [35]. Nevertheless, resolving comb lines with smaller spacing implies longer mutual coherence times should be obtained in a single continuous measurement, which turns out very complicated because in most dual-comb demonstrations, the direct mutual coherence time of the two combs is rather limited (e.g., 1 s at best [22]).

Further, molecular spectra with a high signal-to-noise ratio are needed in almost all the applications (e.g., detection of weak molecular lines), so coherent averaging has to be implemented most of the times. In principle, the signal-to-noise ratio of the spectra is proportional to the square root of the measurement time when the experimental data are averaged coherently. Phase instabilities result in sampling errors and distortions in the consecutive dual-comb interferograms, preventing effective averaging. On the other

hand, the optical power falling onto the photo-detector should be restricted to avoid the detector nonlinearities [79, 80]; at constant power onto the detector, the signal-to-noise ratio in the dual-comb spectra is inversely proportional to the number of resolved spectral elements [81]. As a result, acquiring a broadband molecular spectrum with a signal-to-noise ratio over 1,000 usually requires a data recording time over 1,000 seconds, even with the state-of-the-art dual-comb spectrometers [64, 82].

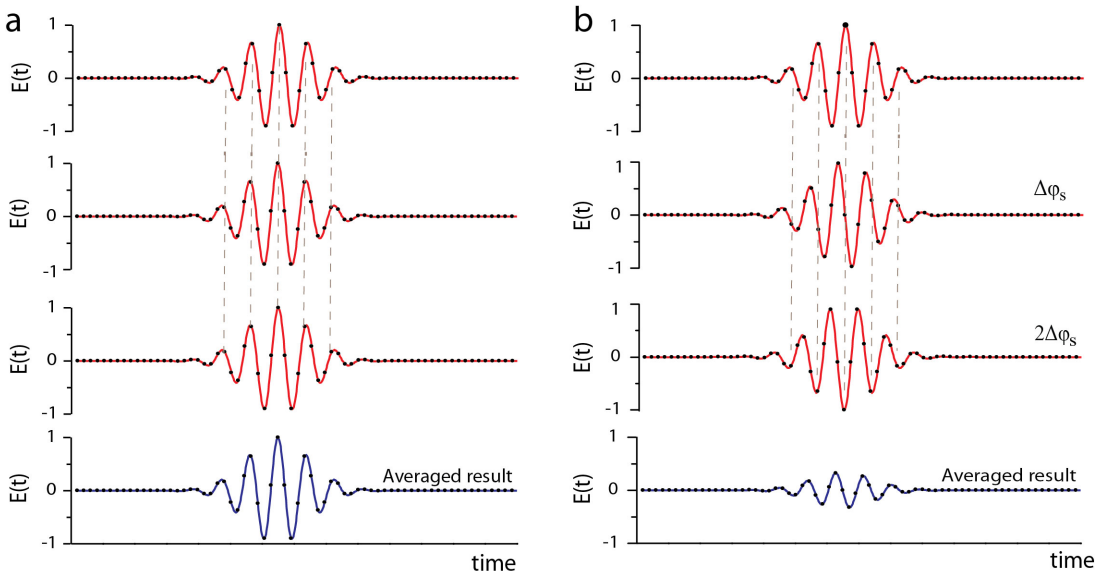


Figure 3.1: **Simulation of averaging dual-comb interferograms.** The blue waveform is the averaged result of the three consecutive interferograms (in red). *a.* Constructive averaging results in an expected waveform without distortion. *b.* A phase shift  $\Delta\varphi_s$  exists in the successive interferograms. The resulting averaged waveform appears with a signal decrease.

Averaging the interferograms in the time domain is more efficient than averaging the spectra in the frequency domain. Dual-comb spectroscopy enables rapid measurements with high data acquisition rates, but sampling at high rates results in the storage and computation of a cumbersome amount of data. Averaging the experimental interferograms in real time (without any post correction) can significantly reduce the file size. In addition to the simplicity of data processing, another benefit of time-domain averaging is the improved signal-to-noise ratio. Part of the essential molecular information, the dispersion, is resolved in the phase spectrum. But the spectral phase is not defined in the region where the signal-to-noise ratio is low, which is usually the case in a non-averaged single-shot measurement. Apart from the requirements of preserving the dual-comb temporal mutual coherence, two additional conditions should be met to enable time-domain averaging.

First, the period of the dual-comb interferograms ( $1/\Delta f_r$ ) should match the sampling grid such that each interferogram is taken with an identical integer number of samples. Second, the interferometric waveform should repeat itself in each period without any phase shift (Figure 3.1). The phase slippage between the consecutive samples,  $\Delta\varphi_s = 2\pi\Delta f_{ce}/\Delta f_r$ , can be canceled by setting  $\Delta f_{ce}$  as an integer multiple of the  $\Delta f_r$ .

In terms of spectral resolution, precision, and signal-to-noise ratio, the quality of the dual-comb spectra strongly depends on the mutual coherence of the two combs. In the next section, a new concept based on feed-forward stabilization for experimentally enforcing coherence is introduced.

## 3.2 Principle of feed-forward dual-comb spectroscopy

### 3.2.1 Mutual coherence establishment

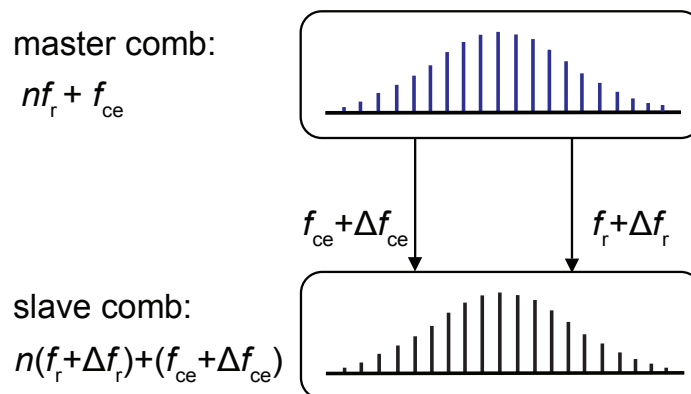


Figure 3.2: **Scheme of mutual coherence establishment.** The slave comb follows the phase fluctuations of the master comb by the stabilization of the relative instability in the repetition frequencies and the carrier-envelope frequencies.

In the feed-forward dual-comb stabilization, the mutual coherence between the two combs is established by directly referencing one comb to the other (Figure 3.2). The first comb serves as a “master comb”, which can be free-running or phase-stabilized. Importantly, the second comb  $f_r + \Delta f_r$ ,  $f_{ce} + \Delta f_{ce}$ , as “slave comb”, follows the fast timing and phase fluctuations of the master comb. As a frequency comb is determined by the two degrees of freedom, this can be achieved by stabilizing the repetition frequency and the carrier-envelope offset frequency of the slave comb relative to those of the master comb.

However, the requirements on the jitter control are technically very demanding, especially the harmful high-frequency jitters (on the order of hundreds of kilohertz) in the carrier-envelope phase will not be removed efficiently with the conventional frequency stabilization technique using piezo and current modulation phase-locked loops, which usually with a phase-lock bandwidth up to a few tens of kilohertz level. A faster actuator should be employed.

### 3.2.2 Feed-forward control

Feed-forward control is a technique known for fast response and low noise. It has been successfully demonstrated for the frequency stabilization of a CW laser [83], for the stabilization of a femtosecond laser to a Fabry-Perot cavity [84], and for the carrier-envelope offset stabilization of a frequency comb [85]. In a feed-forward control, a fast-external actuator, e.g., acousto-optic or electro-optic modulator, is installed at the output of the laser cavity, compensating the fluctuations with high response bandwidth and independence from the intracavity noise sources. This technique is in principle implementable with any kinds of frequency comb generators.

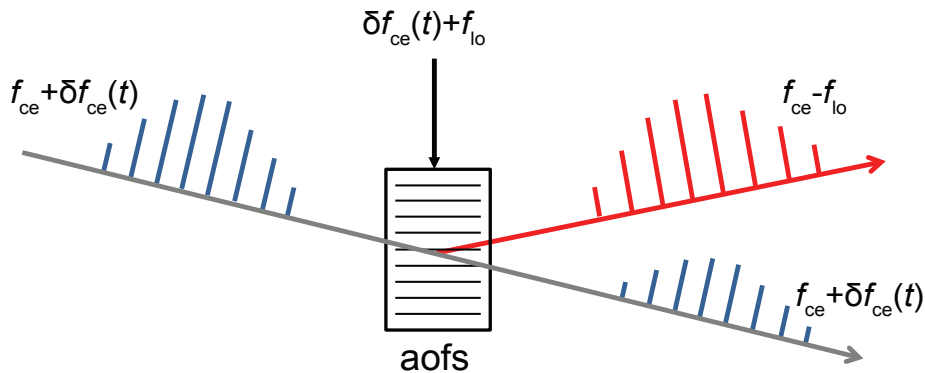


Figure 3.3: Feed-forward control of the carrier-envelope offset frequency of a frequency comb. The AOFS adjusts the carrier-envelope phase of a frequency comb by frequency shifting all the first-order diffracted comb lines by the same amount. This frequency shift can be positive or negative, depending on the direction of the incoming beam towards the acoustic wave. Here a negative diffraction order is used. The instability  $\delta f_{ce}(t)$  in the carrier-envelope offset frequency of the incident frequency comb is stabilized to a constant offset frequency  $f_{LO}$  when the signal  $\delta f_{ce}(t) + f_{LO}$  is fed to drive the AOFS [85].

An acousto-optic frequency shifter (AOFS) is used in the work of this thesis. In the AOFS, a piezoelectric transducer generates an acoustic wave which propagates in the

acousto-optic medium. This sound wave modulates the refractive index of the medium, which is seen by the light wave as an index grating. The incident light, which is diffracted by the grating, is frequency shifted by the amount of the acoustic frequency due to the Doppler effect. When a frequency comb is sent to the AOFS, all the comb lines are shifted by the same amount in frequency. This effect is equivalent to adjusting the carrier-envelope offset frequency of the comb (Figure 3.3). Without any additional locking electronics, the modulation bandwidth is limited only by the response time of the AOFS, e.g., hundreds of nanoseconds [86].

### 3.2.3 Dual-comb stabilization

The scheme of feed-forward dual-comb stabilization is depicted in Figure 3.4.

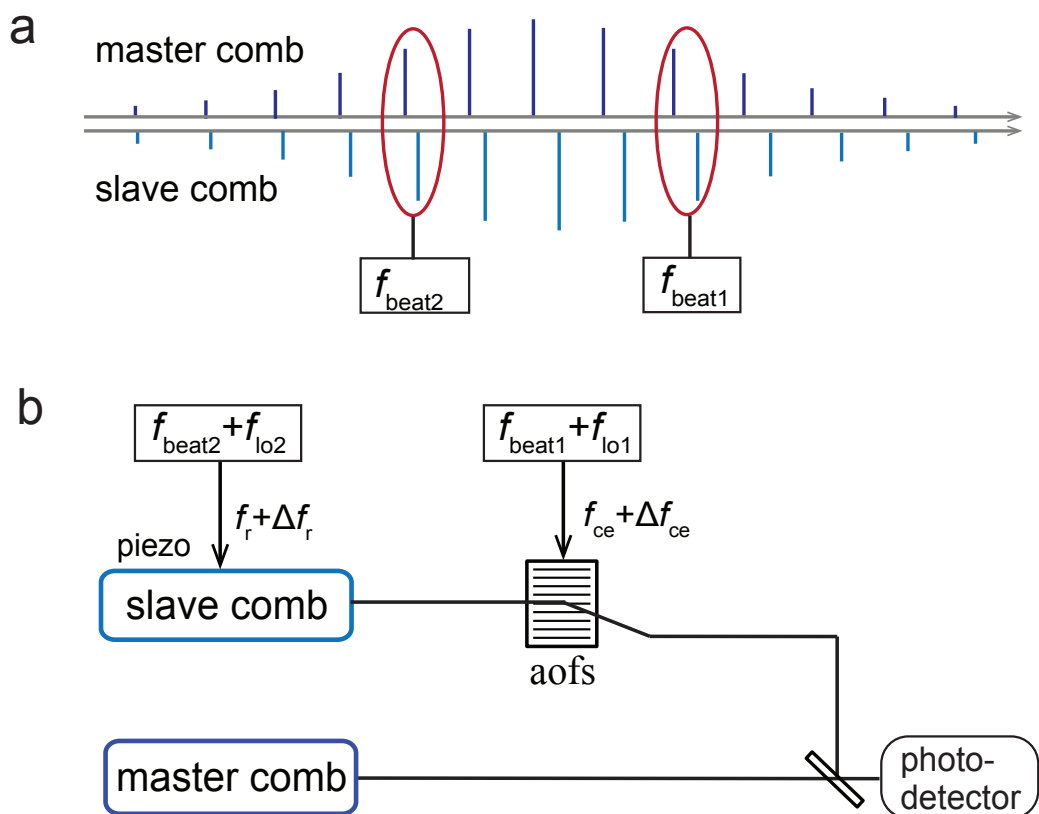


Figure 3.4: **Feed-forward dual-comb stabilization.** *a.* Two radio-frequency beat-notes serve as indicators of the relative instabilities of two degrees of freedom. *b.* Stabilization of the two degrees of freedom: an AOFS controls the relative fluctuation of the carrier-envelope offset frequencies, and a piezo feed-back loop stabilizes the relative repetition frequencies.

**Indication of phase fluctuations.** As in many other demonstrations of dual-comb spectroscopy with mode-locked fiber lasers [22, 46], two radio-frequency beat notes, each between one line of the master comb and one line of the slave comb, are used as gauges of the relative fluctuations of the two degrees of freedom, as shown in Figure 3.4a.

**Stabilization of the relative carrier-envelope frequencies.** The first beat note is mixed with an offset frequency  $f_{LO1}$ , generating a feed-forward driver signal  $f_{beat1} + f_{LO1}$ , feeding the AOFS. The acousto-optic interaction frequency shifts all the comb lines in the first-order diffraction with a quantity containing a constant offset (controlled by  $f_{LO1}$ ) at arbitrary radio frequency and a small amount of acoustic shift (provided by the  $f_{beat1}$ ) that follows the real-time relative fluctuations between the slave and master comb. This is equivalent to a fast adjustment of the carrier-envelope offset of the slave comb relative to that of the master comb.

**Stabilization of the relative repetition frequencies.** For the stabilization of the second degree of freedom, a second beat note  $f_{beat2}$  is generated by beating the  $n_2$ -th line of the master comb and that of the first-order diffracted slave comb. This beat note  $f_{beat2}$  can be stabilized against a radio-frequency reference signal  $f_{LO2}$  using a feed-back loop. Because the AOFS removes the high-frequency noises in the relative carrier-envelope frequencies, the residual instabilities in the repetition frequencies (at low frequencies) can be stabilized with the piezo phase-locked loop of low bandwidth.

### 3.3 Experimental setup

We explore the performance of feed-forward dual-comb interferometers with a setup dedicated to the near-infrared molecular spectroscopy (Figure 3.5).

**Frequency comb sources.** Two commercial erbium-fiber mode-locked laser oscillators, emitting at around 195 THz with a spectral bandwidth of about 20 THz, are used as master comb and slave comb, respectively. Their pulse duration is about 90 fs. Their repetition frequencies are set such that  $f_r=100$  MHz and  $\Delta f_r=100$  Hz, and may be adjusted by translating an intracavity mirror mounted on a piezo transducer. The output of each oscillator is split into three ports. Each port can be fed to an erbium amplifier, providing an average power up to 300 mW. For broadband spectroscopy, the spectrum at the output of one of the amplifiers of each comb is broadened in a piece of highly nonlinear fiber (HNLF), leading to a spectral bandwidth close to an octave (approximately from 140 THz to 280 THz), as exemplified in Appendix Fig.A.1. The spectrum can be filtered to improve

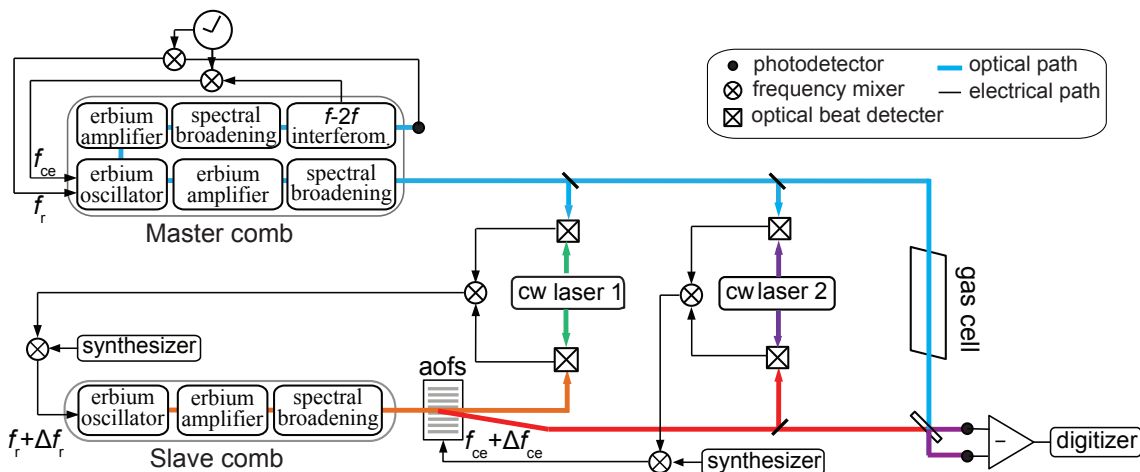


Figure 3.5: **Experimental setup of near-infrared feed-forward dual-comb spectroscopy.**

the signal-to-noise ratio at specific spectral regions with two home-made tunable grating filters.

In this demonstration, the master comb is stabilized against 10-MHz signal of an active hydrogen maser using the self-referencing technique to provide frequency accuracy and long-term stability. This stabilization is independent from the establishment of the mutual coherence, but it is necessary for a serious assessment of the instrumental artifacts and systematic effects. Then, the slave comb is stabilized to the master comb with the feed-forward dual-comb technique. All the synthesizers and the digitizer in the setup are synchronized to the same hydrogen maser.

**Self-referenced master comb.** One amplified output of the master comb is spectrally broadened to an octave for the detection of the carrier-envelope offset frequency in a home-made  $f - 2f$  interferometer. Both the carrier-envelope offset frequency and the repetition frequency of the comb are stabilized to the 10-MHz radio-frequency reference from the hydrogen maser, providing a fractional instability of  $2 \times 10^{-13}$  at 1 s.

**Feed-forward control.** A radio-frequency beat note, of one line of the master comb and one line of the slave comb, is generated to provide the feed-forward driving signal. To isolate an individual line from each comb, an erbium-doped CW laser at 189 THz (labeled as CW laser 1 in Figure 3.5) is used as an intermediate oscillator. The CW laser beats with each comb and two beat notes, of one line of the master comb with the CW laser and of one line of the slave comb with the CW laser, are mixed to cancel the contribution of

the CW laser. The electrical signal at a frequency  $f_{\text{beat1}}$  is thus produced. This signal is then mixed with a radio-frequency signal from a synthesizer, and the resulting signal feeds the AOFS. Here the response time of our AOFS including the related electronics is 550 ns (which leads to a bandwidth of 300 kHz [86]). The carrier-envelope frequency of the beam of the slave comb diffracted in the first order follows that of the master comb with a constant offset. This offset frequency is chosen to be an integer multiple of  $\Delta f_r$  such that the interferometric waveforms are precisely periodic for efficient time-domain averaging.

**Stabilization of the relative repetition frequencies.** For the stabilization of the second degree of freedom, a radio-frequency beat note (as  $f_{\text{beat2}}$ ), between a line of the master comb and a line of the slave is generated, using the CW laser 2 at 195 THz. The beat note is compared to a signal from a synthesizer, and the generating error signal is fed to the piezo transducer, adjusting the cavity length of the slave comb with a bandwidth lower than 1 kHz.

**In-loop measurement.** After the stabilization, the two radio-frequency beat notes, each resulting from a line of the master comb and a line of the first-order slave comb (one at frequency  $f_{\text{beat1}}$ , and the other at frequency  $f_{\text{beat2}}$  in Fig. 3.4), are measured with a radio-frequency spectral analyzer. The 3-dB linewidth of the two beat notes is 1 Hz (Appendix Figure A.2), limited by the resolution of the spectral analyzer. The result indicates the relative stabilities between the two combs.

**Interferometer.** For dual-comb interferometry, the beam of the master comb interrogates the gas sample in a single-pass gas cell. It is then combined on a beam splitter with the beam of the slave comb emitted from the first-order diffraction of the AOFS. The interference between the two beams is detected with a balanced InGaAs photodetector, digitized with a data acquisition board, averaged and Fourier transformed. The frequency scale of the resulting spectra is self-calibrated using the repetition frequency and the carrier-envelope offset frequency of the master comb.

## 3.4 Experimental results

### 3.4.1 Interferogram

The established mutual coherence allows efficiently co-adding all the experimental interferograms directly and continuously. An interferogram of the acetylene absorption in the region of the emission of the laser oscillators is shown in Figure 3.6, which results from 186,000 averages of single interferograms (each with  $10^6$  samples) over a total measure-

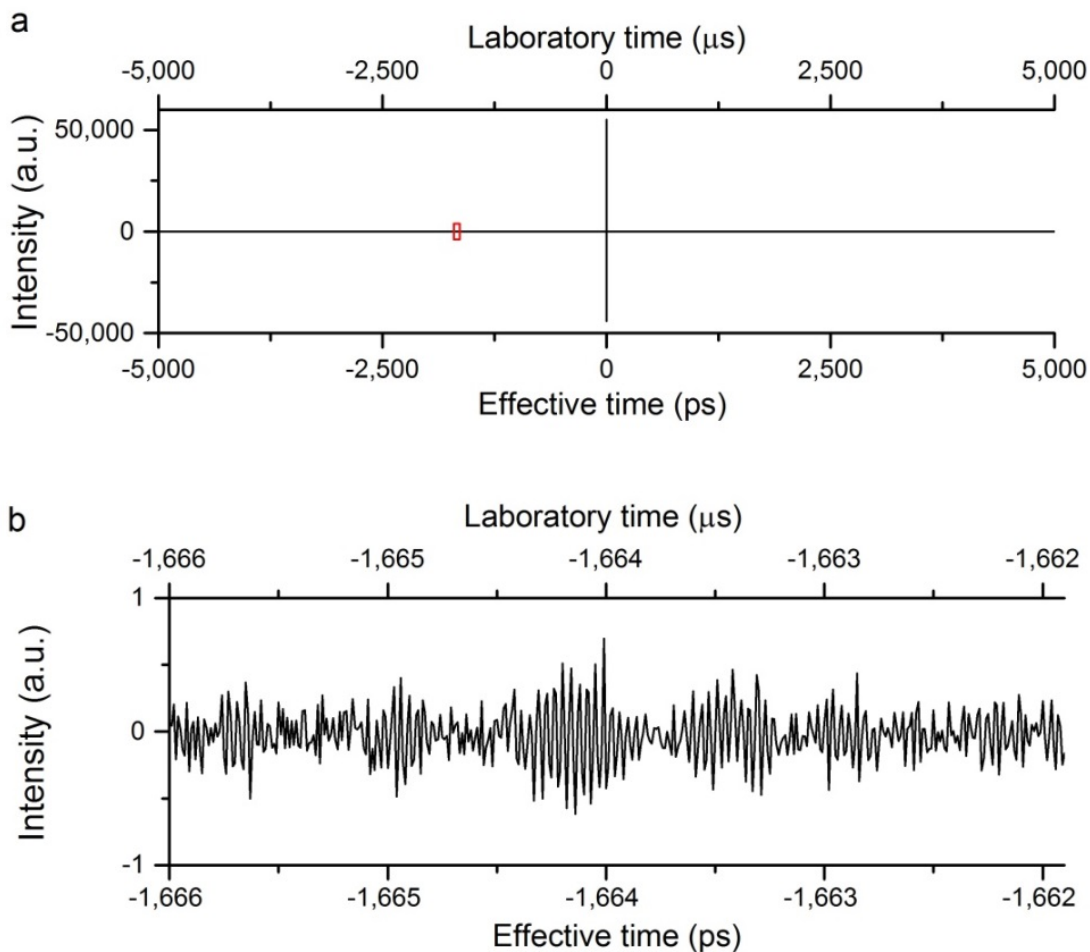


Figure 3.6: **Experimental feed-forward dual-comb interferogram.** In the laboratory timescale, the interferograms repeat with a period of  $1/\Delta f_r = 10$  ms, which corresponds to an optical delay of  $1/f_r = 10$  ns.

**a.** 186,000 consecutive interferograms, each with a laboratory time of 10 ms, are averaged directly, resulting in a total measurement time of 1,860 seconds.

**b.** On a 55,000-fold expanded y-scale, a view of the region indicated by the red rectangle in **a** shows the characteristic interferometric modulation induced by the molecular transitions.

ment time of 31 min. The entire range of optical delay (effective time) is  $1/f_r=10$  ns, corresponding to a 10-ms period of the interference signal in the laboratory frame. The molecular free-induction decay is revealed up to optical delays of 2 ns, which corresponds to the inverse of the Doppler-broadened molecular linewidth. Figure 3.6b exemplifies the characteristic molecular modulations at the optical delay of 1.6 ns.

### 3.4.2 Feed-forward dual-comb spectra

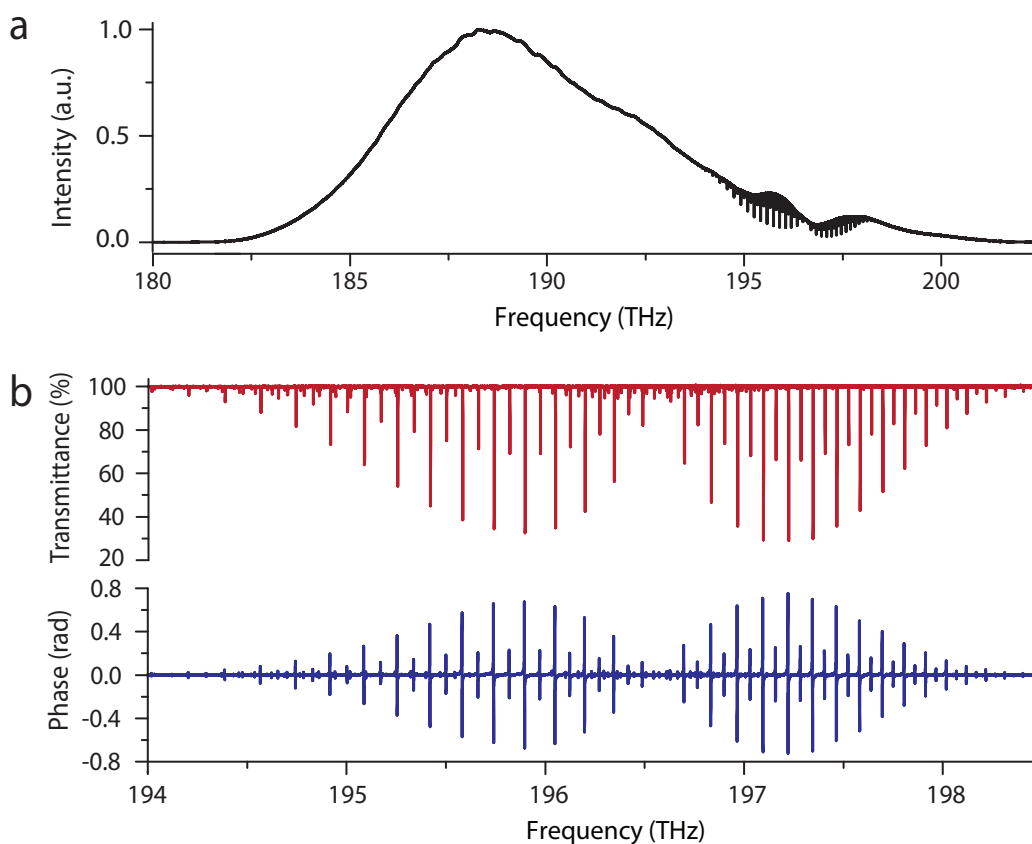


Figure 3.7: **Experimental dual-comb spectrum around 190 THz with a resolution of 100 MHz.** It is recorded with the erbium laser oscillators in the region of the  $\nu_1+\nu_3$  combination band of  $^{12}\text{C}_2\text{H}_2$ . The gas pressure is 195.2 Pa, and the absorption path length is 70 cm. a. The entire spectrum spans 20 THz and its measurement time is 31 min. b. The measured transmittance spectrum and the phase spectrum of the  $\nu_1+\nu_3$  combination band of  $^{12}\text{C}_2\text{H}_2$ . The baselines are corrected with a third-order polynomial fit.

The amplitude and the phase of the spectrum are retrieved by the complex Fourier

transformation of the interferograms. Figure 3.7 depicts a spectrum in the emission region of the erbium oscillators with a resolution corresponding to the comb line spacing, 100 MHz. The spectrum is calculated from the interferogram of Figure 3.6a. The signal-to-noise ratio in the spectrum reaches 8,550 around 188.2 THz and the average signal-to-noise ratio across the entire span, from 182 THz to 202 THz, is 3,850. The good signal-to-noise ratio in both the transmittance and the phase spectra (Figure 3.7b) enables to observe not only the rotational lines of the  $\nu_1 + \nu_3$  and  $\nu_1 + \nu_2 + (\nu_4^1 + \nu_5^{-1})^0$  combination bands, but also the  $\nu_1 + \nu_2 + \nu_4^1 - \nu_4^1$  and the  $\nu_1 + \nu_2 + \nu_5^1 - \nu_5^1$  hot bands of  $^{12}\text{C}_2\text{H}_2$  and even the  $\nu_1 + \nu_3$  band of  $^{12}\text{C}^{13}\text{CH}_2$ , whose concentration (in natural abundance) is 90-fold lower.

The figure of merit of a dual-comb spectrometer is defined as the product of the average signal-to-noise ratio in an unit square root of measurement time and the number of resolved spectral elements [42, 81]. In this demonstration of feed-forward dual-comb spectroscopy in the near-infrared region, the figure of merit reaches  $1.8 \times 10^7 \text{ Hz}^{1/2}$ . It is slightly higher but on the same order of magnitude than that of [22]. In the experiment, the power on the detectors is limited to  $50 \mu\text{W}$ , a value that is experimentally determined to avoid the detector nonlinearities. Similar to Michelson-based Fourier transform spectroscopy, subtle detector nonlinearities create line shifts and line profile distortions [79, 80].

The Fourier transform of interferograms with multiple bursts reveals dual-comb spectra with resolved comb lines. An acetylene absorption spectrum in the region of emission of the laser oscillator is shown in Figure 3.8. The total measurement time is 31 min. Six-thousand interferograms, each with a measurement time of 0.31 s (31 bursts), are averaged and transformed with 6-time zero filling. In Figure 3.8a, more than 200,000 comb lines are resolved over the entire spectral range of 20 THz. Figure 3.8b exemplifies the measured molecular transitions by displaying the  $P(7)$  Doppler-broadened line of the  $\nu_1 + \nu_3$  band of  $^{12}\text{C}_2\text{H}_2$  in the region around 195.581 THz. Its full width at half maximum (FWHM) is near 473 MHz at 295 K. In the unapodized representation in Figure 3.8c, the expected instrumental line shape, cardinal sine function, is well resolved in the comb lines, illustrating the phase stability of this dual-comb system. The FWHM of the comb lines is set about 3.5 Hz in the radio-frequency domain, converting to 3.5 MHz in the optical scale, at the transform limit. Importantly, the width of the instrumental line shape in the comb lines is narrower than the Doppler profiles by two orders of magnitude, thus its contribution to the molecular line shapes is negligible.

The evolution of the average signal-to-noise ratio of the spectrum as a function of the measurement time (and the number of averages) is shown in Figure 3.9. The interferograms are averaged in the time domain and transformed to spectra with a resolution of 100 MHz. The average signal-to-noise ratio of the spectra for different measurement times is

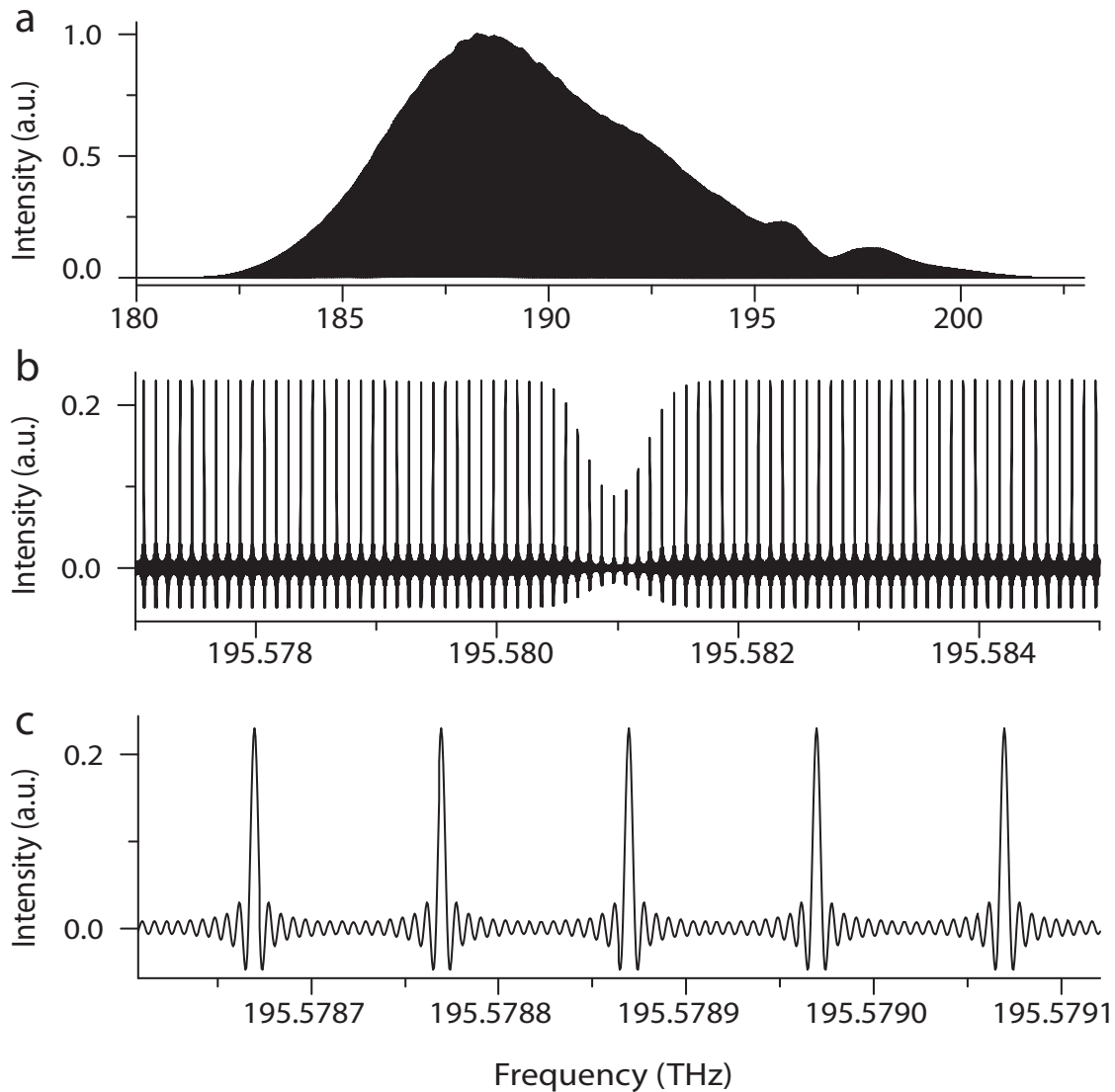


Figure 3.8: **Experimental spectrum around 190 THz with resolved comb lines**, measured within 31 min.

a. Apodized spectrum across the entire span of the emission of the laser oscillators. Over 200,000 individual comb lines spanning 20 THz are resolved.

b. A magnified unapodized representation with the  $P(7)$  Doppler-broadened line of the  $\nu_1+\nu_3$  band of  $^{12}\text{C}_2\text{H}_2$ , which is sampled by the comb lines of 100-MHz spacing.

c. Magnified unapodized representation of **a** with five individual comb lines. The instrumental line shape, a cardinal sine, convolves the unapodized lines.

calculated. A linear fit to the logarithmic representation of the experimental data yielding a slope of 0.498(3) indicates that the signal-to-noise ratio is proportional to the square root of the measurement time. The mutual coherence of the two combs is preserved over the measurement time of 1,860 s, which is three orders of magnitude longer than the best result of 1 s before [22]. No indications that the signal-to-noise ratio departs from this square-root evolution. Therefore, longer averaging times may be achievable.

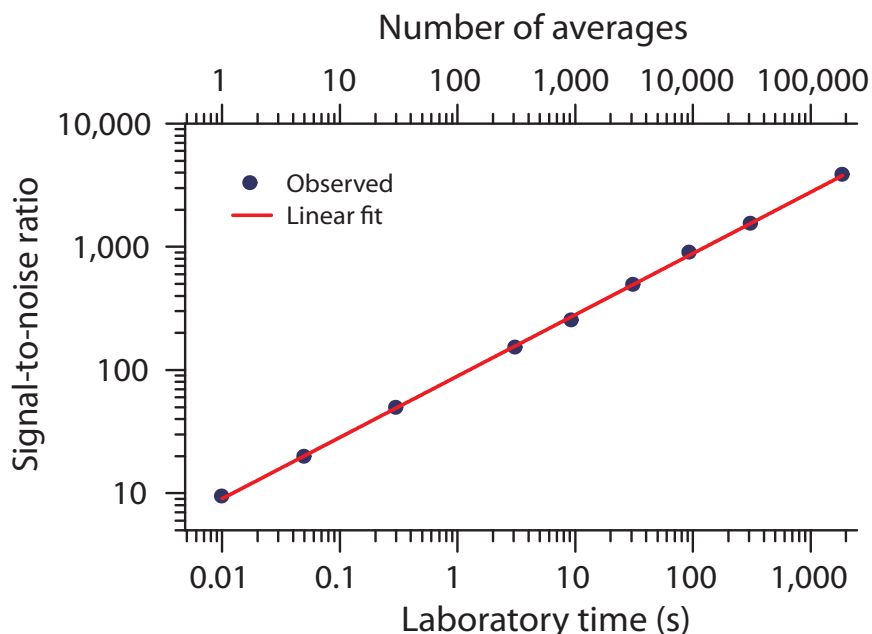


Figure 3.9: Evolution of the average signal-to-noise ratio in the near-infrared feed-forward dual-comb spectra with the measurement time.

A similar behavior is observed over the entire span broadened by the highly nonlinear fibers. A spectrum in the region of the  $2\nu_3$  band of methane around 180 THz with a resolution of 100 MHz is shown in Appendix Figure A.3. It spans from 175 THz to 184 THz and the measurement time is 14.46 s. The signal-to-noise ratio is 770 around 183.2 THz, and the average signal-to-noise ratio is 465, resulting in a figure of merit of  $1.1 \times 10^7 \text{ Hz}^{1/2}$ . The comb lines are resolved over the entire span, as exemplified in Appendix Figure A.4.

### 3.4.3 Assessment of the spectra

The molecular lines in the experimental dual-comb spectra are analyzed and the resulting spectroscopic parameters are compared to the data available in the literature.

The absorption in the experimental spectrum  $I(f)$  is governed by the Beer’s law [1], which describes the intensity of the light  $I_0(f)$  after traveling a path length  $l$  in an absorbing sample,

$$I(f) = I_0(f)e^{-\alpha(f)l}, \quad (3.1)$$

where  $\alpha(f)$  is the absorption coefficient of the sample at the frequency  $f$ . When the baseline spectrum  $I_0(f)$  is obtained, with a reference measurement without a sample or with a low-order polynomial fit on the experimental absorption spectrum, the molecular absorption in the transmittance spectrum  $T(f)$  can be accessed with  $T(f)=I(f)/I_0(f)=e^{-\alpha(f)l}$ . A logarithm operation on the transmittance spectrum reveals the line profiles in the molecular absorption coefficient

$$\alpha(f) = -\ln[T(f)]/l. \quad (3.2)$$

Appropriate profiles, e.g., Gaussian profile when the lines are dominated by Doppler broadening at low gas pressure, can be fitted to the absorption coefficient  $\alpha(f)$ . The line parameters (e.g., position, width, and intensity) are then retrieved.

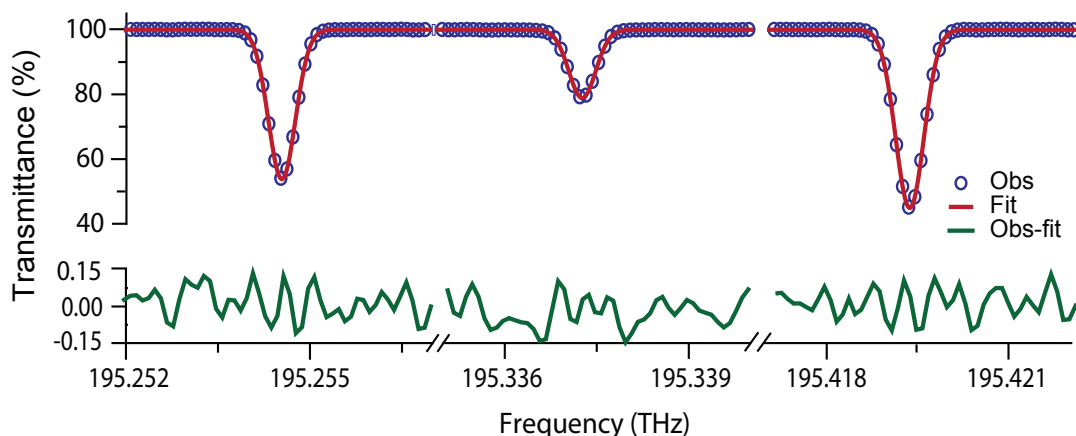


Figure 3.10: **A portion of the acetylene experimental transmittance spectrum and its fitted result.** The measurement time is 31 min. From left to right, the spectrum shows the  $P(17)$ ,  $P(16)$  and  $P(15)$  lines of the  $\nu_1+\nu_3$  band of  $^{12}\text{C}_2\text{H}_2$ . The transmittance goes down to 40%. The Gaussian profiles (red line) are fitted to the experimental spectrum data (blue dots). The standard deviation of the Observed-Fitted (“Obs-Fit”) residuals is 0.06%.

The experimental dual-comb spectra are analyzed and the fitted results are as exemplified in Figure 3.10 and appendix Figure A.3c, respectively, for three molecular lines, the

$P(17)$ ,  $P(16)$  and  $P(15)$ , of the  $\nu_1+\nu_3$  band of  $^{12}\text{C}_2\text{H}_2$  and the  $Q(1)F2$  line of the  $2\nu_3$  band of  $^{12}\text{CH}_4$ . The residuals at the noise level do not show any systematic effect. This fitted result verifies that the instrumental line shape that convolves the profiles can be neglected, thanks to the high mutual coherence of the two combs, the long averaging time, and the narrow width of the comb lines.

The center position of eleven lines of the  $\nu_1+\nu_3$  band of  $^{12}\text{C}_2\text{H}_2$ , for which the pressure shift parameter is measured in [87], is compared to the accurate sub-Doppler saturated absorption measurements from Ref. [88] and Ref. [89] in Appendix Table B.1. The mean value of the discrepancies between our measurement and those in Ref. [88] and Ref. [89] is 110 kHz and 44 kHz, with a standard deviation of 275 kHz and 285 kHz, respectively. Two lines of the  $2\nu_3$  band of  $^{12}\text{CH}_4$  are listed in appendix Table B.2, where the pressure shifts are corrected using the result from [90]. The measurement is in agreement with the Doppler-free line positions of ref. [91].

## 3.5 Conclusion

This chapter has discussed the major limitation of dual-comb instrumentation: the difficulty of preserving the mutual coherence of the two combs over long measurement times. An original dual-comb technique based on feed-forward control of the relative carrier-envelope instabilities is proposed and demonstrated, circumventing this difficulty.

Phase-stabilized dual-comb spectroscopy is achieved with an experimental mutual coherence time approaching 2,000 seconds. This technique does not require any electronic- or digital- corrections of phase errors. Such a result is more than three orders of magnitude better than the previous best result of 1 s [22, 44]. As there is no indication that we reach a limit in times of coherent averaging, arbitrary measurement times may even be within reach. Molecular spectra of high quality with well-resolved comb lines are acquired at high signal-to-noise ratio across a broad span.

With the feed-forward dual-comb stabilization, a compact external-cavity actuator is employed, which is implementable with any types of frequency comb generators where fast control of the phase variations is challenging, including quantum cascade lasers [92], or micro-resonator combs [93]. Besides, the technique is expected to offer new solutions for dual-comb interferometers in other spectral regions of interest where the control of phase fluctuations remains complicated, such as the ultraviolet or the mid-infrared regions.

This phase-stable dual-comb interferometer offers prospects to fundamental or applied problems in atomic and molecular physics. Future applications include multiplex Doppler-

free spectroscopy at high resolution and high precision [35], investigation of optical activity and study of refractive index with high phase precision, etc. In the next chapter, the technique is exploited to study gas molecular sample of small amounts with attenuated-total-reflectance spectroscopy.

# Chapter 4

## Attenuated-total-reflectance dual-comb gas-phase spectroscopy

Attenuated-total-reflectance spectroscopy is one of the most widespread sampling techniques in vibrational spectroscopy of condensed phase [36]. It allows samples in solid or liquid state to be examined directly without further preparation. Such a sampling technique has been widely used in diverse fields of chemical and biomedical studies [94–96]. It exploits light-matter interaction with evanescent waves, which provide a limited penetration depth into the sample. One of the advantages of attenuated-total-reflectance spectroscopy is that the short interaction length can avoid the problematic attenuation of infrared signal in a highly absorbing medium (e.g., water solution) [94, 95]. Besides, the light beam is restricted in a small region within the evanescent field, therefore this technique allows to study samples in small volumes (e.g., on the nanoliter scale [24]). Sample interaction with evanescent waves has enabled detection of chemical chirality [97], high-precision tracking of single biomolecules [96], and fluorescence-based nanoscopy [98], etc.

Despite its success in condensed phase samples, attenuated-total-reflectance spectroscopy is little used in gas-phase spectroscopy [25–27], and it has never been done in broadband gas phase spectroscopy before the work of this thesis. This is due to the fact that combining a broadband spectrometer to an internal reflection element for high-resolution analysis is instrumentally challenging. In this work, leveraging the advantages of feed-forward dual-comb spectroscopy (Chapter 3), we extend attenuated-total-reflectance spectroscopy to coherent multi-heterodyne spectroscopy in the near-infrared domain with a variety of gas absorbers of interrogating volumes as little as tens of picoliters.

## 4.1 Background

### 4.1.1 Evanescent-wave sample interrogation

Evanescent waves establish when the light beam traveling in a medium undergoes a total internal reflection at its boundary. The sample is placed in contact with the internal reflection element, e.g., a prism or a waveguide (Fig. 4.1). At the interface where the internal total reflection happens, the evanescent wave propagates into the sample and interacts with it. The alterations of the evanescent field, e.g., due to the sample absorption, albeit subtle, propagate back into the light beam that can be analyzed spectroscopically. The penetration depth of the evanescent waves into the sample is on the scale of the wavelength (e.g., a micrometer), restricting the light-matter interaction in a small region, e.g., less than a nanoliter in volume. Attenuated-total-reflectance spectroscopy provides nondestructive measurements and it is suited for studying samples of any phase (e.g., gas, liquid or solid, etc). Different from the transmission-based methods, in attenuated-total-reflection spectroscopy, the light beam can be confined in a volume on the nanoliter scale in the evanescent field using, e.g., miniaturized internal reflection elements. It provides opportunities for analyzing samples with little interrogated amounts.

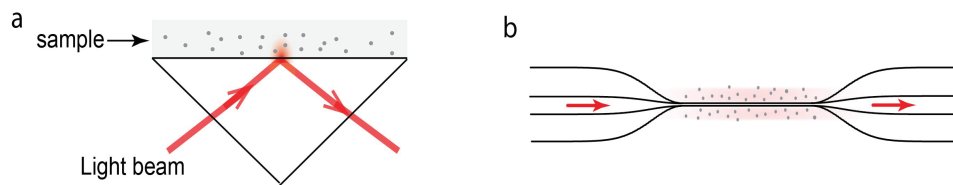


Figure 4.1: **Representative sample interrogation configurations of attenuated-total-reflectance spectroscopy.** a. single-reflection prism. b. tapered-fiber waveguide.

### 4.1.2 Gas-phase attenuated-total-reflectance spectroscopy

Spectroscopic analysis of gas-phase molecules harnessing sample interaction with evanescent waves has been demonstrated with several sampling configurations [25–27], based on tunable CW laser spectroscopy in the near-infrared domain. For instance, for an analysis of methane ( $\text{CH}_4$ ) molecules at around  $1.6\text{-}\mu\text{m}$  region [25], a detectivity of low parts per million in volume (within a measurement time of tens of seconds) has been achieved, leading to as little as  $10^6 - 10^7$  molecules required in a measurement. The detectivity can be enhanced with a chip-based resonator or with sample enrichment [99]. For further improve-

ments, accessing the strong fundamental molecular transitions in the mid-infrared domain presents exciting possibilities [100, 101], but its implementation has been hampered by the difficulty of fabricating mid-infrared waveguides [101]. Before the work of this thesis, all the techniques of gas-phase attenuated-total-reflectance spectroscopy are performed with tunable CW laser spectroscopy. These techniques usually target one specific transition of a particular species [25–27] relying on the prior knowledge of the sample. Therefore their capability of exploring different properties, such as composition and relative concentration, of a samples is rather limited.

However, gas-phase attenuated-total-reflectance spectroscopy over broad spectral spans has not been demonstrated before the work of this thesis, to the best of our knowledge. Most broadband spectrometers employ incoherent light sources (e.g., the tungsten-halogen lamp used in near-infrared Michelson-based spectrometers [36]), which are difficult to collimate and couple into a long internal reflection element for gas measurements with high resolution.

A new approach to broadband attenuated-total-reflectance gas-phase spectroscopy is enabled by dual-comb spectroscopy. The coherent frequency comb laser sources can be coupled into a fiber-based or chip-based waveguide to interrogate the sample with evanescent waves. In this work, the performance of feed-forward dual-comb spectroscopy is extended to attenuated-total-reflectance spectroscopy, analyzing gaseous molecules using a tapered-fiber evanescent element.

## 4.2 Principle

### 4.2.1 Tapered-fiber evanescent waveguide

We use a commercial center-tapered fiber as an internal reflection element (Figure 4.1b), because it provides a path length compatible with gas spectroscopy. The tapered fibers are made by heat stretching a step-index single-mode fiber (SMF-28) to subwavelength diameters under adiabatic conditions. The technique for fabricating such tapered fibers is well established [102], and the waveguide theory of subwavelength tapered fibers has been studied thoroughly in literature [103–105]. Nowadays tapered fibers are used in a wide range of applications, including optical spectroscopy and sensing [96, 106], nonlinear spectral broadening [107], cold-atom physics [108], and waveguide coupling [25], etc.

Two different types of tapered fibers have been utilized in this work. One type of fibers has a taper length of 12 mm and a taper diameter of 1  $\mu\text{m}$ . The other type has a

taper length of 20 mm and a diameter of 500 nm. With the single-mode propagation maintained over the tapered region, the optical transmission efficiency of the beam exceeds 95%. These subwavelength tapered fibers exhibit a significant amount of the light propagating in the evanescent field, which is suited for efficient sample interaction in attenuated-total-reflectance spectroscopy. As an example, the distribution of the mode intensity around a tapered fiber with a diameter of 500 nm in vacuum is depicted in Figure 4.2. More than 90% of the light is guided in the evanescent field at the laser frequency of 200 THz. The intensity fraction of the light guided in the evanescent field  $\eta(f)$ , retrieved from the mode distribution at different laser frequencies, is shown in Appendix Figure A.5 for the two fibers being used. The fraction  $\eta(f)$  increases with the decreasing laser frequencies.

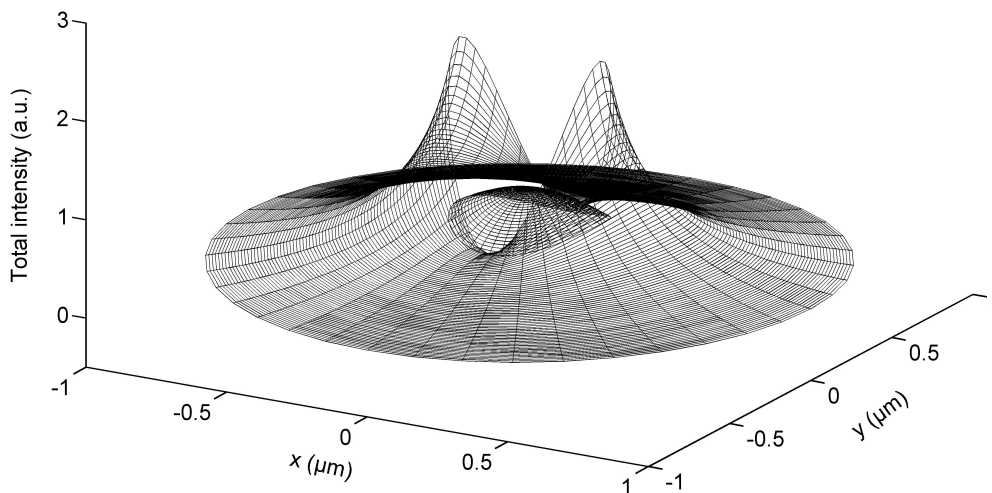


Figure 4.2: **Intensity distribution of the guided fundamental mode at the cross-section of a fused-silica fiber in the vacuum.** The diameter of the fiber is 500 nm, and its reflective index is 1.445. The laser frequency is 200 THz with the polarization aligned along the x-axis. At the fiber surface, the light intensity exhibits a sharp discontinuity, which is due to the high contrast between the index of the fused silica and the vacuum [103, 104]. The penetration depth, determined by the characteristic decay length of the evanescent field [104], is  $1.92 \mu\text{m}$ . About 93.5% of the light intensity propagates in the evanescent field. This numerical simulation is performed using the waveguide theory in Ref [109] and Ref [110], and the results are consistent with those in Ref. [103] and Ref [104].

### 4.2.2 Attenuated-total-reflectance spectroscopy

In the tapered region, the evanescent wave that extends out of the core interacts with the surrounding medium. The molecular sample, which is present within the interaction depth, absorbs the evanescent wave and attenuates the total intensity of the guided mode. In analogy to transmittance-based spectroscopy (section 3.4.3), the absorption in the attenuated-total-reflectance spectra is governed by the Beer-Lambert law [111],

$$I(f) = I_0(f)e^{-\eta(f)\alpha(f)l} \quad (4.1)$$

where  $I_0$  and  $I$ , respectively, correspond to the intensity of light before and after travelling through an absorbing sample.  $l$  denotes the length of the evanescent waveguide in the sample interaction region.  $\alpha(f)$  is the absorption coefficient of the sample, which can be retrieved from the spectrum using

$$\alpha(f) = -\ln[T(f)]/(\eta(f) \cdot l), \quad (4.2)$$

where  $T(f) = I(f)/I_0(f)$ .

To preserve the consistency with transmission spectroscopy (Eq. 3.1), one can refer  $l_e$  as the effective absorption length,

$$l_e(f) = \eta(f) \cdot l. \quad (4.3)$$

The Eq.4.1 can be rewritten as

$$I(f) = I_0(f)e^{-\alpha(f)l_e(f)} \quad (4.4)$$

To discuss the detection limit of this technique, a few quantities are provided as follows. The noise equivalent absorption coefficient  $\alpha_{\min}(f)$  (in unit of  $\text{cm}^{-1}$ ) is one of the common-used standards of detection limit. Derived from the first-order Taylor series of the Beer-Lambert law (Eq.4.4) with the assumption that the absorption is weak,  $\alpha_{\min}(f)$  is inversely proportional to the signal-to-noise ratio ( $SNR$ ) in the spectrum and the effective absorption path length  $l_e(f)$ ,

$$\alpha_{\min}(f) \approx 1/(SNR \cdot l_e(f)) \quad (4.5)$$

Taking the molecular absorption cross-section  $\sigma(f)$  (in unit of  $\text{cm}^2/\text{molecule}$ ) into account using  $\alpha(f) = \sigma(f) \cdot N$ , where  $N$  is the molecular number density (in unit of

molecule/cm<sup>3</sup>), one obtains the minimum detectable value of  $N$  as,

$$N_{\min} \approx 1/(SNR \cdot l_e(f) \cdot \sigma_{\max}), \quad (4.6)$$

where  $\sigma_{\max}$  is the maximum absorption cross-section of the molecule within the spectral coverage. In a sample interaction volume  $V(f)$  (in unit of cm<sup>3</sup>), the minimum detectable number of molecules is

$$n_{\min} \approx V(f)/(SNR \cdot l_e(f) \cdot \sigma_{\max}). \quad (4.7)$$

The volume  $V(f)$  can be calculated from the area indicated by the penetration depth (Appendix Figure A.6) and the length of the tapered waist. For the two tapered fibers being used in the experiment,  $V(f)$  ranges from about 10 picoliters to 14 nanoliters.

### 4.3 Experimental setup

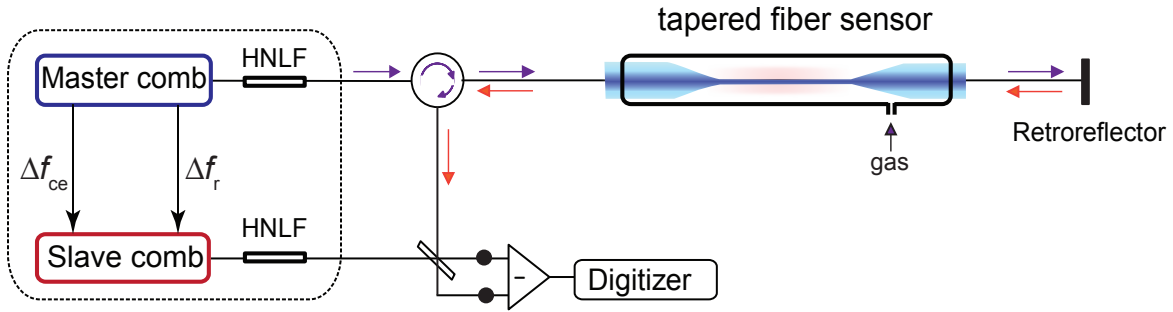


Figure 4.3: **Experimental setup of dual-comb attenuated-total-reflectance gas-phase spectroscopy.** The black-dot rectangle indicates the setup of feed-forward dual-comb stabilization. HNLF: highly-nonlinear fiber. The size of the sensor is not scaled to its actual proportions.

The performance of broadband dual-comb attenuated-total-reflectance gas analysis is explored with a setup in the near-infrared domain, as depicted in Figure 4.3, consisting of our feed-forward dual-comb spectrometer (see Chapter 3 for details) and a sample interrogation unit with a tapered fiber.

The beam of master comb passes through a circulator and it is sent to the tapered-fiber evanescent waveguide in a vacuum cell that can be filled with gases. For improving the absorption path length, the tapered fiber is double-passed using a fiber-optic retroreflector connected at the end of the tapered-fiber, which reflects the beam back to the sample

interaction region. After interrogating the sample, the beam of the master comb circulates by the circulator and overlaps with the beam of the slave comb using a 50:50 fiber coupler. A balanced detector receives the two outputs of the coupler, and a digitizer records the time-domain interferometric signal. The interferograms are Fourier transformed to derive the amplitude and phase of the attenuated-total-reflectance spectra. The experimental data are averaged to improve the signal-to-noise ratio.

## 4.4 Experimental results

### 4.4.1 Dual-comb attenuated-total-reflectance spectra

An experimental dual-comb attenuated-total-reflectance spectrum in the region of the  $2\nu_3$  band of methane around 180 THz is shown in Fig 4.4. The effective absorption path length is about 5.2 mm, the penetration depth is about  $0.5 \mu\text{m}$  and the sample interaction volume is fewer than 25 picoliters. At the gas pressure of  $68.5 \times 10^3 \text{ Pa}$ , the full width at half maximum (FWHM) of the molecular lines is broadened to more than 2.4 GHz [112]. To sample the molecular profiles correctly while preserving the signal-to-noise ratio, the spectral resolution is set at 1 GHz. Due to the mismatch between the resolution desired in the spectra and the comb line spacing (100 MHz in this dual-comb system), only 10% of the measurement time is acquiring useful data and the rest of the time is wasted. In a total experimental recording time of 310 s (60,000 averages), where only 31 seconds of the data contribute to computing the molecular spectrum, the signal-to-noise ratio in the spectrum at around 180.5 THz exceeds 12,660. The average signal-to-noise ratio across the span of 13 THz is 5,920, resulting in a figure of merit (as defined in Section 3.4.2, Chapter 3) of  $4.4 \times 10^6 \text{ Hz}^{1/2}$ , calculated using the total experimental time of 310 s. Both the transmittance and dispersion spectra exhibit a good signal-to-noise ratio, which is suited for the detection of weak absorptions. The entire  $2\nu_3$  band of  $^{12}\text{CH}_4$  is resolved, although its maximum absorption depth and phase shift are less than 8% (Fig. 4.4b) and 40 mrad (Fig. 4.4c), respectively.

The absorption coefficient of the  $2\nu_3$  band of  $^{12}\text{CH}_4$  is obtained from the experimental spectrum (Fig. 4.4b) using Eq. 4.2, where the result of the frequency-dependent intensity fraction  $\eta(f)$  in Fig. A.5a has been taken into account. As shown in Fig 4.5, the experimen-

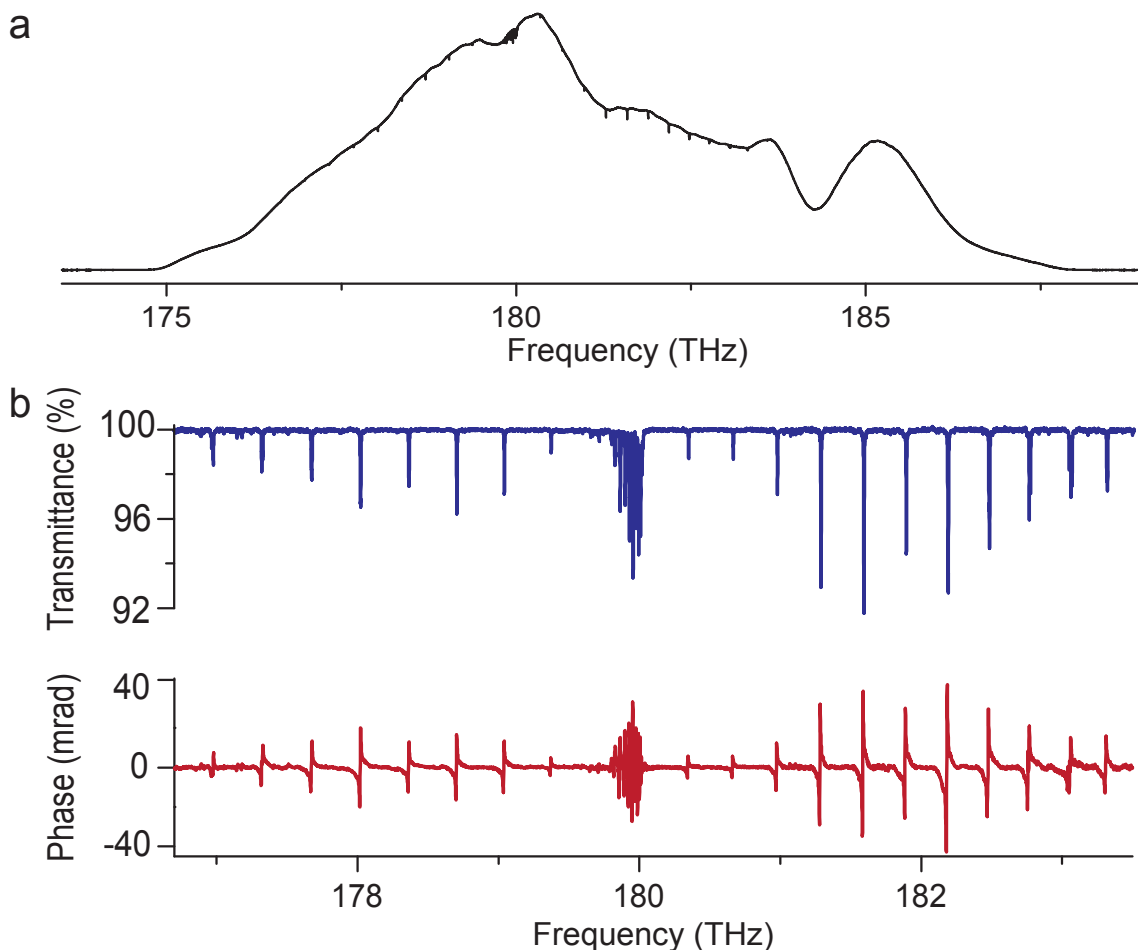


Figure 4.4: **Experimental dual-comb attenuated-total-reflectance spectrum in the region of the  $2\nu_3$  band of  $^{12}\text{CH}_4$ .** Its resolution is 1 GHz.

a. A filtered spectrum around 180 THz. The tapered fiber with a waist diameter of  $1\ \mu\text{m}$  and a length of 12 mm provides an effective absorption path length of about 5.2 mm.

b. The transmittance and phase spectra of the  $2\nu_3$  absorption band of  $^{12}\text{CH}_4$ . The base lines are fitted with low-order polynomial functions.

tal absorption coefficient is compared to the methane absorption coefficient calculated with Voigt line profiles using the line parameters available in HITRAN database [113]. The HITRAN line list includes the 2014 GOSAT methane line intensities [114], the line positions from Ref. [52], and the line broadening coefficients from Ref. [112]. The “Obs-HITRAN” residuals are within  $0.2\ \text{cm}^{-1}$ , which is about 5% of the maximum absorption coefficient ( $0.4\ \text{cm}^{-1}$  at the  $R(4)$  manifold) in the region of the measurement. The standard deviation of the residuals is  $1.6 \times 10^{-3}\ \text{cm}^{-1}$ , corresponding to 0.4% of the maximum absorption coefficient. Such results assert the agreement between this work and the literature data.

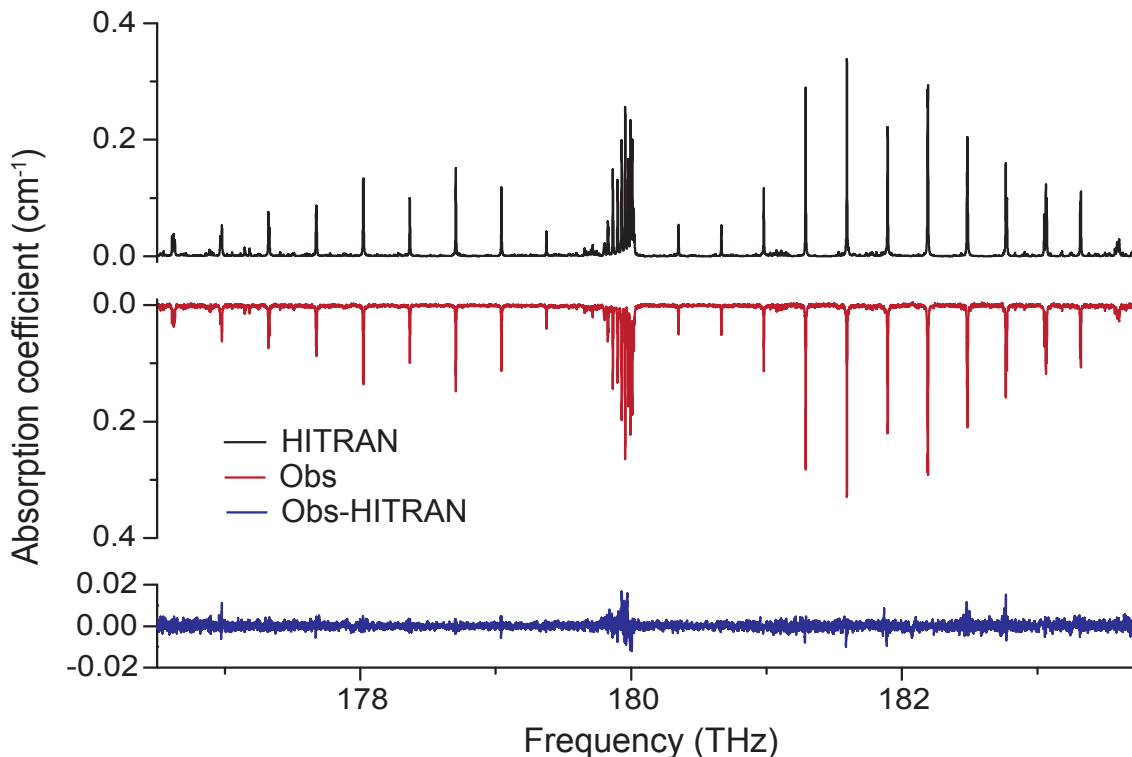


Figure 4.5: **Characterization of the dual-comb attenuated-total-reflectance spectrum.** The observed absorption coefficient of the  $2\nu_3$  absorption band of  $^{12}\text{CH}_4$  with a resolution of 1 GHz, is compared to a spectrum calculated using the line parameters in HITRAN 2016. The Obs-HITRAN residuals are within  $0.02\text{ cm}^{-1}$ , with a standard deviation of  $1.6 \times 10^{-3}\text{ cm}^{-1}$ .

Good signal-to-noise ratio is obtained over the entire spectral coverage of the dual-comb system (covering from about 140 THz to 280 THz, as shown in Fig. A.1). A spectrum in the region of the  $\nu_2+2\nu_3$  band of  $^{12}\text{CH}_4$  around 225 THz is depicted in Appendix Fig. A.7, where the FWHM of the molecular lines is collisionally broadened to larger than 6 GHz and the resolution of the spectrum is set to 2 GHz. In a measurement time of 480 s (only 5% of the time is used for calculating the spectrum), the signal-to-noise ratio culminates at 21,800 around 226 THz and the average signal-to-noise ratio of 12,800 results in a figure of merit of  $3.4 \times 10^6\text{ Hz}^{1/2}$ . The comb lines in the attenuated-total-reflectance spectra are resolved over the entire spectral coverage, as exemplified in Fig. 4.6 with a spectrum in the region of the erbium oscillators. More than 210,000 comb lines are resolved across 21 THz. The frequency scale of the spectrum can be referenced to an atomic clock (as demonstrated in Chapter 3). Therefore, broadband attenuated-total-reflectance spectra can be achieved with high signal-to-noise ratio, high resolution, and a self-calibrated frequency scale.

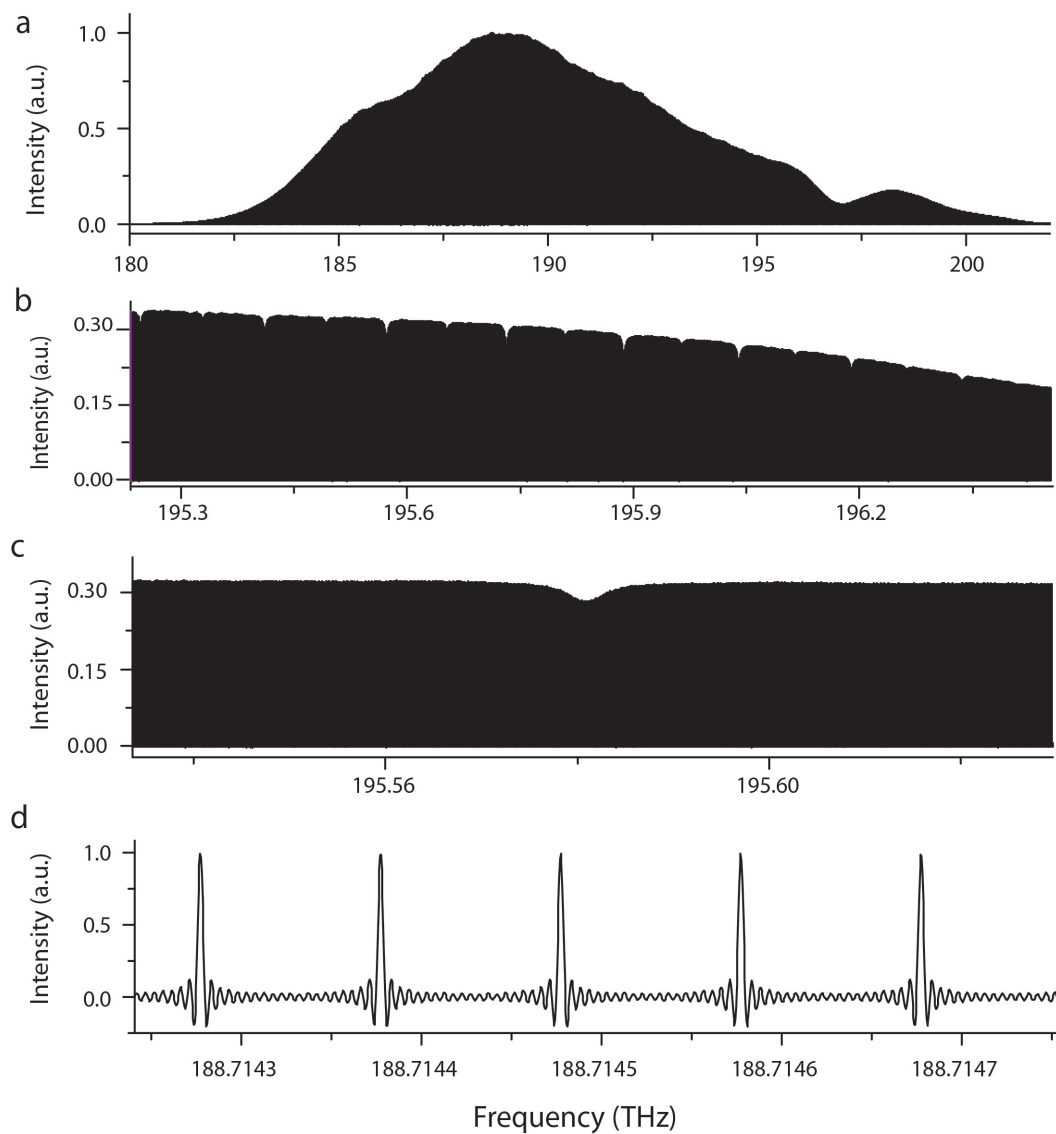


Figure 4.6: **Dual-comb attenuated-total-reflectance spectrum with resolved comb lines.** Its measurement time is 200 s (1,000 averages of 0.2-s recordings). a. Apodized spectrum with the entire span of the erbium oscillators. b. Magnified representation of a at around 195.9 THz showing the  $P$ -branch of the  $\nu_1 + \nu_3$  band of  $^{12}\text{C}_2\text{H}_2$ . The gas pressure is  $5.27 \times 10^4$  Pa, and the equivalent absorption path length is about 4.5 mm. c. Magnified representation with the collisionally broadened  $P(19)$  line of the  $\nu_1 + \nu_3$  band of  $^{12}\text{C}_2\text{H}_2$  resolved by the comb lines. d. A magnified unapodized spectrum of five individual comb lines with line spacing of 100 MHz. The expected instrumental line shape, cardinal sine function, convolves the comb lines. The FWHM of the comb lines is 5 Hz in the radio-frequency domain, at the transform limit.

### 4.4.2 Analysis of molecules in small volumes

The capability of analyzing molecular samples of small amounts is experimentally investigated. In Figure 4.7, a dual-comb attenuated-total-reflectance spectrum in the region of the  $\nu_1 + \nu_3$  band of acetylene is acquired with a gas pressure of 51 Pa. The molecular lines are Doppler-broadened with a FWHM of more than 470 MHz, and the spectral resolution is set to 300 MHz. The double-passed tapered fiber (500 nm in diameter and 20 mm in waist length) provides an effective absorption path length of about 37.4 mm, and the penetration depth of 1.9  $\mu\text{m}$  leads to an interrogation sample volume of less than 0.3 nanoliters. With a total experimental time of 126 s (only 30 % of the total experimental time contributes to acquiring data for calculating the spectrum), its signal-to-noise ratio reaches 6,250 around 197.7 THz, and an average signal-to-noise ratio of 3,750 corresponds to a figure of merit of  $6.8 \times 10^6 \text{ Hz}^{1/2}$ . Due to the low gas density, the maximum absorption and phase shift are only about 1.7% and 10 mrad (Figure 4.7b), and the entire band is resolved.

The signal-to-noise ratio of 6,250 in the spectrum and the effective absorption path length of 37.4 mm result in a noise equivalent absorption coefficient (Eq. 4.5) of  $4.3 \times 10^{-5} \text{ cm}^{-1}$  (or  $4.8 \times 10^{-4} \text{ cm}^{-1} \cdot \text{Hz}^{-1/2}$ ). For acetylene, the absorption cross-section of  $7.92 \times 10^{-19} \text{ cm}^2/\text{molecule}$  (for the Doppler-broadened  $R(9)$  line of the  $\nu_1 + \nu_3$  band) at 197.22 THz leads to a minimum detectable number density (Eq. 4.6) of  $5.4 \times 10^{13} \text{ molecules/cm}^3$ . In the 0.3-nanoliter interaction volume, the detectable number of molecules is about  $1.6 \times 10^7$  (Eq. 4.7), corresponding to 27 attomoles. Unlike other techniques where the detection limit may result from the background spectral fringes due to the beating of multiple waveguide modes [25, 101], in our demonstration, the number of molecules detectable can be further decreased with longer acquisition times, because of the long mutual coherence of the dual-comb spectrometer (Chapter 3) and the single-mode property of the tapered-fiber evanescent element.

This technique can be exploited for analyzing small volumes of gases. For example, local detection of methane leakage from the natural gas systems has attracted significant attention in recent years [115], and attenuated-total-reflectance gas spectroscopy has been proposing solutions [25, 26]. At atmospheric pressure, the methane lines are collisionally broadened, resulting in a linewidth of 5 GHz and an absorption cross-section of  $1.5 \times 10^{-20} \text{ cm}^2/\text{molecule}$  at the  $R(4)$  manifold of the  $2\nu_3$  band [114]. In the experimental spectral region of the  $2\nu_3$  band of methane with a resolution of 1 GHz (Fig. 4.4), our signal-to-noise ratio of  $720 \text{ Hz}^{1/2}$  applying to the detection of  $R(4)$  manifold, leads to a detectable number density of  $2.5 \times 10^{16} \text{ molecules}/(\text{cm}^3 \cdot \text{Hz}^{1/2})$ , which is slightly lower than (with a difference less than a factor of 1.5) the state-of-the-art techniques with photonic crystal slot

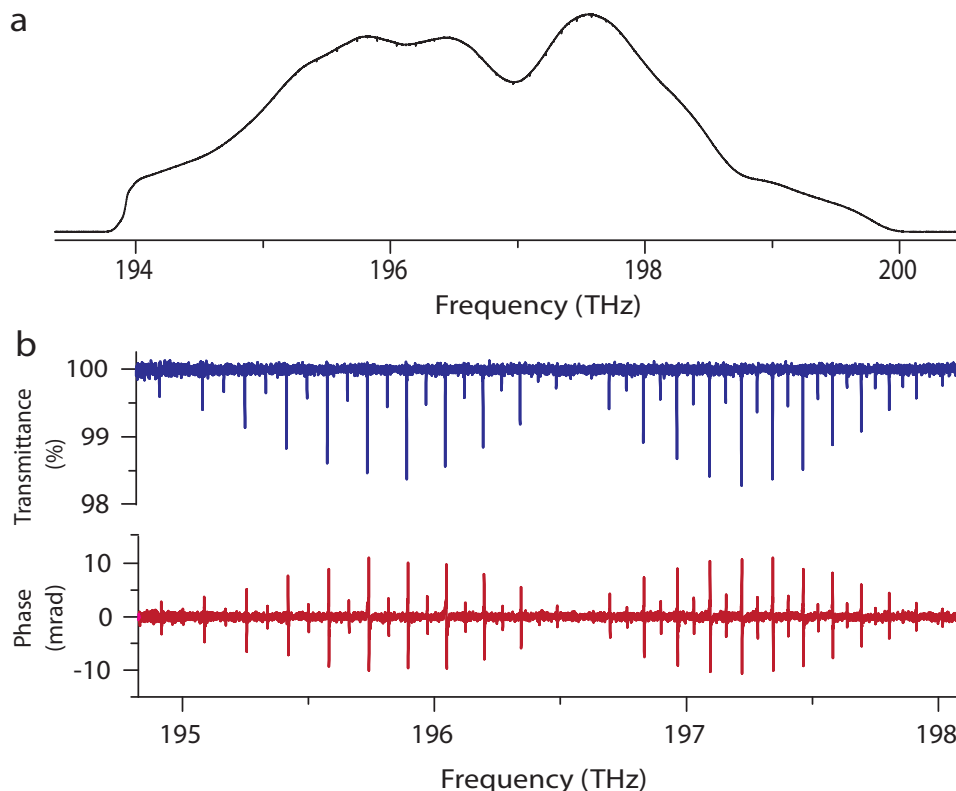


Figure 4.7: **Dual-comb attenuated-total-reflectance spectrum in the region of  $\nu_1 + \nu_3$  absorption band of  $^{12}\text{C}_2\text{H}_2$ .** The gas pressure is 51 pa. a. The experimental spectrum around 197 THz. Its resolution is 300 MHz, and the total experimental time is 126 s. b. The transmittance and phase spectra. The maximum absorption and phase shift are only 1.7% and 10 mrad, respectively.

waveguides [26] and silicon-chip based spiral waveguides [25] based on tunable CW laser spectroscopy, despite our spectra are acquired over a broad bandwidth with the ability to diagnose multiple absorbers simultaneously.

## 4.5 Conclusion

In this chapter, we extend attenuated-total-reflectance spectroscopy to coherent multi-heterodyne analysis of gas-phase molecules with high-resolution (at the Doppler-limited resolution) for the first time. Using a tapered-fiber internal reflection element, broadband dual-comb spectra interrogating sample volumes as little as tens of picoliters, are capable

of analyzing molecules with an amount of tens of attomole ( $10^7$  molecules). Multiple gas species can be analyzed simultaneously over broad spans with the measurement consistency preserved. Our detection limit is close to the state-of-the-art gas-phase evanescent detection techniques based on tunable CW laser spectroscopy [25, 26].

In this demonstration, a considerable amount of the measurement time is wasted because of the mismatch of the molecular linewidth (e.g., up to several GHz) and the 100-MHz line spacing of the dual-comb spectrometer. For future applications, depending on the samples to be analyzed, the measurement time can be improved by choosing a dual-comb spectrometer with a line spacing slightly lower but close to the width of the molecular profiles, e.g., a dual-comb system with comb line spacing of a few GHz is ideal for analyzing acetylene at atmospheric pressure [55].

In the future, if the technology of waveguide fabrication is advanced, dual-comb attenuated-total-reflectance spectroscopy may be implemented with chip-based waveguides. The effective absorption path length may be improved by using a longer waveguide. The detectable number of molecules may be reduced if the technique can be operated in the mid-infrared domain [101] to access the strong fundamental molecular transitions. The feed-forward dual-comb technique is performed in the mid-infrared region in the next chapter.



# Chapter 5

## Mid-infrared feed-forward dual-comb spectroscopy

The mid-infrared spectral region is of fundamental importance for molecular spectroscopy because almost all molecules have strong absorption in this region [1, 36]. As one of the techniques of frequency-comb spectroscopy, dual-comb spectroscopy has been mostly reported in the near-infrared range, where broadband molecular spectra with well-resolved comb lines have been obtained [22, 23]. However, its implementation in the mid-infrared region turns out to be involved. In this chapter, the feed-forward dual-comb technique is extended to the  $3\text{-}\mu\text{m}$  region, providing a solution to mid-infrared dual-comb spectroscopy.

### 5.1 Background

A small molecule, e.g., with as few as three atoms, has multiple fundamental vibrational modes (stretching and bending, etc.) and possesses a large number of rotational and vibrational states. The transitions between these states are characteristic with their unique frequency, usually within the mid-infrared range of the electromagnetic spectrum (15-150 THz or 2-20  $\mu\text{m}$ ). The absorption cross section of these fundamental transitions is typically strong, which will enhance the detection sensitivity. Directly and simultaneously interrogating these molecular fingerprints with high-resolution spectroscopy over broad spans, yields rich information, not only for revealing the structure and dynamics of the molecules [19, 32], but also for unambiguously identifying and quantifying the species in complex mixtures [116]. For instance, in the spectral window around 3  $\mu\text{m}$  [117], which corresponds to the energy of the CH, OH, and NH stretching modes in molecules, broadband molecular spectroscopy has become an irreplaceable tool for the study of many small and large

organic, as well as oxygen- or nitrogen-containing molecules.

Currently, Michelson-based Fourier transform spectroscopy, harnessing a mechanical scanning arm and incoherent light sources, is the workhorse of mid-infrared molecular spectroscopy; it provides broadband spectra with high resolution (e.g., up to 27 MHz [21]). However, as explained in Chapter 2, the limitations of Michelson interferometers are related to the moving parts. Dual-comb spectroscopy is a technique of Fourier transform interferometry without moving parts. Its powerful performance has been mostly explored in the near-infrared region on overtone molecular transitions. Extending its potential to the molecular fingerprint region will enable new possibilities to the discoveries of molecular science; however, its implementation still encounters several challenges.

### 5.1.1 Challenges of mid-infrared dual-comb spectroscopy

Unlike the near-infrared and the visible spectral regions, where frequency comb technology is well established, mid-infrared comb generators are still in active development. Various approaches have been explored, e.g., with novel solid-state [58] or doped-fiber [118] laser gain media, quantum-cascade [92] or interband-cascade lasers [119], micro-resonators [66, 120], and nonlinear frequency conversion such as difference frequency generation [121], optical parametric oscillation [122], and spectral broadening in highly nonlinear waveguides [123], etc.

Apart from the difficulty of generating mid-infrared combs, maintaining the mutual coherence between two mid-infrared frequency combs represent another challenge of mid-infrared dual-comb spectroscopy. So far, most techniques of mid-infrared dual-comb spectroscopy are based on frequency conversion of near-infrared combs. Due to the complexity of the laser systems and the difficulty of designing mid-infrared single-frequency lasers with hertz linewidth for referencing the two combs, the near-infrared dual-comb techniques, based on phase stabilization using common references [22, 44] or phase reconstruction using computer algorithms [46, 48, 68], are difficult to implement in the mid-infrared region.

Last but not least, the photonic tools and optics in the mid-infrared region are not as advanced as those in the visible or the telecommunication region, which represents an additional difficulty.

### 5.1.2 Current state of mid-infrared dual-comb spectroscopy

Because of the difficulties, many results of mid-infrared dual-comb spectroscopy remained a stage of promising proofs of principle, although they point to an intriguing potential

[12, 59, 61–63, 66, 119]. For example, the first results based on frequency comb generators of large comb line spacing, such as semiconductor lasers [61, 119] and micro-resonator combs [66] highlight new opportunities in time-resolved spectroscopy for physical chemistry. Mid-infrared dual-comb spectra with well-resolved comb lines have been produced, although over narrow spectral spans, with systems of quantum cascade [124] and inter-band cascade lasers [119], difference frequency generators using erbium-doped mode-locked fiber lasers [62] and electro-optic modulators [63]. Recently, advanced control of degenerate optical parametric oscillators [65], and difference-frequency comb generators stabilized in the near-infrared in combination with real-time digital corrections [64], have proved in producing broadband mid-infrared spectra with well-resolved comb lines.

In Chapter 3, our recent technique based on feed-forward stabilization of the relative carrier-envelope offset frequencies has been devised with erbium fiber laser combs in the near-infrared region [23]. It allows continuous averaging of interferograms during times approaching 2,000 seconds without any phase correction, which is three orders of magnitude longer than the previous state-of-the-art [22]. Such a technique results in experimental simplicity and reduction of possible spectral artifacts. In this chapter, this technique is extended to the mid-infrared region, accessing one of the most important spectroscopic windows, the 3- $\mu\text{m}$  range.

## 5.2 Principle

Our 3- $\mu\text{m}$  feed-forward dual-comb scheme is based on difference frequency conversion of a phase-stabilized near-infrared system to the mid-infrared region, as sketched in Figure 5.1. The near-infrared dual-comb system has been described in section 3.2, where the master comb is self-referenced to a radio-frequency atomic clock to provide the long-term stability, while the slave comb follows the fast phase variations of the master comb with a relative stabilization using feed-forward control. The two erbium combs are frequency converted to the mid-infrared region using a single-frequency laser as the pump in the difference-frequency generation process.

The principle of difference frequency generation between a frequency comb and a single-frequency laser is illustrated in Fig. 5.2. Such a frequency conversion technique has been exploited in dual-comb spectroscopy with erbium combs [62] and with electro-optic modulators [63]. Mixing a continuous-wave laser with a pulsed laser is a process of low efficiency. The signal pulsed laser emits a large amount of photons in a short duration; within this period the photons of the continuous-wave laser are entirely depleted in the conversion

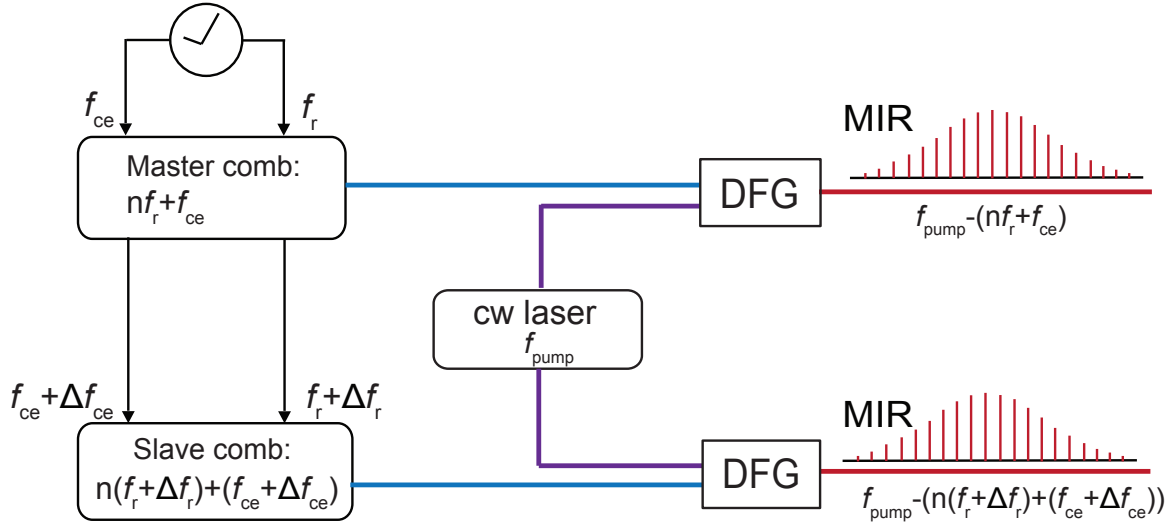


Figure 5.1: **Scheme of mid-infrared feed-forward dual-comb spectroscopy.** DFG: difference frequency generation; CW: continuous-wave; MIR: mid-infrared.

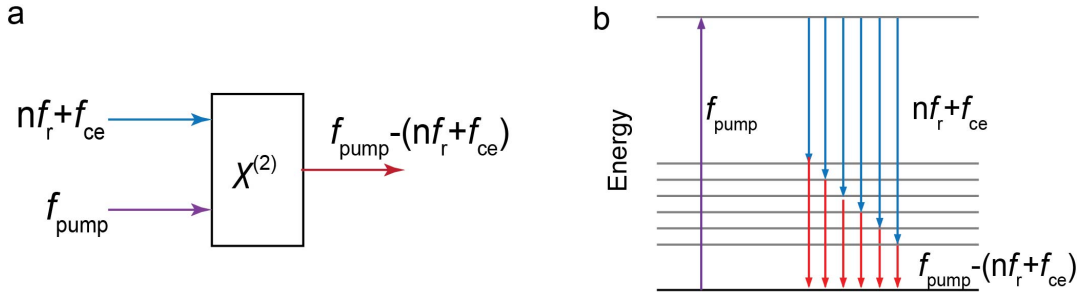


Figure 5.2: **Principle of difference frequency generation between a single-frequency laser and a frequency comb.**

a. The geometry of the nonlinear frequency interaction [32, 125]. In a medium with appropriate  $\chi^{(2)}$  second-order nonlinearity, mixing a single-frequency laser ( $f_{\text{pump}}$ ) and a frequency comb ( $nf_r + f_{\text{ce}}$ ), leads to the generation of the idler comb,  $f_{\text{pump}} - (nf_r + f_{\text{ce}})$ .

b. Energy-diagram description. The single-frequency pump laser excites the atoms to a high virtual level. Stimulated by the signal comb, this level decays with a two-photon emission process. One pump photon is split into a photon of the signal comb and a photon of the idler frequency comb.

process, resulting in the waste of signal photons. Nevertheless, because of the simplicity of the implementation of this technique, and for avoiding detector nonlinearities, mid-infrared combs with high average power are not required, we retain this scheme. With quasi-phase-matched commercial nonlinear crystals [125], sufficient idler comb power can be obtained without significant efforts.

In our implementation, the frequency of the continuous-wave pump laser is stabilized against the master comb. The beam of the pump laser is split into two parts. Each part is used as the pump to generate a mid-infrared idler comb with an erbium signal comb. The repetition frequency of the resulting idler comb remains the same as that of the signal comb, while its carrier-envelope offset frequency is shifted by the amount of  $f_{\text{pump}}$  (modulo  $f_r$ ). Because two idler combs share the same pump laser, their carrier-envelope-offset frequency is shifted by the same amount; the dual-comb phase instability induced by the pump laser is canceled out. Therefore, the mutual coherence of the near-infrared system is transferred to the two mid-infrared combs.

### 5.3 Experimental setup

The performance of the mid-infrared feed-forward dual-comb spectrometer is investigated with an experimental setup displayed in Figure 5.3. The original configuration of the feed-forward near-infrared dual-comb system, indicated in the rectangle, has been described in section 3.3. The difference of the repetition frequencies of the two combs is set to 130 Hz in this demonstration.

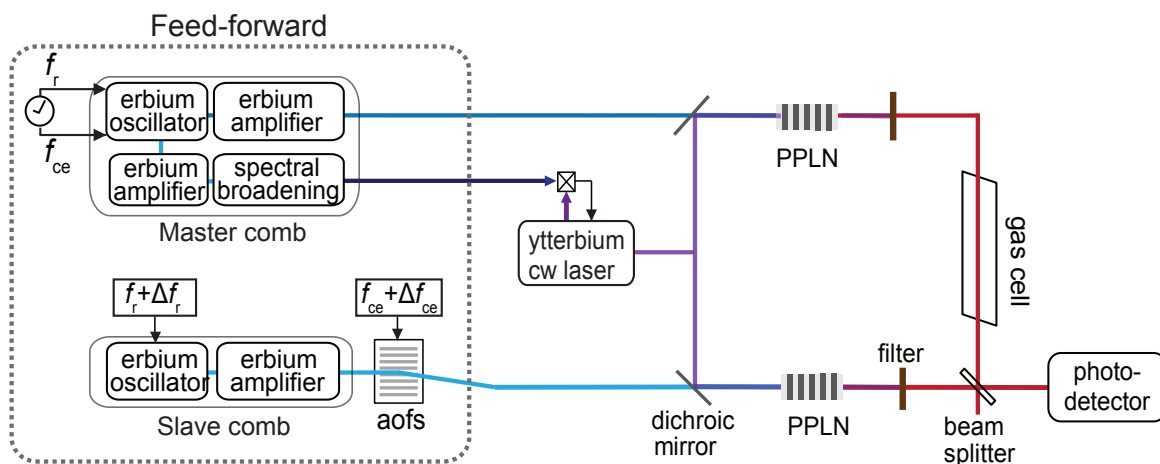


Figure 5.3: **Experimental setup of mid-infrared feed-forward dual-comb spectroscopy.** aofs: acousto-optic frequency shifter; CW: continuous-wave; PPLN: Magnesium-doped periodically poled lithium niobate crystal.

Here, each erbium comb is converted to the mid-infrared region by difference-frequency generation in a Magnesium-doped periodically poled lithium niobate (PPLN) crystal. The pump is a continuous-wave ytterbium-doped fiber laser emitting at  $f_{\text{pump}}=281.8$  THz

(1063.8 nm) with a linewidth of 50 kHz (at 100- $\mu$ s integration time). Its frequency is phase locked to a line of the master comb. The output of the pump laser is split into two beams. Each beam with 2-W average power is superimposed on the amplified erbium comb beam using a dichroic mirror, and the combined beam is focused onto one of the poling channels of the PPLN crystal, which has a length of 3 mm and seven poling periods around 30.5  $\mu$ m. The spectrum resulting from the difference frequency generation is shown in Figure A.8. The span of the idler comb is about 8.2 THz, which is limited by the phase-matching bandwidth of the PPLN crystal. The center frequency of the idler comb can be tuned from 82 THz to 100 THz by changing the temperature or the poling period of the crystal. A long-wavelength-pass optical filter filters out the residual pump and the signal lasers after the crystal. The power of the idler comb increases with the pump power (Fig. A.8b), and it exceeds 90  $\mu$ W at the pump power of 2 W.

In the dual-comb interferometer, the arm of the master idler comb passes through a single-pass gas cell of a length of 70 cm. The two idler beams are then combined using a pellicle beamsplitter. One output of the beamsplitter is focused onto a fast thermoelectrically cooled HgCdTe detector. For avoiding the detector nonlinearities, the total power falling on the detector is kept below 40  $\mu$ W. The interference signal of the two combs is electronically filtered, amplified, and digitized. Due to the limited power onto the detector, obtaining a good signal-to-noise ratio over broad spectral bandwidth requires an integration time of several minutes. To implement time-domain averaging, the experimental conditions are set  $\Delta f_{ce}=0$  (or  $\Delta f_{ce}$  as an integer multiple of  $\Delta f_r$ ) to keep the individual interferograms identical. When averaging, we add up all the experimental interferograms directly without implementing any numerical corrections to the interferograms or the spectra. The averaged interferogram is computed with a complex Fourier transform to reveal the amplitude and phase of the spectrum. During the measurements, the radio-frequency parameters ( $f_r$ ,  $f_{ce}$ , and  $\Delta f_r$ ) of the two near-infrared combs, the absolute frequency of the pump ytterbium laser at 281.8 THz, and that of the erbium laser at 189 THz (used for the feed-forward driver signal generation, see Chapter 3), are counted to calibrate the frequency scale of the dual-comb spectra.

## 5.4 Experimental results

An interferometric sequence with nineteen interferograms in the region of the  $\nu_9$  and  $\nu_{11}$  bands of ethylene is shown in Figure 5.4a. In the laboratory time frame, the individual interferograms repeat with a period of  $1/\Delta f_r=7.7$  ms, corresponding to an optical delay of  $1/f_r=10$  ns (Figure 5.4b). A magnified view in Figure 5.4c of the region surrounded by a

red rectangle in Figure 5.4b displays the characteristic modulations induced by the  $^{12}\text{C}_2\text{H}_4$  transitions. The signal-to-noise ratio enables revealing modulations up to optical delays of more than four nanoseconds, corresponding to the inverse of the Doppler width of the molecular transitions.

A broadband mid-infrared dual-comb spectra with resolved comb lines around 92 THz, resulting from the interferogram of Figure 5.4a, is shown in Figure 5.5. It spans 8.2 THz with 82,000 comb lines (Figure 5.5a). In Figure 5.5b, a magnified view of the spectrum shows a Doppler-broadened line of the  $\nu_9$  band of  $^{12}\text{C}_2\text{H}_4$ , sampled by the comb lines with 100-MHz spacing. The individual comb lines (Figure 5.5c) appear with the expected instrumental profile, sinc function, with a transform-limited full-width at half maximum (FWHM) of 6.8 Hz in the radio-frequency domain. The instrumental line shape in the comb lines is resolved, illustrating the relative phase stabilities between the two mid-infrared combs.

The spectrum (in Figure 5.6a) with a resolution of the comb-line spacing (100 MHz) shows the absorption lines of ethylene over the entire measured span. Ethylene ( $^{12}\text{C}_2\text{H}_4$ ) is a near-prolate planar asymmetric-top molecule. In a single recording without tuning the center frequency, the spectral bandwidth covers the region of the  $\nu_9$  and  $\nu_{11}$  stretching modes of  $^{12}\text{C}_2\text{H}_4$ , where the  $\nu_2 + \nu_{12}$ ,  $2\nu_{10} + \nu_{12}$ , and  $\nu_9 + \nu_{10}$  cold bands are observed. Figure 5.6b illustrates the transmittance and phase spectra. A magnified view in the region of a  $Q$ -branch of the  $\nu_9$  band is shown in Figure 5.6c, exemplifying the resolved rovibrational lines. For a measurement time of 1,742 s, the signal-to-noise ratio peaks 1,275 in the region around 92.5 THz (corresponding to  $30.5 \text{ Hz}^{1/2}$ ), and its average value across the span of 8.2 THz is 570 ( $13.6 \text{ Hz}^{1/2}$ ). The figure of merit, given by the product of the average signal-to-noise ratio in unit square root of measurement time and the number of spectral elements, is  $1.1 \times 10^6 \text{ Hz}^{1/2}$ , which is comparable with the best results reported in the same spectral region, such as narrowband [62, 63], and phase-reconstructed broadband [64] dual-comb spectroscopy.

The center frequency of the spectrum can be optimized to the absorption of different molecules by changing the temperature or the poling period of the PPLN crystals. The comb lines are resolved across the entire tunable spectral range (82–105 THz). As an example, the spectrum is centered at around 98 THz for the measurement of the  $\nu_3$  fundamental band of  $^{12}\text{C}_2\text{H}_2$ , depicted in the Appendix Fig. A.9 with resolved comb lines. In Figure 5.7a, the spectrum sampled at the comb-line positions has a signal-to-noise ratio of 1,360 at around 98.4 THz and an average signal-to-noise ratio of 500 across the span of 8 THz. The transmittance and phase spectra of the  $\nu_3$  band of  $^{12}\text{C}_2\text{H}_2$  are shown in Figure 5.7b, where the strong lines belong to the  $\nu_3$  and  $\nu_2 + (\nu_4 + \nu_5)_+^0$  cold bands of  $^{12}\text{C}_2\text{H}_2$ , and

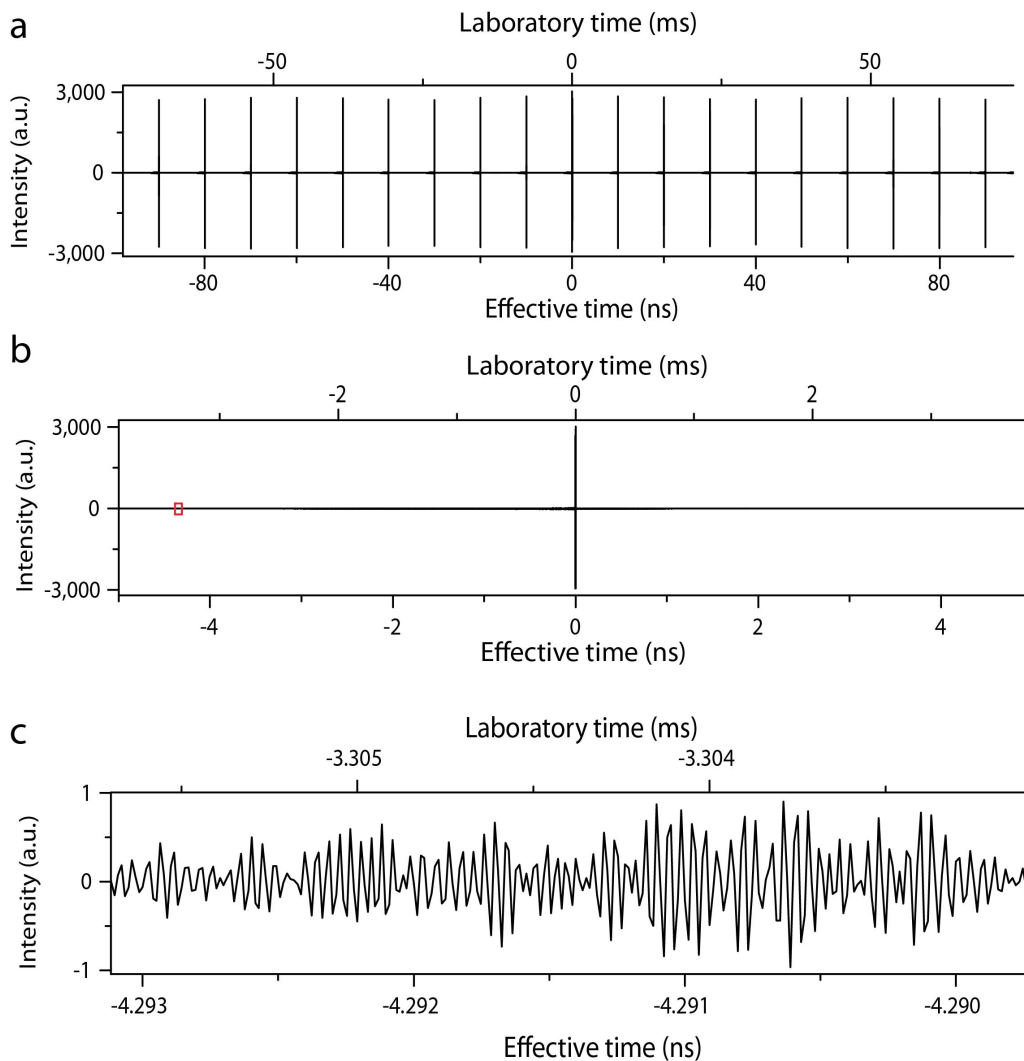


Figure 5.4: **Feed-forward mid-infrared dual-comb interferogram.**

a. an averaged time sequence with 19 individual interferograms. Its total measurement time is 29 min, resulting from 11,920 averages of continuous recordings, each with a laboratory time of 0.146 s.

b. a magnified view with an averaged interferogram in a sampling period (10 ns in the effective time scale and 7.7 ms in the laboratory scale).

c. a magnified view of the region indicated by the red rectangle of **b** with the characteristic molecular modulations.

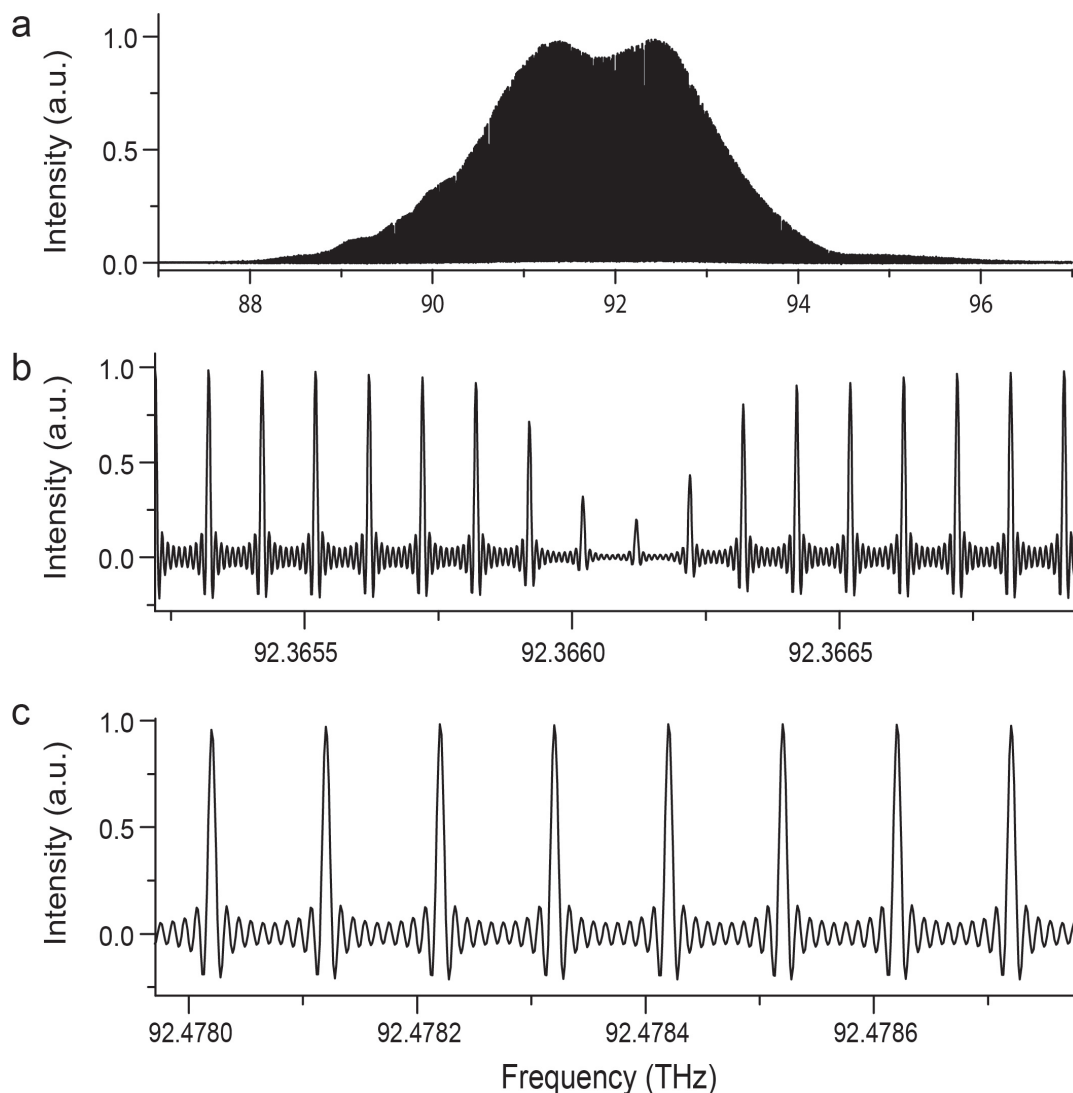


Figure 5.5: **Experimental mid-infrared dual-comb spectrum at around 92 THz with resolved comb lines.**

a. Apodized spectrum in the full spectral bandwidth of 8.2 THz, measured within 29 min and computed with a complex Fourier transform with 6-fold zero filling.

b. Magnified unapodized representation of **a** showing a Doppler-broadened molecular line ( $J=13, K_a'=1, K_c'=13$ )-( $J''=14, K_a''=0, K_c''=14$ ) in a *P*-branch of the  $\nu_9$  band of  $^{12}\text{C}_2\text{H}_4$ . The gas pressure is 146.7 Pa and the absorption path length is 70 cm. In the line assignments,  $K_a$  and  $K_c$ , respectively, denote the quantum number of the projection of the rotational angular momentum to the inertial axis of the smallest and largest moment.  $J$  is the rotational quantum number. The prime and double primes labels the upper state and lower state of the transition, respectively.

c. Magnified unapodized view of **b** showing eight individual comb lines convolved with the cardinal-sine instrument line shape.

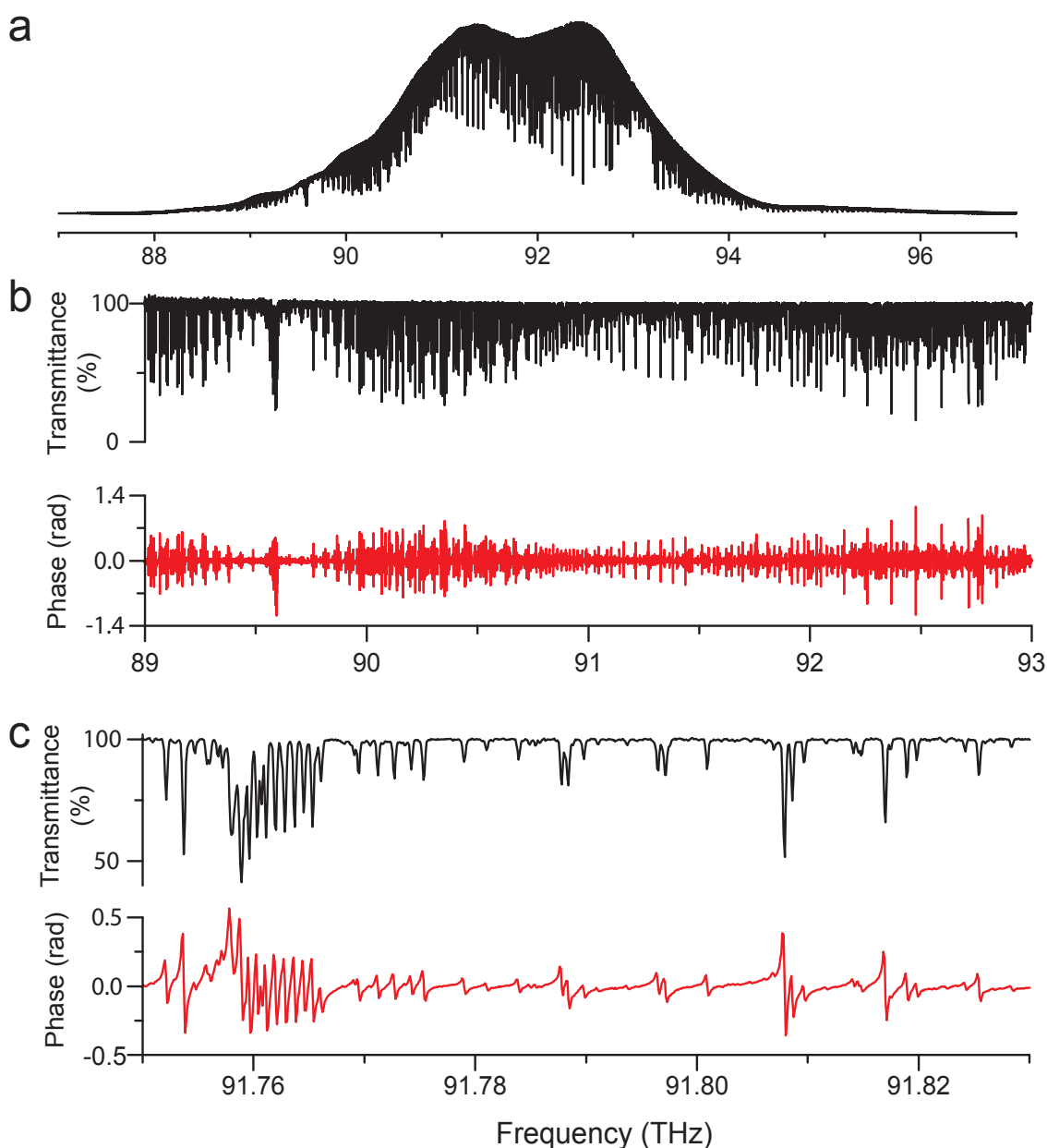


Figure 5.6: **Experimental spectrum in the region of the  $\nu_9$  and  $\nu_{11}$  fundamental bands of  $^{12}\text{C}_2\text{H}_4$  around 92 THz.**

a. The entire spectrum spans 8.2 THz, and it is measured within 29 min. The resolution of the spectrum is 100 MHz, corresponding to the spacing of the comb lines.

b. Transmittance and phase spectra of the  $\nu_9$  and  $\nu_{11}$  band of  $^{12}\text{C}_2\text{H}_4$ . The baseline is corrected with a third-order polynomial fit.

c. Magnified view of **b** in the region at around 91.8 THz. The lines in the  $Q$ -branch of the  $\nu_9$  band are assigned  $J'-J''=0$ ,  $K_a'=5$ ,  $K_a''=6$ , and  $K_c'-K_c''=1$ .

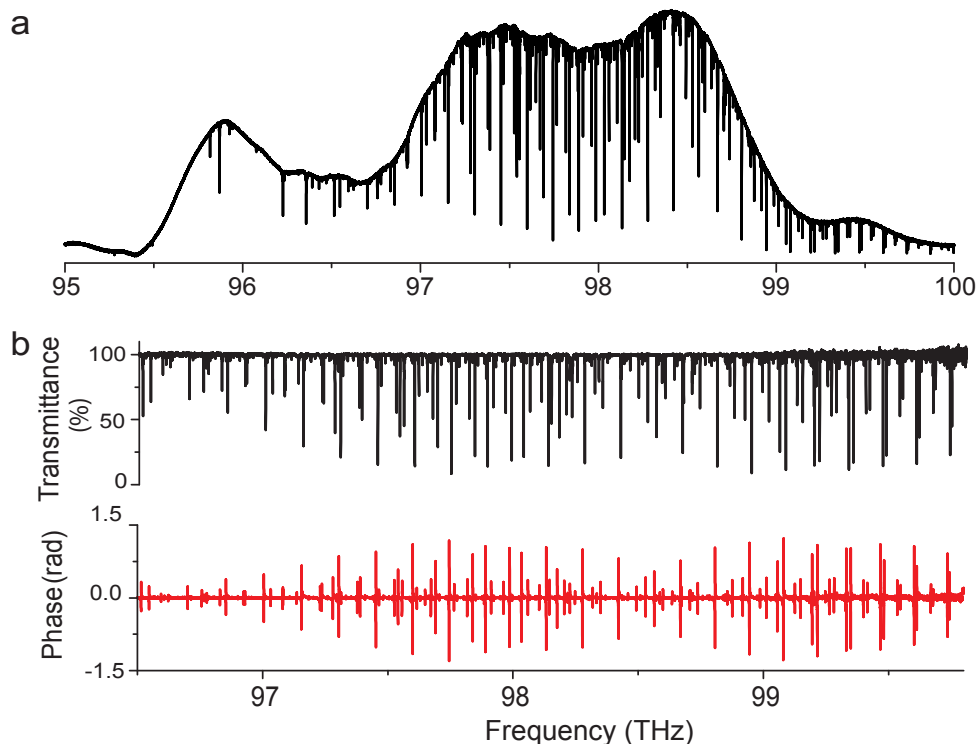


Figure 5.7: **Experimental spectrum in the region of the  $\nu_3$  fundamental band of  $^{12}\text{C}_2\text{H}_2$  with a resolution of 100 MHz, measured within 34.2 min.** a. A portion of the spectrum shows the  $\nu_2+\nu_4+\nu_5$  combination band and the  $P$ -branch of the  $\nu_3$  fundamental band of  $^{12}\text{C}_2\text{H}_2$ . The acetylene sample is in natural abundance with a pressure of 10.7 Pa and an absorption path length of 70 cm. b. Transmittance and phase spectra of the  $\nu_3$  and  $\nu_2+\nu_4+\nu_5$  band of  $^{12}\text{C}_2\text{H}_2$ .

the weak lines are assigned to the  $\nu_3+\nu_4^1-\nu_4^1$ ,  $\nu_2+(2\nu_4+\nu_4)^1\Pi-\nu_4^1$ ,  $\nu_2+(2\nu_4+\nu_5)^1\Pi-\nu_5^1$  hot bands. The rotational assignments can be found in Ref [126].

The evolution of the signal-to-noise ratio in the acetylene spectrum (Fig. 5.7) with the measurement time is shown in Figure 5.8. The signal-to-noise ratio increases as the square root of the measurement time, which is the expected trend for coherent averaging. The linear behavior in Fig. 5.8 has not reached its limit at the maximum measurement time of 2,052 s, suggesting that the mutual coherence between two mid-infrared combs can be obtained for longer times. Similar behavior is also observed in the ethylene spectrum (Figure 5.6). Such a coherence time is experimentally achieved without any other corrective treatment of phase errors. It is three orders-of-magnitude longer than that of the state-of-the-art dual-comb systems, where a mutual coherence of 1 second represents an excellent figure.

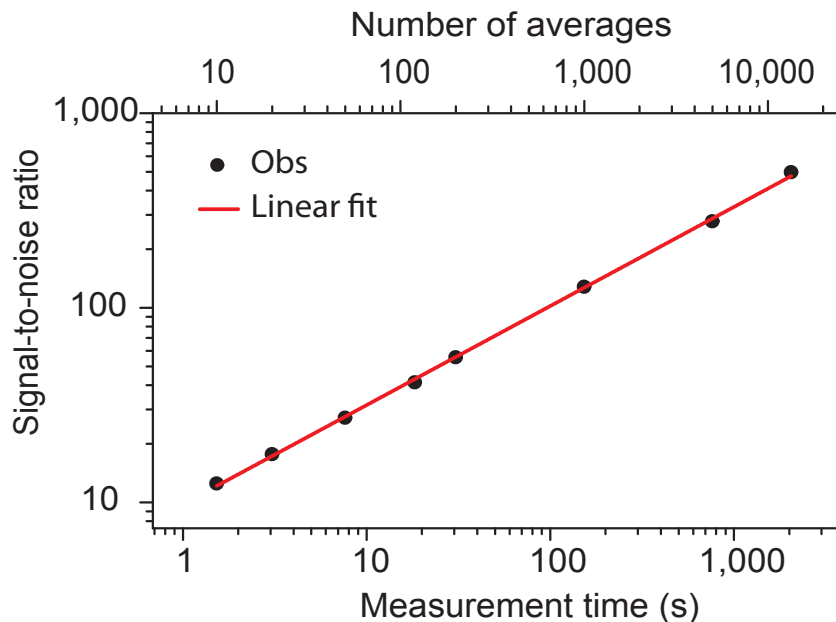


Figure 5.8: **Evolution of the average signal-to-noise ratio in the experimental mid-infrared dual-comb spectra over 2,000 s.** The interferograms, each with duration of 0.153 s, are averaged and Fourier transformed to obtain dual-comb spectra. The average signal-to-noise ratio in the spectra (with 100-MHz resolution) is measured for different measurement times. In the logarithmic scale, a linear fit with a fitted slope of 0.509(5) indicates the signal-to-noise is proportional to the square root of the measurement time.

For a preliminary analysis, we fitted a limited number of molecular lines in the self-referenced experimental dual-comb spectra to determine their frequency. In the ethylene spectrum (Figure 5.6), the lines of the  $\nu_9$  band of  $^{12}\text{C}_2\text{H}_4$  with an FWHM of about 215 MHz are satisfactorily sampled by the resolved comb lines of 100-MHz spacing. The result of the least-squares fit of Doppler profiles to the experimental lines is exemplified in Figure 5.9. The “Obs-Fit” residuals with a standard deviation of 0.12% do not exhibit any systematic signatures above the noise. We select 250 lines that are well isolated and we compare the retrieved line positions to the literature data, in Appendix Table B.3–B.6. For a measurement time of about half an hour, the average statistical uncertainty of our measurement is about 0.8 MHz, with a standard deviation of 0.4 MHz. In an extensive line list on HITRAN 2016 [113], which reproduces the report of [127], the precision of the position of most lines is listed better than 20 MHz, and the accuracy is stated as “slightly worse”. The mean value of the discrepancies between this work and those of HITRAN is  $-240$  kHz with a standard deviation of 1 MHz. In Appendix Table B.4, about sixty lines in the  $\nu_{11}$  band are compared with ref. [128], in which the lines are measured with an

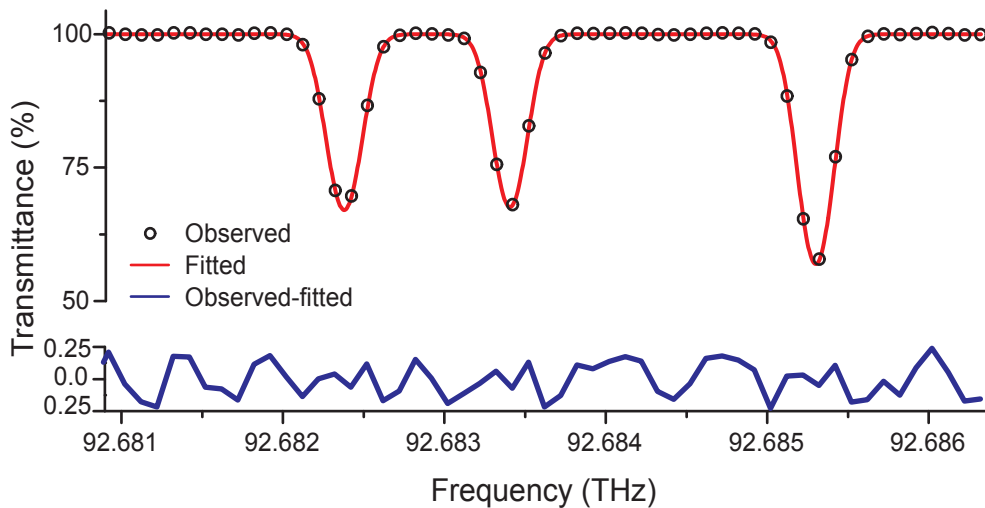


Figure 5.9: **Portion of the experimental transmittance spectrum of ethylene and the fitted molecular profiles.** The measurement time of the spectrum is 29 min. The gas pressure is 146.7 Pa, and the absorption path length is 70 cm. The Doppler-broadened FWHM of the lines is approximately 215 MHz. The maximum absorption goes down to 50%. The “obs-fit” residuals are within 0.25% with a standard deviation of  $1.2 \times 10^{-3}$ .

accuracy of  $\pm 18$  MHz. The average discrepancy between ref.[128] and our measurement is 1.0 MHz, with a standard deviation of 3 MHz. This indicates that our feed-forward dual-comb technique, with frequency scale calibrated directly to the hydrogen maser, provides a potential for Doppler-limited molecular line position measurements. However, the related line parameters of the samples in the experiment, such as the pressure shifts, have not been experimentally determined, which will be the main object of our future investigations, therefore no line positions can be provided at this point.

## 5.5 Conclusion and discussion

In this chapter, the feed-forward dual-comb technique is extended to the molecular fingerprint region. For the first time, broadband mid-infrared spectroscopy with self-calibrated frequency scales is demonstrated with a negligible contribution of the instrumental line shape, without any types of phase correction required. While maintaining a relatively simple dual-comb experimental setup, a mutual coherence of 2,000 seconds is achieved, exceeding the state-of-the-art techniques by three orders of magnitude. Moreover, compared to the techniques of stabilizing the two combs to optical references [62, 64], the feed-forward scheme does not involve any referencing cavities or continuous-wave lasers with linewidth at the Hertz level. As discussed in Chapter 2, phase correction is not al-

ways implementable and may induce subtle artifacts degrading the precision. Therefore, such a system without any data correction will open new prospects to broadband precision molecular spectroscopy, and it will help to identify the systematic instrumental artifacts and ascertain the precision frontiers.

This spectrometer provides self-calibrated frequency scale and resolves molecular profiles with negligible instrumental line width, which is well suited for the line shape analysis. The major contribution to the instrumental profile arises from the optical lines of the master comb that interrogates the sample. In this work, the master comb is self-referenced with a linewidth of 100 kHz (at 1-min integration time), which is three orders of magnitude narrower than the Doppler-broadened molecular profiles (at room temperature). The molecular profiles in the spectra can be directly fitted, potentially resulting in line parameters with improved precision.

A limitation of this scheme is the low average power of the mid-infrared idler combs. The power obtained (about 100  $\mu\text{W}$ ) is suitable for spectroscopy with a single-pass cell or a multi-pass cell of a small number of reflections because the power falling onto the detector should be kept 30–40  $\mu\text{W}$  to avoid detector nonlinearities. For experiments with a long absorption path or with a high-finesse cavity, the efficiency of difference-frequency generation could be improved by chirping the signal pulses to several picoseconds for an improved temporal overlap between the signal pulses and the pump laser. For further addressing the low output power issue, the mid-infrared combs based on optical parametric oscillators or difference frequency generation between two laser systems should be harnessed; using an external actuator, the feed-forward control of relative phase fluctuations could be implemented in the mid-infrared region.

With the current configuration, the spectrum bandwidth covers 81–106 THz (2.8–3.7  $\mu\text{m}$ ). Broader tunable spectral bandwidth over the entire atmospheric window 60–100 THz (3–5  $\mu\text{m}$ ) is achievable by spectrally broadening the output of the erbium combs [23]. To access the lower frequency ranges, such as the 21–37 THz (8–14  $\mu\text{m}$ ) domain, a tunable continuous-wave laser as pump laser, or intra-pulse difference frequency generation in a semiconductor (e.g., orientation-patterned gallium phosphide [129]) could be harnessed.

This feed-forward dual-comb spectroscopy at the 3- $\mu\text{m}$  region demonstrates the potential of phase-stable dual-comb interferometer in the molecular fingerprint region. Future work of precision spectroscopy of molecular line shapes will be explored.

# Chapter 6

## Summary and Outlook

In this thesis, phase-stabilized dual-comb spectroscopy is first demonstrated in the near-infrared region. Its versatility is illustrated with the demonstration of gas-phase attenuated-total-reflectance spectroscopy over broad spectral bandwidth. Furthermore, we extended it to the 3- $\mu\text{m}$  mid-infrared region. The results and prospects of this thesis are summarized in this chapter.

**Chapter 3** has described an original dual-comb approach, which addresses one of the main difficulties of dual-comb instrumentation: the demanding requirement of preserving the relative phase coherence between the two frequency combs during measurements. Established by means of acousto-optic feed-forward control of the relative carrier-envelope offset frequencies, mutual coherence between two mode-locked femtosecond erbium-fiber frequency combs is maintained during about 2,000 seconds without any computer-based corrective processing of phase errors. The experimental achieved coherence is more than three orders of magnitude longer than that of the previous best result [22]. The absence of saturation in the evolution of the signal-to-noise ratio versus time suggests that such a phase control in a dual-comb interferometer might offer arbitrarily long measurement times.

This achievement opens new prospects for broadband high-precision spectroscopy and metrology. For instance, this dual-comb technique should be capable of resolving comb lines of narrow spacing (e.g., based on frequency combs with line spacing lower than 1 MHz rather than the 100-MHz combs in the present demonstration), leading to improved spectral resolution; such an accomplishment will speed up the development of Doppler-free spectroscopy over broad spectral bandwidths [35]. Coherent averaging can be performed to improve the signal-to-noise ratio in the dual-comb spectra, therefore this technique may become suited for the measurement of weak molecular lines. The extended measurement

times that are reached can be harnessed to study some interesting properties of substance, such as characterization of refractive index [75] or investigation of molecular chirality.

As it employs a fast and compact external actuator, this dual-comb technique can be used with any types of frequency comb source, including semiconductor lasers [53, 61] and micro-resonator combs [66, 93]. Further development might provide solutions to dual-comb spectroscopy in spectral regions where its development is still challenging, such as the ultraviolet and the mid-infrared regions.

**Chapter 4** exploits phase-stabilized dual-comb spectroscopy for attenuated-total-reflectance analysis of gases in small amounts. Using a center-tapered fiber of subwavelength diameter for sample interrogation, the broadband dual-comb spectrometer simultaneously resolves absorption and dispersion features of multiple gas molecules in volumes as little as 25 picolitres, with the capability of diagnosing molecular amounts below 0.3 femtomoles within a measurement time of 1 second. The consistency and precision of the spectra are preserved by the coherent multi-heterodyne acquisitions.

The technique could be exploited for analyzing samples in small quantities, e.g., local detection of gas leakage [115], or observation of small amounts of gases released from chemical reactions (e.g., microgasometry [130]), etc. In this demonstration, the line spacing of the comb sources is about 100 MHz, which is suited for gas analysis at low pressure (e.g., with Doppler-broadened line profiles). For future applications, e.g., analyzing gases at atmospheric pressure with a linewidth of several GHz, the line spacing of the dual-comb system should be chosen to match the resolution required in the spectra for avoiding the waste of measurement times [55].

With future development to waveguide fabrication technology, the technique could be implemented in the mid-infrared domain on strong fundamental transitions to reduce the minimum detectable number of molecules. This work explores the potential of dual-comb spectroscopy with evanescent-wave sample interaction. Currently, on-chip frequency comb sources are in active development [131]; in a long term vision, the light sources, the sample interrogation part, and the detection unit might be fully integrated.

**Chapter 5** explores the potential of phase-stabilized dual-comb spectroscopy in the mid-infrared region. The light of the feed-forward dual-comb spectrometer is frequency converted by difference frequency generation to the mid-infrared region around 3  $\mu\text{m}$ . The mutual coherence between two mid-infrared combs is experimentally preserved over 2,000 seconds. A signal-to-noise ratio over 1,000 is obtained, and comb lines are resolved over the spectral range of tunability (82-100 THz). This allows self-calibration of the frequency

scale and negligible contribution of the instrumental line shape to the Doppler-broadened profiles of small molecules at room temperature.

All these features are simultaneously achieved with a relatively simple experimental setup of coherence control; this set-up does not require complex computer hardware and programming for phase reconstruction or ultra-stable cavities for phase referencing. Because phase correction is not needed, the technique provides opportunities to further ascertain the frequency precision and examine systematic artifacts. In this demonstration, the instrumental line width, which is ultimately determined by the width of the interrogation comb lines (on the order of 100 kHz at the measurement time of 1 min), has a negligible contribution to the Doppler width (a few hundreds of MHz) of the molecular transition. Therefore, the intrinsic molecular profiles can be accessed and directly fitted with appropriate spectral profiles. In the future, by harnessing spectrally-broadened signal combs or tunable CW pump laser in the difference frequency generation process, the spectral coverage could be extended to lower frequencies.



# Appendix A

## Appendix Figures

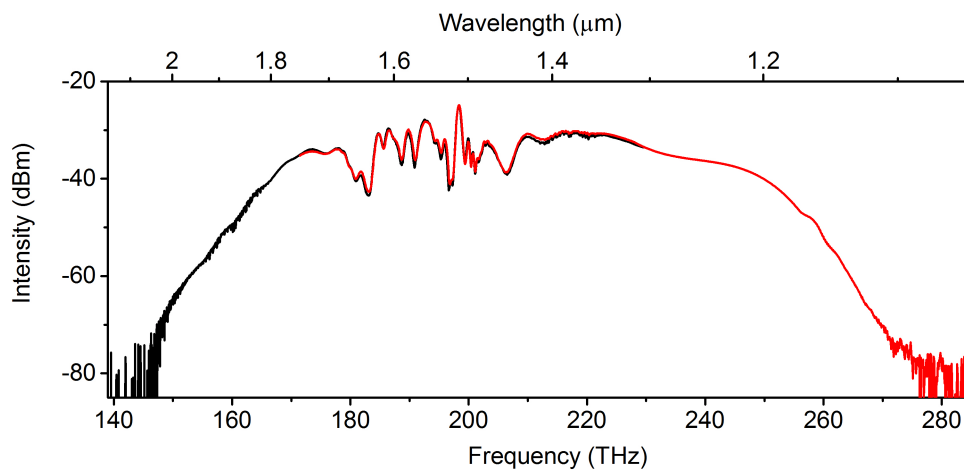


Figure A.1: **Spectral broadening of an erbium comb in a highly nonlinear fiber.** The output of each erbium laser comb is amplified to 300 mW and launched into a piece of highly nonlinear fiber for spectral broadening. The length of the highly nonlinear fiber is 7 cm, and its nonlinear coefficient is  $10.7 \text{ (W} \cdot \text{km)}^{-1}$ . The resulting spectrum spans close to an octave.

The spectrum is measured with two different optical spectral analyzers: one covers 140–230 THz (in black), and the other records the range of 170–280 THz (in red). The resolution is 1 nm.

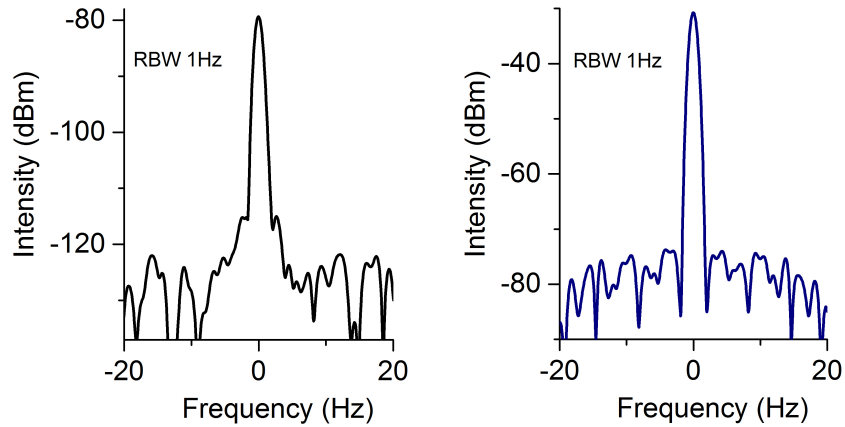


Figure A.2: **Radio-frequency power spectrum of the phase-locked in-loop beat signals.** After the phase stabilization, the two beat signals  $f_{\text{beat1}}$  and  $f_{\text{beat2}}$  are measured to preliminary indicate the relative stability. The center frequency of each beat note is detuned to zero frequency. The 3-dB linewidth of each beat note is 1 Hz, limited by the resolution bandwidth of the spectral analyzer. RBW: resolution bandwidth

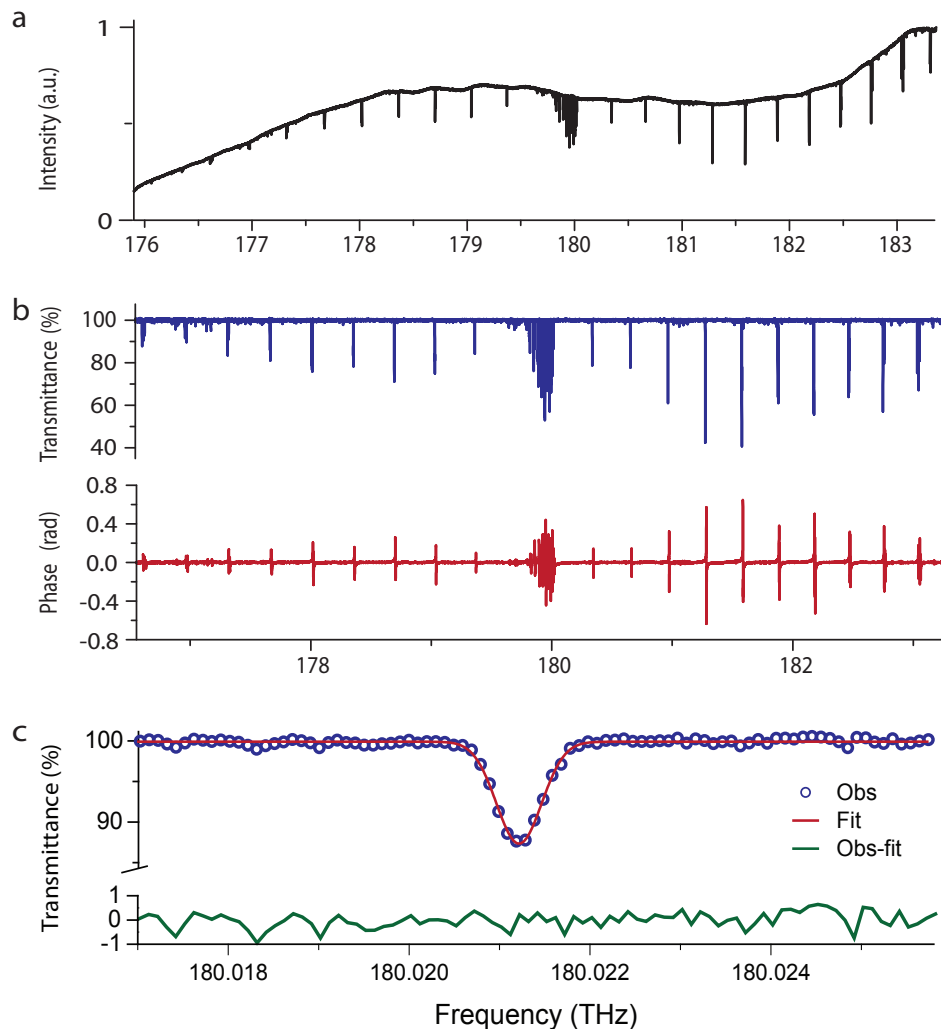


Figure A.3: **Experimental feed-forward dual-comb spectrum in the 180-THz region with a resolution of 100 MHz.** **a.** The spectrum in the region of the  $2\nu_3$  band of  $^{12}\text{CH}_4$  spans 9 THz and the data recording time is 14.46 s. The absorption path length of the sample is 70 cm, and its gas pressure is 1,067 Pa. **b.** The experimental transmittance and phase spectra of the  $2\nu_3$  band of  $^{12}\text{CH}_4$ . **c.** Transmittance spectrum with the  $Q(1)$  line of the  $2\nu_3$  band and its fitted result. The maximum absorption is about 13% at the line center. The Doppler full width at half maximum of the  $Q(1)$  line at 295 K is approximately 554 MHz. The experimental profile is fitted by a Doppler line shape. The “observed–fitted” residuals are at the noise level with a standard deviation of 0.3%.

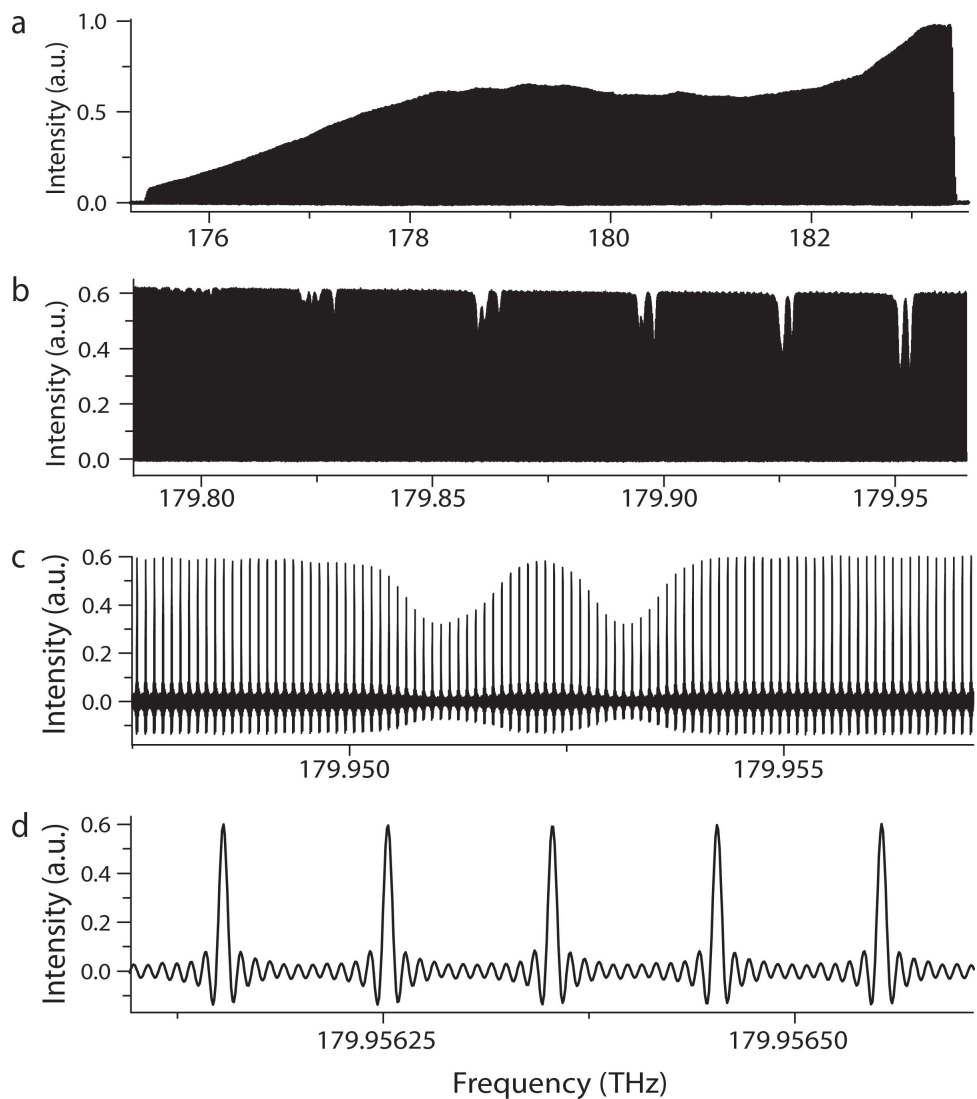


Figure A.4: **Experimental dual-comb spectra with resolved comb lines in the region of the  $2\nu_3$  band of  $^{12}\text{CH}_4$  around 180 THz.** The spectra are displayed apodized in **a.** and unapodized in **b,c,d.** The measurement time is 14.46 s. **a.** The entire span covers 9 THz. **b.** A portion of the spectrum shown in **a.** with some of the multiplets in the  $Q$ -branch of the  $2\nu_3$  band of  $^{12}\text{CH}_4$ . **c.** Magnified view of the  $Q(6)$  manifold. **d.** Magnified view of five individual comb lines.

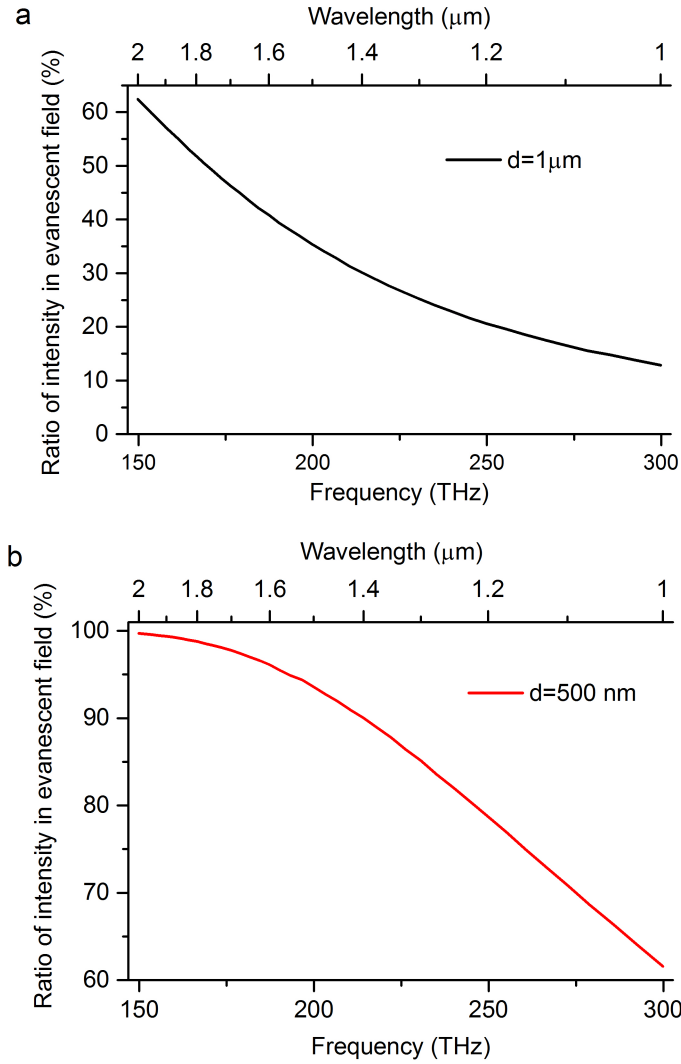


Figure A.5: **The evolution of the fraction  $\eta(f)$  of total light intensity propagating in the evanescent field with laser frequencies.** The intensity distribution of the vacuum-clad tapered fibers at different laser frequencies is calculated (as in Fig. 4.2). For each frequency, the intensities inside ( $I_{\text{in}}$ ) and outside ( $I_{\text{out}}$ ) the core, are integrated to retrieve the ratio  $\eta(f) = I_{\text{out}} / (I_{\text{in}} + I_{\text{out}})$ . In **a** and **b**,  $\eta(f)$  is calculated for the fiber diameter of  $1\mu\text{m}$  and  $500\text{ nm}$ , respectively.

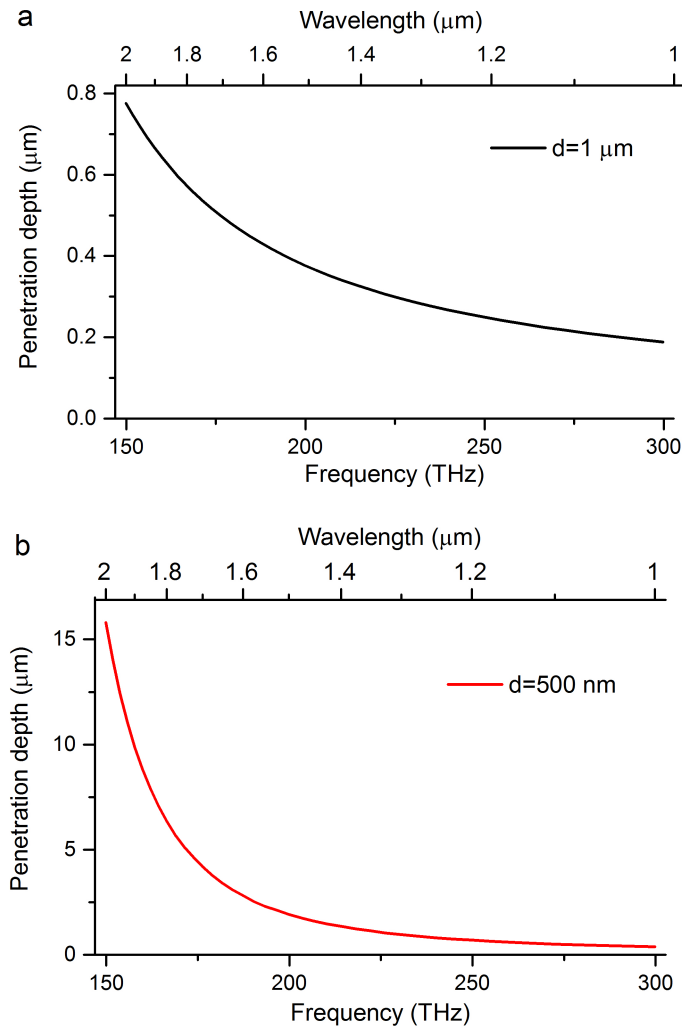


Figure A.6: Penetration depth of the evanescent field around a tapered fiber at different guided laser frequencies. The results for the fiber with the diameter of 1  $\mu\text{m}$  and 500 nm are in **a** and **b**, respectively. The penetration depth increases with the wavelengths.

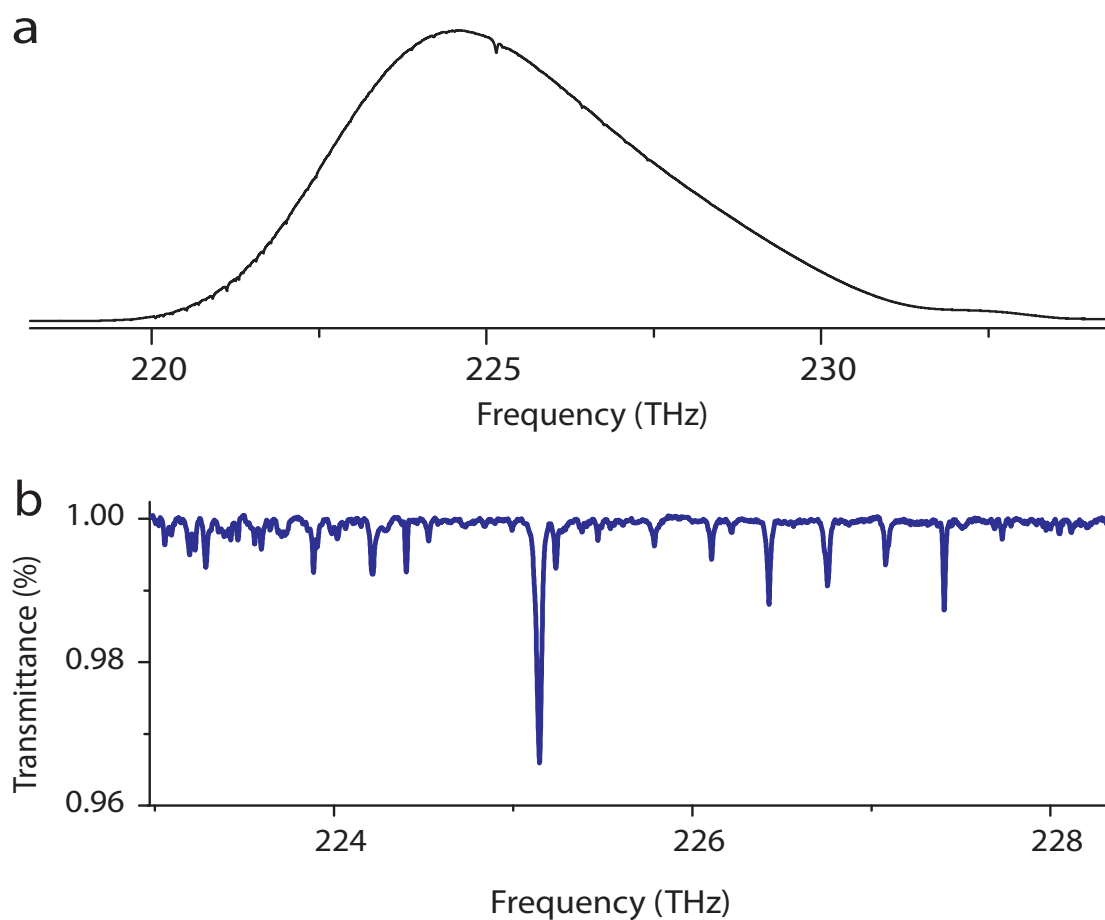


Figure A.7: **Dual-comb attenuated-total-reflection spectrum at around 225 THz with the  $\nu_2 + 2\nu_3$  band of  $\text{CH}_4$ .**

**a.** The resolution is 2 GHz and its total experimental time is 480 s (only 24-s data contributes to acquiring useful molecular spectrum). A tapered fiber provides an equivalent absorption path length of about 17 mm, and the gas pressure is 97.14 kPa. The FWHM of the molecular lines are broadened to more than 6 GHz.

**b.** A portion of transmittance spectrum at around 225 THz shows the  $\nu_2 + 2\nu_3$  band of  $^{12}\text{CH}_4$ . The maximum absorption is only less than 4%.

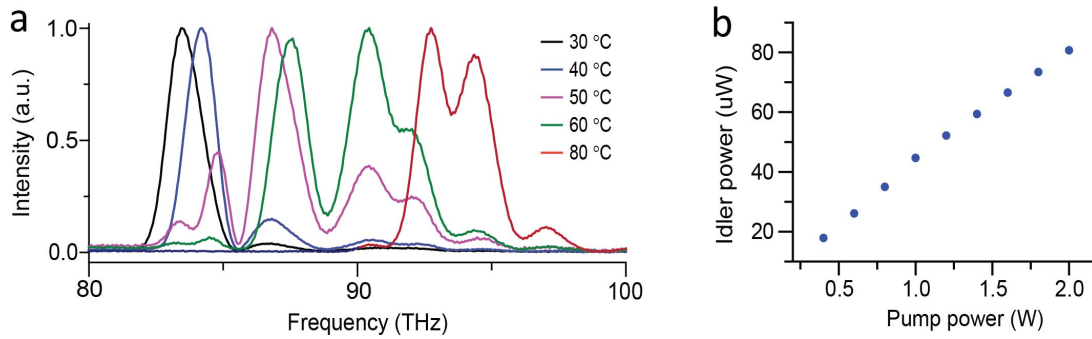


Figure A.8: **Result of mid-infrared frequency comb generation.**

**a.** The spectra of generated mid-infrared idler frequency comb. They are recorded by a Fourier spectrometer with a resolution of 30 GHz. The center frequency is tuned by changing the temperature of the PPLN crystal.

**b.** The idler comb power increases with the increasing pump power.

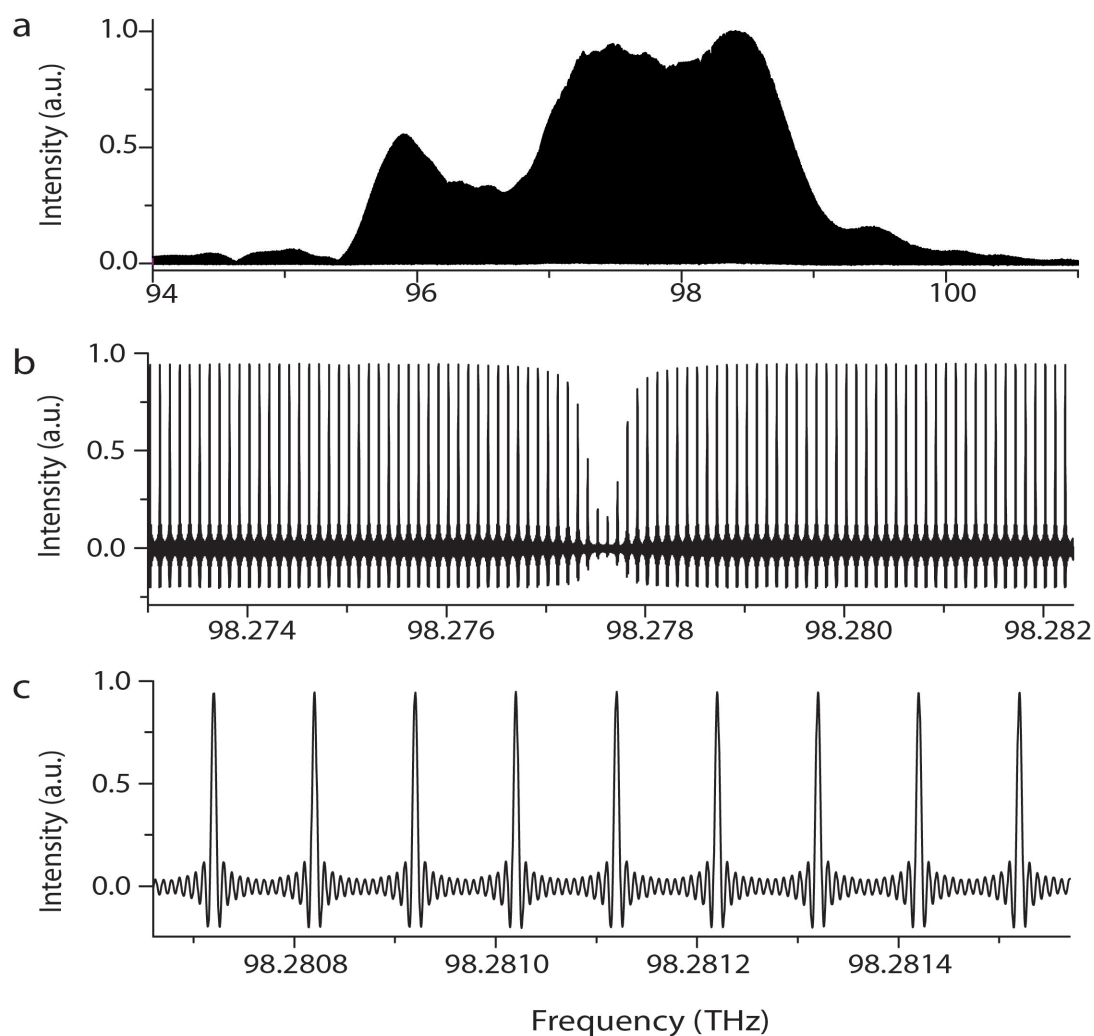


Figure A.9: **Mid-infrared dual-comb spectrum with resolved comb lines in the region of the  $\nu_3$  band of  $^{12}\text{C}_2\text{H}_2$  around 98 THz.** The measurement time of the spectrum is 34.2 min, resulting from 13,400 averages of consecutive interferograms of 153-ms duration. The spectrum is displayed apodized in **a** and unapodized in **b,c**.

**a.** A portion of the spectrum spans about 7 THz.

**b.** Magnified view of the line  $P(7)$  of the  $\nu_3$  fundamental band of  $^{12}\text{C}_2\text{H}_2$ .

**c.** Magnified view of nine individual comb lines. The expected instrumental line shape convolves the comb lines.



# Appendix B

## Appendix Tables

### B.1 List of experimental molecular line positions of Chapter 3

The  $\nu_1 + \nu_3$  band of  $^{12}\text{C}_2\text{H}_2$  (Table B.1.)

The  $2\nu_3$  band of  $^{12}\text{CH}_4$  (Table B.2)

### B.2 Experimental molecular line positions of Chapter 5

The  $\nu_9$  band of  $^{12}\text{C}_2\text{H}_4$  (Table B.3)

The  $\nu_{11}$  band of  $^{12}\text{C}_2\text{H}_4$  (Table B.4)

The  $\nu_2 + \nu_{12}$  band of  $^{12}\text{C}_2\text{H}_4$  (Table B.5)

The  $2\nu_{10} + \nu_{12}$  band of  $^{12}\text{C}_2\text{H}_4$  (Table B.6)

Assignment	Frequency (MHz)						
	This work	Pressure shift at 15.2 Pa [87]	This work extrapolated to zero pressure	[88]	[89]	This work- [88]	This work- [89]
$P(14)$	195,500,510.1(5)	-0.40(4)	195,500,510.5(5)	195,500,510.62(15)	195,500,510.7477(101)	-0.1	-0.2
$P(13)$	195,580,979.3(3)	-0.40(4)	195,580,979.7(3)	195,580,979.28(13)	195,580,979.3711(102)	0.4	0.3
$P(10)$	195,817,848.2(4)	-0.42(4)	195,817,848.6(4)	195,817,848.23(15)	195,817,848.3823(105)	0.4	0.2
$P(6)$	196,123,037.7(4)	-0.40(7)	196,123,038.1(4)	196,123,038.51(15)	196,123,038.5214(103)	-0.4	-0.4
$P(5)$	196,197,428.0(2)	-0.42(4)	196,197,428.4(2)	196,197,428.20(13)	196,197,428.3457(102)	0.2	0.1
$P(4)$	196,271,052.2(5)	-0.42(4)	196,271,052.6(5)	196,271,052.46(14)	196,271,052.5819(103)	0.1	0.0
$P(3)$	196,343,910.0(4)	-0.40(4)	196,343,910.4(4)	196,343,910.06(14)	196,343,910.0006(127)	0.3	0.4
$R(1)$	196,696,653.0(4)	-0.20(4)	196,696,653.2(4)	-	196,696,652.9203(100)	-	0.3
$R(7)$	197,094,394.3(3)	-0.42(4)	197,094,394.7(3)	197,094,394.83(15)	197,094,395.0333(104)	-0.1	-0.3
$R(11)$	197,343,962.2(4)	-0.57(4)	197,343,962.8(4)	197,343,962.37(15)	-	0.4	-
$R(17)$	197,694,759.3(3)	-0.81(4)	197,694,760.1(3)	197,694,760.15(15)	-	-0.1	-

Table B.1: Line list of the  $\nu_1 + \nu_3$  band of  $^{12}\text{C}_2\text{H}_2$ . Center frequencies of the lines of the  $\nu_1 + \nu_3$  band of  $^{12}\text{C}_2\text{H}_2$  in this work are retrieved from the spectrum in Fig. 3.7, measured within 31 min. The experimental line positions at zero pressure are corrected (fourth column) for the pressure shift using the measurement values of [87]. The number within parentheses is the uncertainty, which includes statistical and systematic effects, in units of the last digit.

Assignment	Frequency (MHz)			This work- [91]	
	This work	Pressure shift at 1,067 Pa [90]	This work extrapolated to zero pressure		
$R(0)$	180,345,060.9 (25)	-5.51(3)	180,345,066.4(25)	180,345,065.08(37)	1.3
$Q(1)$	180,021,248.7 (32)	-6.11(6)	180,021,254.8(32)	180,021,253.10(61)	1.7

Table B.2: Center positions of the Doppler-broadened lines  $R(0)$  and  $Q(1)$  in the  $2\nu_3$  band of  $^{12}\text{CH}_4$  measured in this work. The measurement time is 14.46 seconds. The frequencies extrapolated to zero pressure is shown in the fourth column, corrected using the pressure shifts measured in [90]. These two lines are the only ones for which accurate measurements (based on Doppler-free saturated absorption spectroscopy) are available in the literature [91]. The number within parentheses is the uncertainty, including statistical and systematic effects, in units of the last digit.

Table B.3: Line positions of the  $\nu_9$  band of  $^{12}\text{C}_2\text{H}_4$ .

$J'$	$K'_a$	$K'_c$	$J''$	$K''_a$	$K''_c$	Observed <sup>1</sup> (MHz)	HITRAN [113] (MHz)	HITRAN Uncertainty code <sup>2</sup>	Observed- HITRAN (MHz)
30	5	25	31	6	26	90,145,138.1(13)	90,145,136.00	5	2.1
27	5	23	28	6	22	90,203,826.6(15)	90,203,828.50	5	-1.9
9	9	0	10	10	1	90,241,494.0(10)	90,241,492.70	5	1.3
9	9	1	10	10	0	90,241,494.0(10)	90,241,492.70	4	1.3
14	11	3	14	12	2	90,290,874.2(11)	90,290,873.50	5	0.7
22	5	18	23	6	17	90,488,885.7(4)	90,488,886.60	4	-0.9
13	7	7	14	8	6	90,505,566.7(7)	90,505,567.80	4	-1.1
13	7	6	14	8	7	90,505,566.7(7)	90,505,567.80	4	-1.1
11	7	4	12	8	5	90,617,974.5(5)	90,617,973.10	5	1.4
11	7	5	12	8	4	90,617,974.5(5)	90,617,973.10	5	1.4
12	6	6	13	7	7	90,804,714.4(5)	90,804,715.00	5	-0.6
12	6	7	13	7	6	90,804,714.4(5)	90,804,715.00	5	-0.6
7	7	0	8	8	1	90,841,672.7(4)	90,841,672.00	5	0.7
7	7	1	8	8	0	90,841,672.7(4)	90,841,672.00	5	0.7
14	5	9	15	6	10	90,934,841.8(4)	90,934,841.10	5	0.7
14	5	10	15	6	9	90,934,841.8(4)	90,934,841.10	5	0.7
9	6	4	10	7	3	90,972,817.7(6)	90,972,818.70	5	-1.0
9	6	3	10	7	4	90,972,817.7(6)	90,972,818.70	5	-1.0
10	5	6	11	6	5	91,158,744.6(3)	91,158,745.30	5	-0.7
10	5	5	11	6	6	91,158,744.6(3)	91,158,745.30	5	-0.7
8	5	3	9	6	4	91,270,517.1(5)	91,270,517.40	5	-0.3
8	5	4	9	6	3	91,270,517.1(5)	91,270,517.40	5	-0.3
7	5	3	8	6	2	91,326,294.4(4)	91,326,295.90	5	-1.5
7	5	2	8	6	3	91,326,294.4(4)	91,326,295.90	5	-1.5
12	3	10	13	4	9	91,381,981.3(6)	91,381,982.30	5	-1.0
6	5	2	7	6	1	91,381,981.3(6)	91,381,982.30	5	-1.0
6	5	1	7	6	2	91,381,981.3(6)	91,381,982.30	5	-1.0
5	5	0	6	6	1	91,437,566.8(5)	91,437,568.20	5	-1.4
5	5	1	6	6	0	91,437,566.8(5)	91,437,568.20	5	-1.4
14	3	11	15	4	12	91,448,049.2(7)	91,448,048.70	5	0.5
9	4	6	10	5	5	91,455,688.0(5)	91,455,688.60	5	-0.6
9	4	5	10	5	6	91,455,688.0(5)	91,455,688.60	5	-0.6
13	3	11	14	4	10	91,466,218.2(5)	91,466,218.20	5	0.0

The  $\nu_9$  band of  $\text{C}_2\text{H}_4$  (Continued on next page)<sup>1</sup>The number within parentheses is the statistical uncertainty in units of the last digit.<sup>2</sup>The HITRAN uncertainty code: “4” represents an uncertainty of 3–30 MHz, and “5” for an uncertainty of 0.3–3 MHz.

Table B.3 The  $\nu_9$  band of  $C_2H_4$  (continued from previous page)

$J'$	$K'_a$	$K'_c$	$J''$	$K''_a$	$K''_c$	Observed (MHz)	HITRAN [113] (MHz)	HITRAN Uncertainty code	Observed- HITRAN (MHz)
12	3	9	13	4	10	91,542,541.7(4)	91,542,542.70	5	-1
11	3	9	12	4	8	91,582,780.9(5)	91,582,782.80	5	-1.9
10	3	7	11	4	8	91,645,718.5(5)	91,645,719.60	5	-1.1
5	4	1	6	5	2	91,678,399.7(5)	91,678,400.60	5	-0.9
5	4	2	6	5	1	91,678,399.7(5)	91,678,400.60	5	-0.9
9	3	6	10	4	7	91,699,317.2(5)	91,699,317.20	4	0.0
8	3	6	9	4	5	91,752,123.1(4)	91,752,125.40	4	-2.3
8	3	5	9	4	6	91,753,719.3(7)	91,753,719.60	5	-0.3
22	1	21	23	2	22	91,816,985.4(7)	91,816,985.80	5	-0.4
21	1	21	22	0	22	91,944,686.5(7)	91,944,687.80	5	-1.3
4	3	2	5	4	1	91,974,151.5(7)	91,974,152.40	5	-0.9
4	3	1	5	4	2	91,974,151.5(7)	91,974,152.40	5	-0.9
18	1	17	19	2	18	91,992,030.6(6)	91,992,028.60	5	2.0
17	4	13	17	5	12	92,0125,76.5(4)	92,012,576.40	5	0.1
8	2	6	9	3	7	92,0125,76.5(4)	92,012,576.40	5	0.1
3	3	1	4	4	0	92,029,146.0(4)	92,029,144.10	5	1.9
3	3	0	4	4	1	92,029,146.0(4)	92,029,144.10	5	1.9
16	1	15	17	2	16	92,075,518.5(4)	92,075,517.90	5	0.6
18	1	18	19	0	19	92,100,984.1(7)	92,100,983.30	5	0.8
21	1	21	21	2	20	92,116,625.2(7)	92,116,624.60	4	0.6
20	8	12	19	9	11	92,116,625.2(7)	92,116,624.60	4	0.6
14	1	13	15	2	14	92,125,954.2(5)	92,125,954.70	5	-0.5
23	3	21	23	4	20	92,132,303.3(10)	92,132,302.70	4	0.6
17	0	17	18	1	18	92,146,547.7(3)	92,146,548.80	5	-1.1
16	2	15	17	1	16	92,227,258.9(5)	92,227,258.40	4	0.5
16	3	14	16	4	13	92,228,635.5(6)	92,228,634.90	4	0.6
14	3	12	14	4	11	92,237,963.8(7)	92,237,965.10	4	-1.3
10	3	7	10	4	6	92,251,132.9(6)	92,251,133.90	5	-1.0
10	1	9	11	2	10	92,253,060.9(5)	92,253,059.80	5	1.1
13	3	10	13	4	9	92,264,727.6(5)	92,264,730.20	5	-2.6
14	0	14	15	1	15	92,294,681.1(6)	92,294,682.00	5	-0.9
8	1	7	9	2	8	92,320,120.5(5)	92,320,121.20	5	-0.7
18	3	15	18	4	14	92,333,451.6(4)	92,333,450.90	5	0.7
13	0	13	14	1	14	92,342,681.9(3)	92,342,682.20	5	-0.3
5	1	5	6	2	4	92,345,453.3(4)	92,345,453.20	5	0.1
16	2	15	16	3	14	92,362,725.9(5)	92,362,724.30	4	1.6
20	3	17	20	4	16	92,373,453.8(4)	92,373,452.90	5	0.9

The  $\nu_9$  band of  $C_2H_4$  (Continued on next page)

Table B.3 The  $\nu_9$  band of  $C_2H_4$  (continued from previous page)

$J'$	$K'_a$	$K'_c$	$J''$	$K''_a$	$K''_c$	Observed (MHz)	HITRAN [113] (MHz)	HITRAN Uncertainty code	Observed- HITRAN (MHz)
17	3	15	18	2	16	92,381,896.5(4)	92,381,896.10	4	0.4
22	3	19	22	4	18	92,410,178.7(5)	92,410,179.70	5	-1.0
12	1	12	13	0	13	92,421,036.1(5)	92,421,036.50	5	-0.4
24	3	21	24	4	20	92,433,606.8(5)	92,433,607.70	4	-0.9
20	1	19	20	2	18	92,451,258.6(6)	92,451,258.50	5	0.1
9	2	8	9	3	7	92,468,294.6(5)	92,468,293.40	4	1.2
5	2	3	5	3	2	92,490,658.3(5)	92,490,658.40	4	-0.1
8	2	6	8	3	5	92,506,436.7(5)	92,506,436.50	4	0.2
9	0	9	10	1	10	92,512,229.0(4)	92,512,229.60	4	-0.6
11	2	9	11	3	8	92,541,615.5(5)	92,541,616.30	5	-0.8
19	6	13	18	7	12	92,556,228.0(7)	92,556,229.70	5	-1.7
19	6	14	18	7	11	92,556,228.0(7)	92,556,229.70	5	-1.7
12	2	10	12	3	9	92,556,228.0(7)	92,556,229.70	5	-1.7
8	0	8	9	1	9	92,557,675.5(4)	92,557,675.50	5	0.0
14	0	14	14	1	13	92,557,675.5(4)	92,557,675.50	5	0.0
15	3	13	16	2	14	92,562,611.3(6)	92,562,611.60	4	-0.3
18	1	17	18	2	16	92,564,606.7(4)	92,564,607.20	5	-0.5
15	2	13	15	3	12	92,595,862.4(6)	92,595,862.70	5	-0.3
9	1	9	9	2	8	92,601,550.8(4)	92,601,551.50	5	-0.7
16	2	14	16	3	13	92,603,961.2(5)	92,603,960.80	5	0.4
1	1	1	2	2	0	92,613,894.3(6)	92,613,894.60	5	-0.3
13	0	13	13	1	12	92,615,305.6(4)	92,615,305.50	5	0.1
17	1	16	17	2	15	92,615,305.6(4)	92,615,305.50	5	0.1
7	1	7	7	2	6	92,649,126.2(6)	92,649,126.50	5	-0.3
8	1	8	9	0	9	92,653,466.8(5)	92,653,468.30	5	-1.5
16	1	15	16	2	14	92,664,936.7(8)	92,664,937.30	5	-0.6
6	1	6	6	2	5	92,668,638.3(9)	92,668,638.90	4	-0.6
12	0	12	12	1	11	92,670,328.5(6)	92,670,327.20	4	1.3
15	1	14	15	2	13	92,682,373.2(3)	92,682,374.90	5	-1.7
5	0	5	6	1	6	92,683,402.1(3)	92,683,401.50	5	0.6
5	1	5	5	2	4	92,685,294.6(3)	92,685,294.30	5	0.3
6	1	6	7	0	7	92,777,792.3(9)	92,777,792.80	5	-0.5
9	0	9	9	1	8	92,798,928.6(4)	92,798,929.40	5	-0.8
6	0	6	6	1	5	92,896,963.1(7)	92,896,962.90	5	0.2
3	0	3	3	1	2	92,946,537.2(4)	92,946,538.40	5	-1.2
26	6	20	25	7	19	92,946,537.2(4)	92,946,538.40	5	-1.2
2	0	2	2	1	1	92,955,328.6(5)	92,955,329.10	5	-0.5

The  $\nu_9$  band of  $C_2H_4$  (Continued on next page)

Table B.3 The  $\nu_9$  band of  $C_2H_4$  (continued from previous page)

$J'$	$K'_a$	$K'_c$	$J''$	$K''_a$	$K''_c$	Observed (MHz)	HITRAN [113] (MHz)	HITRAN Uncertainty code	Observed- HITRAN (MHz)
9	3	7	10	2	8	93,061,301.1(11)	93,061,302.90	4	-1.8
12	2	11	11	3	8	93,088,909.9(10)	93,088,908.20	4	1.7
17	5	13	18	4	14	93,088,909.9(10)	93,088,908.20	4	1.7
2	1	1	2	0	2	93,207,350.0(8)	93,207,349.50	5	0.5
5	1	4	5	0	5	93,241,663.2(9)	93,241,661.30	5	1.9
8	1	7	7	2	6	93,246,963.8(9)	93,246,965.10	5	-1.3
9	1	8	9	0	9	93,346,825.1(15)	93,346,826.60	5	-1.5
3	1	3	2	0	2	93,348,398.5(12)	93,348,398.30	5	0.2
11	2	9	11	1	10	93,374,059.8(15)	93,374,058.90	5	0.9
6	2	4	6	1	5	93,391,156.7(11)	93,391,157.50	5	-0.8
13	2	11	13	1	12	93,396,572.3(14)	93,396,572.00	5	0.3
10	2	9	10	1	10	93,416,316.3(15)	93,416,317.60	5	-1.3
14	2	12	14	1	13	93,416,316.3(15)	93,416,317.60	5	-1.3
8	0	8	7	1	7	93,438,457.9(10)	93,438,459.00	5	-1.1
15	2	13	15	1	14	93,442,115.3(11)	93,442,115.60	5	-0.3
11	1	10	10	2	9	93,468,705.0(13)	93,468,703.60	4	1.4
16	2	14	16	1	15	93,474,108.6(16)	93,474,109.20	5	-0.6
17	3	14	17	2	15	93,509,212.2(13)	93,509,213.20	5	-1.0
6	3	3	6	2	4	93,509,212.2(13)	93,509,213.20	5	-1.0
17	2	15	17	1	16	93,512,027.6(15)	93,512,029.00	5	-1.4
22	3	19	22	2	20	93,552,571.9(15)	93,552,572.00	5	-0.1
19	2	17	19	1	18	93,603,913.1(11)	93,603,913.00	4	0.1
26	4	22	26	3	23	93,621,545.2(12)	93,621,543.20	5	2.0
11	0	11	10	1	10	93,621,545.2(12)	93,621,543.20	5	2.0
7	3	4	7	2	5	93,652,428.6(12)	93,652,430.00	5	-1.4
25	3	22	25	2	23	93,659,313.7(14)	93,659,313.40	5	0.3
6	3	3	6	2	4	93,659,313.7(14)	93,659,313.40	5	0.3
4	2	2	3	1	3	93,671,509.7(12)	93,671,509.90	4	-0.2
14	1	14	13	0	13	93,805,078.5(11)	93,805,077.80	5	0.7
17	2	16	17	1	17	93,821,957.0(13)	93,821,957.10	5	-0.1
19	4	16	19	3	17	93,900,876.3(16)	93,900,876.00	5	0.3
23	10	13	24	9	16	93,900,876.3(16)	93,900,876.00	5	0.3

Table B.4: Line list of the  $\nu_{11}$  band of Ethylene ( $^{12}\text{C}_2\text{H}_4$ ).

$J'$	$K'_a$	$K'_c$	$J''$	$K''_a$	$K''_c$	Observed <sup>1</sup> (MHz)	[128] <sup>2</sup> (MHz)	[113] (MHz)	code <sup>3</sup>	Obs- [128] (MHz)	Obs- [113] (MHz)
5	2	3	4	2	2	89,872,664.7(13)	89,872,664.40	89,872,664.30	5	0.3	0.4
6	0	6	5	0	5	89,918,378.0(12)	89,918,382.80	89,918,377.80	5	-4.8	0.2
6	2	4	5	2	3	89,929,211.4(15)	89,929,214.30	89,929,212.60	5	-2.9	-1.2
7	1	7	6	1	6	89,956,996.1(11)	89,956,993.10	89,956,995.90	5	3.0	0.2
7	2	5	6	2	4	89,986,396.2(12)	89,986,393.70	89,986,396.50	5	2.5	-0.3
7	1	6	6	1	5	89,995,481.3(11)	89,995,483.40	89,995,483.80	5	-2.1	-2.5
8	1	8	7	1	7	90,007,123.0(14)	90,007,121.40	90,007,123.10	5	1.6	-0.1
8	4	5	7	4	4	90,031,050.5(12)	90,031,044.80	90,031,048.90	5	5.7	1.6
8	4	4	7	4	3	90,031,050.5(12)	90,031,044.80	90,031,048.90	5	5.7	1.6
9	6	4	8	6	3	90,080,014.9(15)	90,080,015.90	90,080,014.90	5	-1.0	0.0
9	6	3	8	6	2	90,080,014.9(15)	90,080,015.90	90,080,014.90	5	-1.0	0.0
9	2	8	8	2	7	90,082,992.6(13)	90,082,986.80	90,082,992.50	5	5.8	0.1
9	5	5	8	5	4	90,082,992.6(13)	90,082,986.80	-	-	5.8	-
9	5	4	8	5	3	90,082,992.6(13)	90,082,986.80	90,082,992.50	5	5.8	0.1
9	3	7	8	3	6	90,087,615.3(12)	90,087,609.60	90,087,615.20	5	5.7	0.1
10	0	10	9	0	9	90,115,740.1(11)	90,115,742.20	90,115,740.20	5	-2.1	-0.1
10	5	5	9	5	4	90,137,385.7(14)	90,137,387.20	90,137,387.30	5	-1.5	-1.6
10	5	6	9	5	5	90,137,385.7(14)	90,137,387.20	90,137,387.30	5	-1.5	-1.6
10	3	8	9	3	7	90,142,150.6(12)	90,142,150.90	90,142,151.80	5	-0.3	-1.2
10	3	7	9	3	6	90,145,138.1(13)	90,145,133.80	90,145,136.00	5	4.3	2.1
11	1	11	10	1	10	90,155,211.0(12)	90,155,206.80	90,155,210.10	5	4.2	0.9
15	8	7	14	8	6	90,155,211.0(12)	-	90,155,210.10	5	-	0.9
11	5	7	10	5	6	90,191,767.2(14)	90,191,763.50	90,191,767.00	5	3.7	0.2
11	5	6	10	5	5	90,191,767.2(14)	90,191,763.50	90,191,767.00	5	3.7	0.2
11	3	8	10	3	7	90,201,378.4(11)	90,201,374.90	90,201,378.70	5	3.5	-0.3
12	1	12	11	1	11	90,203,826.6(15)	90,203,824.20	90,203,828.50	5	2.4	-1.9
12	5	8	11	5	7	90,246,150.2(10)	90,246,154.90	90,246,152.80	5	-4.7	-2.6
12	5	7	11	5	6	90,246,150.2(10)	90,246,154.90	90,246,152.80	5	-4.7	-2.6
12	3	10	11	3	9	90,250,873.4(14)	90,250,876.60	90,250,873.80	5	-3.2	-0.4
13	1	13	12	1	12	90,252,093.8(9)	90,252,090.80	90,252,093.70	5	3.0	0.1
12	1	11	11	1	10	90,265,976.5(8)	90,265,977.20	90,265,979.30	5	-0.7	-2.8
13	2	12	12	2	11	90,290,874.2(11)	90,290,877.90	90,290,873.50	5	-3.7	0.7

The  $\nu_{11}$  band of  $\text{C}_2\text{H}_4$  (Continued on next page)<sup>1</sup>The number within parentheses is the statistical uncertainty in units of the last digit.<sup>2</sup>The uncertainty of the line positions in [128] is 18 MHz.<sup>3</sup>The HITRAN uncertainty code: “4” represents an uncertainty of 3–30 MHz, and “5” for an uncertainty of 0.3–3 MHz.

Table B.4 Line list of the  $\nu_{11}$  band of  $C_2H_4$  (continued from previous page)

$J'$	$K'_a$	$K'_c$	$J''$	$K''_a$	$K''_c$	Observed (MHz)	[128] (MHz)	[113] (MHz)	code	Obs- [128] (MHz)	Obs- [113] (MHz)
13	2	11	12	2	10	90,335,089.2(12)	90,335,085.30	90,335,091.60	5	3.9	-2.4
14	3	12	13	3	11	90,358,760.6(8)	90,358,753.90	90,358,758.50	5	6.7	2.1
14	4	11	13	4	10	90,358,760.6(8)	-	90,358,758.50	5	-	2.1
14	4	10	13	4	9	90,360,020.2(7)	90,360,019.10	90,360,021.10	5	1.1	-0.9
15	8	7	14	8	6	90,396,271.8(6)	-	90,396,273.40	5	-	-1.6
15	8	8	14	8	7	90,396,271.8(6)	-	90,396,273.40	5	-	-1.6
16	7	10	15	7	9	90,454,947.7(7)	90,454,948.30	90,454,947.90	4	-0.6	-0.2
16	7	9	15	7	8	90,454,947.7(7)	90,454,948.30	90,454,947.90	4	-0.6	-0.2
16	4	12	15	4	11	90,471,297.6(6)	90,471,299.00	90,471,298.00	4	-1.4	-0.4
18	1	18	17	1	17	90,488,885.7(4)	90,488,884.80	90,488,886.60	4	0.9	-0.9
18	0	18	17	0	17	90,490,261.5(4)	90,490,260.90	90,490,262.00	4	0.6	-0.5
17	10	7	16	10	6	90,490,261.5(4)	-	90,490,262.00	4	-	-0.5
17	1	16	16	1	15	90,511,306.5(5)	90,511,306.30	90,511,307.60	4	0.2	-1.1
17	6	11	16	6	10	90,513,614.0(5)	90,513,614.70	90,513,615.20	4	-0.7	-1.2
17	6	12	16	6	11	90,513,614.0(5)	90,513,614.70	90,513,615.20	4	-0.7	-1.2
17	2	15	16	2	14	90,558,601.2(4)	90,558,598.60	90,558,603.50	4	2.6	-2.3
18	6	13	17	6	12	90,567,810.6(4)	90,567,808.20	90,567,811.00	4	2.4	-0.4
18	6	12	17	6	11	90,567,810.6(4)	90,567,808.20	90,567,811.00	4	2.4	-0.4
18	3	16	17	3	15	90,570,737.4(5)	90,570,737.20	90,570,736.00	4	0.2	1.4
18	4	15	17	4	14	90,577,085.2(7)	90,577,080.80	90,577,084.70	5	4.4	0.5
20	1	20	19	1	19	90,581,793.1(4)	90,581,796.50	90,581,794.80	4	-3.4	-1.7
20	0	20	19	0	19	90,582,535.2(4)	90,582,531.00	90,582,535.20	4	4.2	0.0
18	4	14	17	4	13	90,584,311.5(5)	90,584,314.80	90,584,310.90	4	-3.3	0.6
19	8	11	18	8	10	90,611,154.4(10)	90,611,155.20	90,611,154.00	4	-0.8	0.4
19	8	12	18	8	11	90,611,154.4(10)	90,611,155.20	90,611,154.00	4	-0.8	0.4
18	2	16	17	2	15	90,612,029.8(7)	90,612,030.60	90,612,029.30	5	-0.8	0.5
19	7	12	18	7	11	90,616,798.7(11)	-	90,616,798.50	5	-	0.2
19	7	13	18	7	12	90,616,798.7(11)	-	90,616,798.50	5	-	0.2
19	4	15	18	4	14	90,641,686.3(5)	90,641,686.10	90,641,686.80	5	0.2	-0.5
22	2	21	21	2	20	90,731,305.1(11)	-	90,731,305.50	5	-	-0.4
28	1	28	27	1	27	90,944,969.0(5)	-	90,944,969.70	5	-	-0.7
28	0	28	27	0	27	90,944,969.0(5)	-	90,944,969.70	5	-	-0.7
29	1	29	28	1	28	90,989,457.7(4)	-	90,989,456.60	4	-	1.1
29	0	29	28	0	28	90,989,457.7(4)	-	90,989,456.60	4	-	1.1
25	4	21	24	4	20	90,998,618.1(6)	-	90,998,619.40	4	-	-1.3
30	3	28	29	3	27	91,158,744.6(3)	-	91,158,745.30	5	-	-0.7

Table B.5: Line list of the  $\nu_2 + \nu_{12}$  band of Ethylene ( $^{12}\text{C}_2\text{H}_4$ ).

$J'$	$K'_a$	$K'_c$	$J''$	$K''_a$	$K''_c$	Observed (MHz)	HITRAN [113] (MHz)	HITRAN Uncertainty code	Observed- HITRAN (MHz)
15	8	7	15	8	8	91,992,030.6(6)	91,992,028.60	5	2.0
8	4	5	8	4	4	92,229,597.2(6)	92,229,597.20	4	0.0
8	4	4	8	4	5	92,229,597.2(6)	92,229,597.20	4	0.0
5	4	2	5	4	1	92,239,740.7(5)	92,239,741.60	5	-0.9
5	4	1	5	4	2	92,239,740.7(5)	92,239,741.60	5	-0.9
13	3	11	13	4	10	92,240,923.3(6)	92,240,923.70	5	-0.4
5	0	5	4	0	4	92,555,340.0(6)	92,555,341.40	4	-1.4
7	1	7	6	1	6	92,641,916.3(4)	92,641,916.40	5	-0.1
8	4	5	7	4	4	92,669,319.3(7)	92,669,319.60	4	-0.3
8	4	4	7	4	3	92,669,319.3(7)	92,669,319.60	4	-0.3
11	4	7	10	4	6	92,820,758.8(7)	92,820,759.30	4	-0.5
11	4	8	10	4	7	92,820,758.8(7)	92,820,759.30	4	-0.5
14	2	13	13	2	12	92,992,298.2(7)	92,992,298.30	4	-0.1
15	1	14	14	1	13	93,061,301.1(11)	93,061,302.90	4	-1.8

Table B.6: Line positions of the  $2\nu_{10} + \nu_{12}$  band of  $^{12}\text{C}_2\text{H}_4$ .

$J'$	$K'_a$	$K'_c$	$J''$	$K''_a$	$K''_c$	Observed (MHz)	HITRAN [113] (MHz)	HITRAN Uncertainty code	Observed- HITRAN (MHz)
16	4	13	17	4	14	91,992,030.6 (6)	91,992,028.60	5	2.0
5	5	0	6	5	1	92,641,916.3 (4)	92,641,916.40	5	-0.1
1	0	1	2	0	2	92,955,328.6 (5)	92,955,329.10	5	-0.5

# Bibliography

- [1] P. F. Bernath. *Spectra of Atoms and Molecules, Third Edition*. Oxford University Press, New York, 2016.
- [2] R. K. Altmann, L. S. Dreissen, E. J. Salumbides, W. Ubachs, and K. S. E. Eikema. Deep-Ultraviolet Frequency Metrology of H<sub>2</sub> for Tests of Molecular Quantum Theory. *Phys. Rev. Lett.*, 120:043204, 2018.
- [3] B. Spaun, P. B. Changala, D. Patterson, B. J. Bjork, Oliver Hubert Heckl, J. M. Doyle, and J. Ye. Continuous probing of cold complex molecules with infrared frequency comb spectroscopy. *Nature*, 533:517–520, 2016.
- [4] T. W. Hänsch. Nobel Lecture: Passion for precision. *Rev. Mod. Phys.*, 78:1297–1309, 2006.
- [5] Th. Udem, R. Holzwarth, and T. W. Hänsch. Optical Frequency Metrology. *Nature*, 17:233–237, 2002.
- [6] Th. Udem, J. Reichert, R. Holzwarth, and T. W. Hänsch. Absolute Optical Frequency Measurement of the Cesium  $D_1$  Line with a Mode-Locked Laser. *Phys. Rev. Lett.*, 82:3568–3571, 1999.
- [7] S. A. Diddams, J. C. Bergquist, S. R. Jefferts, and C. W. Oates. Standards of Time and Frequency at the Outset of the 21st Century. *Science*, 306:1318–1324, 2004.
- [8] T. Steinmetz, T. Wilken, C. A. Hauck, R. Holzwarth, T. W. Hänsch, L. Pasquini, A. Manescau, S. D’Odorico, M. T. Murphy, T. Kentischer, W. Schmidt, and Th. Udem. Laser Frequency Combs for Astronomical Observations. *Science*, 321:1335–1337, 2008.
- [9] S. T. Cundiff and A. M. Weiner. Optical arbitrary waveform generation. *Nat. Photonics*, 4:760–766, 2010.

- [10] A. Baltuska, Th. Udem, M. Uiberacker, M. Hentschel, E. Goulielmakis, C. Gohle, R. Holzwarth, Vladislav S. Yakovlev, A. Scrinzi, T. W. Hänsch, and F. Krausz. Attosecond control of electronic processes by intense light fields. *Nature*, 421:611–615, 2003.
- [11] N. Picqué and T. W. Hänsch. Frequency comb spectroscopy. *Nat. Photonics*, 13:146–157, 2019.
- [12] F. Keilmann, C. Gohle, and R. Holzwarth. Time-domain mid-infrared frequency-comb spectrometer. *Opt. Lett.*, 29:1542–1544, 2004.
- [13] M. J. Thorpe, K. D. Moll, R. J. Jones, B. Safdi, and J. Ye. Broadband Cavity Ring-down Spectroscopy for Sensitive and Rapid Molecular Detection. *Science*, 311:1595–1599, 2006.
- [14] C. Gohle, B. Stein, A. Schliesser, Th. Udem, and T. W. Hänsch. Frequency Comb Vernier Spectroscopy for Broadband, High-Resolution, High-Sensitivity Absorption and Dispersion Spectra. *Phys. Rev. Lett.*, 99:263902, 2007.
- [15] S. A. Diddams, L. Hollberg, and V. Mbele. Molecular fingerprinting with the resolved modes of a femtosecond laser frequency comb. *Nature*, 445:627–630, 2007.
- [16] J. Mandon, G. Guelachvili, and N. Picqué. Fourier transform spectroscopy with a laser frequency comb. *Nat. Photonics*, 3:99–102, 2009.
- [17] I. Coddington, W. C. Swann, and N. R. Newbury. Coherent Multiheterodyne Spectroscopy Using Stabilized Optical Frequency Combs. *Phys. Rev. Lett.*, 100:013902, 2008.
- [18] B. Bernhardt, A. Ozawa, P. Jacquet, M. Jacquy, Y. Kobayashi, Th. Udem, R. Holzwarth, G. Guelachvili, N. Picqué, and T. W. Hänsch. Cavity-enhanced dual-comb spectroscopy. *Nat. Photonics*, 4:55–57, 2010.
- [19] B. J. Bjork, T. Q. Bui, O. H. Heckl, P. B. Changala, B. Spaun, P. Heu, D. Follman, C. Deutsch, G. D. Cole, M. Aspelmeyer, M. Okumura, and J. Ye. Direct frequency comb measurement of  $\text{OD} + \text{CO} \rightarrow \text{DOC O}$  kinetics. *Science*, 354:444–448, 2016.
- [20] N. Coluccelli, M. Cassinero, B. Redding, H. Cao, P. Laporta, and G. Galzerano. The optical frequency comb fibre spectrometer. *Nat. Commun.*, 7:12995, 2016.

- [21] G. Guelachvili. High-accuracy Doppler-limited  $10^6$  samples Fourier transform spectroscopy. *Appl. Opt.*, 17:1322–1326, 1978.
- [22] A. M. Zolot, F. R. Giorgetta, E. Baumann, J. W. Nicholson, W. C. Swann, I. Coddington, and N. R. Newbury. Direct-comb molecular spectroscopy with accurate, resolved comb teeth over 43 THz. *Opt. Lett.*, 37:638–640, 2012.
- [23] Z. Chen, M. Yan, T. W. Hänsch, and N. Picqué. A phase-stable dual-comb interferometer. *Nat. Commun.*, 9:3035, 2018.
- [24] A. Nitkowski, L. Chen, and M. Lipson. Cavity-enhanced on-chip absorption spectroscopy using microring resonators. *Opt. Express*, 16:11930–11936, 2008.
- [25] L. Tombez, E. J. Zhang, J. S. Orcutt, S. Kamlapurkar, and W. M. J. Green. Methane absorption spectroscopy on a silicon photonic chip. *Optica*, 4:1322–1325, 2017.
- [26] W-C. Lai, S. Chakravarty, X. Wang, C. Lin, and R. T. Chen. On-chip methane sensing by near-IR absorption signatures in a photonic crystal slot waveguide. *Opt. Lett.*, 36:984–986, 2011.
- [27] G. Pickrell, W. Peng, and A. Wang. Random-hole optical fiber evanescent-wave gas sensing. *Opt. Lett.*, 29:1476–1478, 2004.
- [28] J. Ye and S. T. Cundiff. *Femtosecond Optical Frequency Comb: Principle, Operation, and Applications*. Springer, New York, 2005.
- [29] L. C. Sinclair, I. Coddington, W. C. Swann, G. B. Rieker, A. Hati, K. Iwakuni, and N. R. Newbury. Operation of an optically coherent frequency comb outside the metrology lab. *Opt. Express*, 22:6996–7006, 2014.
- [30] C. Gohle, Th. Udem, M. Herrmann, J. Rauschenberger, R. Holzwarth, H. A. Schuessler, F. Krausz, and T. W. Hänsch. A frequency comb in the extreme ultraviolet. *Nature*, 436:234, 2005.
- [31] G. Porat, C. M. Heyl, S. B. Schoun, C. Benko, N. Dörre, K. L. Corwin, and J. Ye. Phase-matched extreme-ultraviolet frequency-comb generation. *Nat. Photonics*, 12:387–391, 2018.
- [32] A. Schliesser, N. Picqué, and T. W. Hänsch. Mid-infrared frequency combs. *Nat. Photonics*, 6:440–449, 2012.

- [33] L. Consolino, A. Taschin, P. Bartolini, S. Bartalini, P. Cancio, A. Tredicucci, H. E. Beere, D. A. Ritchie, R. Torre, M. S. Vitiello, and P. De Natale. Phase-locking to a free-space terahertz comb for metrological-grade terahertz lasers. *Nat. Commun.*, 3:1040, 2012.
- [34] N. R. Newbury. Searching for applications with a fine-tooth comb. *Nat. Photonics*, 5:186–188, 2011.
- [35] S. A. Meek, A. Hipke, G. Guelachvili, T. W. Hänsch, and N. Picqué. Doppler-free fourier transform spectroscopy. *Opt. Lett.*, 43:162–165, 2018.
- [36] P. R. Griffiths and J. A. de Haseth. *Fourier Transform Infrared Spectrometry*. John Wiley and Sons, Inc, Hoboken, NJ, 2007.
- [37] A. Foltynowicz, T. Ban, P. Masłowski, F. Adler, and J. Ye. Quantum-noise-limited optical frequency comb spectroscopy. *Phys. Rev. Lett.*, 107:233002, 2011.
- [38] S. J. Lee, B. Widiyatmoko, M. Kouroggi, and M. Ohtsu. Ultrahigh scanning speed optical coherence tomography using optical frequency comb generators. *Jpn. J. Appl. Phys.*, 40:3–6, 2001.
- [39] T. Ideguchi, S. Holzner, B. Bernhardt, G. Guelachvili, N. Picqué, and T. W. Hänsch. Coherent Raman spectro-imaging with laser frequency combs. *Nature*, 502:355–358, 2013.
- [40] K. J. Mohler, B. J. Bohn, M. Yan, G. Mélen, T. W. Hänsch, and N. Picqué. Dual-comb coherent Raman spectroscopy with lasers of 1-GHz pulse repetition frequency. *Opt. Lett.*, 42:318–321, 2017.
- [41] A. Hipke, S. A. Meek, T. Ideguchi, T. W. Hänsch, and N. Picqué. Broadband Doppler-limited two-photon and stepwise excitation spectroscopy with laser frequency combs. *Phys. Rev. A*, 90:011805, 2014.
- [42] I. Coddington, N. Newbury, and W. Swann. Dual-comb spectroscopy. *Optica*, 3:414–426, 2016.
- [43] M. L. Weichman, P. B. Changala, J. Ye, Z. Chen, M. Yan, and N. Picqué. Broadband molecular spectroscopy with optical frequency combs. *J. Mol. Spectrosc.*, 355:66 – 78, 2019.

- [44] S. Okubo, K. Iwakuni, H. Inaba, K. Hosaka, A. Onae, H. Sasada, and F. Hong. Ultra-broadband dual-comb spectroscopy across 1.0–1.9  $\mu\text{m}$ . *Appl. Phys. Express*, 8:082402, 2015.
- [45] P. Giaccari, J. Deschênes, P. Saucier, J. Genest, and P. Tremblay. Active Fourier-transform spectroscopy combining the direct RF beating of two fiber-based mode-locked lasers with a novel referencing method. *Opt. Express*, 16:4347–4365, 2008.
- [46] J. Roy, J. Deschênes, S. Potvin, and J. Genest. Continuous real-time correction and averaging for frequency comb interferometry. *Opt. Express*, 20:21932–21939, 2012.
- [47] T. Ideguchi, A. Poisson, G. Guelachvili, T. W. Hänsch, and N. Picqué. Adaptive dual-comb spectroscopy in the green region. *Opt. Lett.*, 37:4847–4849, 2012.
- [48] T. Ideguchi, A. Poisson, G. Guelachvili, N. Picqué, and T. W. Hänsch. Adaptive real-time dual-comb spectroscopy. *Nat. Commun.*, 5:3375, 2014.
- [49] D. Burghoff, Y. Yang, and Q. Hu. Computational multiheterodyne spectroscopy. *Sci. Adv.*, 2:e1601227, 2016.
- [50] G. Millot, S. Pitois, M. Yan, T. Hovhannisyan, A. Bendahmane, T. W. Hänsch, and N. Picqué. Frequency-agile dual-comb spectroscopy. *Nat. Photonics*, 10:27–30, 2016.
- [51] A. J. Fleisher, D. A. Long, Z. D. Reed, J. T. Hodges, and D. F. Plusquellic. Coherent cavity-enhanced dual-comb spectroscopy. *Opt. Express*, 24:10424–10434, 2016.
- [52] X. Zhao, G. Hu, B. Zhao, C. Li, Y. Pan, Y. Liu, T. Yasui, and Z. Zheng. Picometer-resolution dual-comb spectroscopy with a free-running fiber laser. *Opt. Express*, 24:21833–21845, 2016.
- [53] S. M. Link, D. J. H. C. Maas, D. Waldburger, and U. Keller. Dual-comb spectroscopy of water vapor with a free-running semiconductor disk laser. *Science*, 356:1164–1168, 2017.
- [54] T. Ideguchi, T. Nakamura, Y. Kobayashi, and K. Goda. Kerr-lens mode-locked bidirectional dual-comb ring laser for broadband dual-comb spectroscopy. *Optica*, 3:748–753, 2016.
- [55] J. Nürnberg, C. G. E. Alfieri, Z. Chen, D. Waldburger, N. Picqué, and U. Keller. An unstabilized femtosecond semiconductor laser for dual-comb spectroscopy of acetylene. *Opt. Express*, 27:3190–3199, 2019.

- [56] G. B. Rieker, F. R. Giorgetta, W. C. Swann, J. Kofler, A. M. Zolot, L. C. Sinclair, E. Baumann, C. Cromer, G. Petron, C. Sweeney, P. P. Tans, I. Coddington, and N. R. Newbury. Frequency-comb-based remote sensing of greenhouse gases over kilometer air paths. *Optica*, 1:290–298, 2014.
- [57] K. C. Cossel, E. M. Waxman, F. R. Giorgetta, M. Cermak, I. R. Coddington, D. Heselius, S. Ruben, W. C. Swann, G. Truong, G. B. Rieker, and N. R. Newbury. Open-path dual-comb spectroscopy to an airborne retroreflector. *Optica*, 4:724–728, 2017.
- [58] B. Bernhardt, E. Sorokin, P. Jacquet, R. Thon, T. Becker, I. T. Sorokina, N. Picqué, and T. W. Hänsch. Mid-infrared dual-comb spectroscopy with 2.4  $\mu\text{m}$   $\text{Cr}^{2+}:\text{ZnSe}$  femtosecond lasers. *Appl. Phys. B*, 100:3–8, 2010.
- [59] Z. Zhang, T. Gardiner, and D. T. Reid. Mid-infrared dual-comb spectroscopy with an optical parametric oscillator. *Opt. Lett.*, 38:3148–3150, 2013.
- [60] A. Schliesser, M. Brehm, F. Keilmann, and D. W. van der Weide. Frequency-comb infrared spectrometer for rapid, remote chemical sensing. *Opt. Express*, 13:9029–9038, 2005.
- [61] G. Villares, A. Hugi, S. Blaser, and J. Faist. Dual-comb spectroscopy based on quantum-cascade-laser frequency combs. *Nat. Commun.*, 5:1–3, 2014.
- [62] E. Baumann, F. R. Giorgetta, W. C. Swann, A. M. Zolot, I. Coddington, and N. R. Newbury. Spectroscopy of the methane  $\nu_3$  band with an accurate midinfrared coherent dual-comb spectrometer. *Phys. Rev. A*, 84:062513, 2011.
- [63] M. Yan, P-L Luo, K. Iwakuni, G. Millot, T. W. Hänsch, and N. Picqué. Mid-infrared dual-comb spectroscopy with electro-optic modulators. *Light Sci. Appl.*, 6:e17076, 2017.
- [64] G. Ycas, F. R. Giorgetta., E Baumann, I Coddington, D. Herman, S. A. Diddams, and N. R. Newbury. High-coherence mid-infrared dual-comb spectroscopy spanning 2.6 to 5.2  $\mu\text{m}$ . *Nat. Photonics*, 12:1–7, 2018.
- [65] A. V. Muraviev, V. O. Smolski, Z. E. Loparo, and K. L. Vodopyanov. Massively parallel sensing of trace molecules and their isotopologues with broadband subharmonic mid-infrared frequency combs. *Nat. Photonics*, 12:209–214, 2018.
- [66] M. Yu, Y. Okawachi, A. G. Griffith, N. Picqué, M. Lipson, and A. L. Gaeta. Silicon-chip-based mid-infrared dual-comb spectroscopy. *Nat. Commun.*, 9:1869, 2018.

- [67] T. Yasui, Y. Kabetani, E. Saneyoshi, S. Yokoyama, and T. Araki. Terahertz frequency comb by multifrequency-heterodyning photoconductive detection for high-accuracy, high-resolution terahertz spectroscopy. *Appl. Phys. Lett.*, 88:241104, 2006.
- [68] Y. Yang, D. Burghoff, D. J. Hayton, J.-R. Gao, J. L. Reno, and Q. Hu. Terahertz multiheterodyne spectroscopy using laser frequency combs. *Optica*, 3:499–502, May 2016.
- [69] I. A. Finneran, J. T. Good, D. B. Holland, P. B. Carroll, M. A. Allodi, and G. A. Blake. Decade-spanning high-precision terahertz frequency comb. *Phys. Rev. Lett.*, 114:163902, 2015.
- [70] K. Rahmelow and W. Hübner. Phase correction in Fourier transform spectroscopy: subsequent displacement correction and error limit. *Appl. Opt.*, 36:6678–6686, 1997.
- [71] P. Raspollini, P. Ade, B. Carli, and M. Ridolfi. Correction of instrument line-shape distortions in fourier transform spectroscopy. *Appl. Opt.*, 37:3697–3704, 1998.
- [72] R. C. M. Learner, A. P. Thorne, and J. W. Brault. Ghosts and artifacts in fourier-transform spectrometry. *Appl. Opt.*, 35:2947–2954, 1996.
- [73] T. Ideguchi, B. Bernhardt, G. Guelachvili, T. W. Hänsch, and N. Picqué. Raman-induced kerr-effect dual-comb spectroscopy. *Opt. Lett.*, 37:4498–4500, 2012.
- [74] R. C. M. Learner, A. P. Thorne, I. Wynne-Jones, J. W. Brault, and M. C. Abrams. Phase correction of emission line fourier transform spectra. *J. Opt. Soc. Am. A*, 12:2165–2171, 1995.
- [75] G. Wu, M. Takahashi, K. Arai, H. Inaba, and K. Minoshima. Extremely high-Accuracy correction of air refractive index using two-colour optical frequency combs. *Sci. Rep.*, 3, 2013.
- [76] H. A. Haus and A. Mecozzi. Noise of mode-locked lasers. *IEEE J. Quantum Electron*, 29:983–996, 1993.
- [77] N. R. Newbury and W. C. Swann. Low-noise fiber-laser frequency combs (invited). *J. Opt. Soc. Am. B*, 24:1756–1770, 2007.
- [78] G. Guelachvili. *Distortions in Fourier spectra and diagnosis, Spectrometric Techniques II, Second Edition*. Academic Press, London, 1981.

- [79] G. Guelachvili. Distortion free interferograms in Fourier transform spectroscopy with nonlinear detectors. *Appl. Opt.*, 25:4644–4648, 1986.
- [80] L. Palchetti, G. Bianchini, U. Cortesi, E. Pascale, and C. Lee. Assessment of detector nonlinearity in fourier transform spectroscopy. *Appl. Spectrosc.*, 56:271–274, 2002.
- [81] N. R. Newbury, I. Coddington, and W. Swann. Sensitivity of coherent dual-comb spectroscopy. *Opt. Express*, 18:7929–7945, 2010.
- [82] Z. Chen, T. W. Hänsch, and N. Picqué. Mid-infrared feed-forward dual-comb spectroscopy. *Proc. Natl. Acad. Sci. USA*, 116:3454–3459, 2019.
- [83] J. L. Hall and T. W. Hänsch. External dye-laser frequency stabilizer. *Opt. Lett.*, 9:502–504, 1984.
- [84] R. J. Jones and J. Diels. Stabilization of femtosecond lasers for optical frequency metrology and direct optical to radio frequency synthesis. *Phys. Rev. Lett.*, 86:3288–3291, 2001.
- [85] S. Koke, H. Grebing, C. and Frei, A. Anderson, A. Assion, and G. Steinmeyer. Direct frequency comb synthesis with arbitrary offset and shot-noise-limited phase noise. *Nat. Photonics*, 4:462–465, 2010.
- [86] D. Gatti, T. Sala, A. Gambetta, N. Coluccelli, G. Nunzi Conti, G. Galzerano, P. Laporta, and M. Marangoni. Analysis of the feed-forward method for the referencing of a CW laser to a frequency comb. *Opt. Express*, 20:24880–24885, 2012.
- [87] W. C. Swann and S. L. Gilbert. Pressure-induced shift and broadening of 1510–1540-nm acetylene wavelength calibration lines. *J. Opt. Soc. Am. B*, 17:1263–1270, 2000.
- [88] K. Nakagawa, M. de Labachellerie, Y. Awaji, and M. Kourogi. Accurate optical frequency atlas of the 1.5- $\mu\text{m}$  bands of acetylene. *J. Opt. Soc. Am. B*, 13:2708–2714, 1996.
- [89] C. S. Edwards, G. P. Barwood, H. S. Margolis, P. Gill, and W. R. C. Rowley. High-precision frequency measurements of the  $\nu_1 + \nu_3$  combination band of  $^{12}\text{C}_2\text{H}_2$  in the 1.5  $\mu\text{m}$  region. *J. Mol. Spectrosc.*, 234:143 – 148, 2005.

- [90] O. M. Lyulin, V. I. Perevalov, I. Morino, T. Yokota, R. Kumazawa, and T. Watanabe. Measurements of self-broadening and self-pressure-induced shift parameters of the methane spectral lines in the 5556–6166  $\text{cm}^{-1}$  range. *J. Quant. Spectrosc. Radiat. Transf.*, 112:531–539, 2011.
- [91] C. Ishibashi, M. Kouroggi, K. Imai, B. Widiyatmoko, A. Onae, and H. Sasada. Absolute frequency measurement of the saturated absorption lines of methane in the 1.66  $\mu\text{m}$  region. *Optics Communications*, 161:223 – 226, 1999.
- [92] A. Hugi, G. Villares, S. Blaser, H. C. Liu, and J. Faist. Mid-infrared frequency comb based on a quantum cascade laser. *Nature*, 492:229–233, 2012.
- [93] M.-G. Suh, Q. Yang, K. Y. Yang, X. Yi, and K. J. Vahala. Microresonator soliton dual-comb spectroscopy. *Science*, 354:600–603, 2016.
- [94] J. Greener, B. Abbasi, and E. Kumacheva. Attenuated total reflection Fourier transform infrared spectroscopy for on-chip monitoring of solute concentrations. *Lab Chip*, 10:1561–1566, 2010.
- [95] H. N Holman, H. A. Bechtel, Z. Hao, and M. C. Martin. Synchrotron IR spectromicroscopy: Chemistry of living cells. *Anal. Chem.*, 82:8757–8765, 2010.
- [96] N. P. Mauranyapin, L. Madsen, M. A. Taylor, M. Waleed, and W. P. Bowen. Evanescent single-molecule biosensing with quantum limited precision. *Nat. Photonics*, 11:477–481, 2017.
- [97] D. Sofikitis, L. Bougas, G. E. Katsoprinakis, A. K. Spiliotis, B. Loppinet, and T. P. Rakitzis. Evanescent-wave and ambient chiral sensing by signal-reversing cavity ring-down polarimetry. *Nature*, 514:76, 2014.
- [98] R. Diekmann, Ø. I. Helle, C. I. Øie, Peter McCourt, Th. R. Huser, M. Schüttpelz, and B. S. Ahluwalia. Chip-based wide field-of-view nanoscopy. *Nat. Photonics*, 11:322–328, 2017.
- [99] T. H. Stievater, M. W. Pruessner, D. Park, W. S. Rabinovich, R. A. McGill, D. A. Kozak, R. Furstenberg, S. A. Holmstrom, and J. B. Khurgin. Trace gas absorption spectroscopy using functionalized microring resonators. *Opt. Lett.*, 39:969–972, 2014.
- [100] H. Tai, H. Tanaka, and T. Yoshino. Fiber-optic evanescent-wave methane-gas sensor using optical absorption for the 3.392- $\mu\text{m}$  line of a He–Ne laser. *Opt. Lett.*, 12:437–439, 1987.

- [101] C. J. Smith, R. Shankar, M. Laderer, M. B. Frish, M. Loncar, and M. G. Allen. Sensing nitrous oxide with QCL-coupled silicon-on-sapphire ring resonators. *Opt. Express*, 23:5491–5499, 2015.
- [102] L. Tong, R. R. Gattass, J. B. Ashcom, S. He, J. Lou, M. Shen, I. Maxwell, and E. Mazur. Subwavelength-diameter silica wires for low-loss optical wave guiding. *Nature*, 426:816, 2003.
- [103] L. Tong, J. Lou, and E. Mazur. Single-mode guiding properties of subwavelength-diameter silica and silicon wire waveguides. *Opt. Express*, 12:1025–1035, 2004.
- [104] F. L. Kien, J.Q. Liang, K. Hakuta, and V.I. Balykin. Field intensity distributions and polarization orientations in a vacuum-clad subwavelength-diameter optical fiber. *Opt. Commun.*, 242:445 – 455, 2004.
- [105] G. Brambilla, F. Xu, P. Horak, Y. Jung, F. Koizumi, N. P. Sessions, E. Koukharenko, X. Feng, G. S. Murugan, J. S. Wilkinson, and D. J. Richardson. Optical fiber nanowires and microwires: fabrication and applications. *Adv. Opt. Photon.*, 1:107–161, 2009.
- [106] F. Warken, E. Vetsch, D. Meschede, M. Sokolowski, and A. Rauschenbeutel. Ultra-sensitive surface absorption spectroscopy using sub-wavelength diameter optical fibers. *Opt. Express*, 15:11952–11958, 2007.
- [107] T. A. Birks, W. J. Wadsworth, and P. St. J. Russell. Supercontinuum generation in tapered fibers. *Opt. Lett.*, 25:1415–1417, 2000.
- [108] G. Sagué, E. Vetsch, W. Alt, D. Meschede, and A. Rauschenbeutel. Cold-atom physics using ultrathin optical fibers: Light-induced dipole forces and surface interactions. *Phys. Rev. Lett.*, 99:163602, 2007.
- [109] A. W. Snyder and J. D. Love. *Optical Waveguide Theory*. Chapman and Hall, New York, NY, 1983.
- [110] A. Yariv. *Optical Electronics*. CBS College, New York, 1985.
- [111] N. Punjabi, J. Satija, and S. Mukherji. *Evanescent Wave Absorption Based Fiber-Optic Sensor - Cascading of Bend and Tapered Geometry for Enhanced Sensitivity*, pages 25–45. Springer International Publishing, Cham, 2015.

- [112] V. M. Devi, D. C Benner, K. Sung, T. J. Crawford, S. Yu, Linda R. Brown, M. A. H. Smith, A. W. Mantz, V. Boudon, and S. Ismail. Self- and air-broadened line shapes in the  $2\nu_3$   $P$  and  $R$  branches of  $^{12}\text{CH}_4$ . *J. Mol. Spectrosc.*, 315:114 – 136, 2015.
- [113] I.E. Gordon, L.S. Rothman, C. Hill, R.V. Kochanov, Y. Tan, P.F. Bernath, M. Birk, V. Boudon, A. Campargue, K.V. Chance, B.J. Drouin, J.-M. Flaud, R.R. Gamache, J.T. Hodges, D. Jacquemart, V.I. Perevalov, A. Perrin, K.P. Shine, M.-A.H. Smith, J. Tennyson, G.C. Toon, H. Tran, V.G. Tyuterev, A. Barbe, A.G. Császár, V.M. Devi, T. Furtenbacher, J.J. Harrison, J.-M. Hartmann, A. Jolly, T.J. Johnson, T. Karman, I. Kleiner, A.A. Kyuberis, J. Loos, O.M. Lyulin, S.T. Massie, S.N. Mikhailenko, N. Moazzen-Ahmadi, H.S.P. Müller, O.V. Naumenko, A.V. Nikitin, O.L. Polyansky, M. Rey, M. Rotger, S.W. Sharpe, K. Sung, E. Starikova, S.A. Tashkun, J. Vander Auwera, G. Wagner, J. Wilzewski, P. Wcisło, S. Yu, and E.J. Zak. The HITRAN 2016 molecular spectroscopic database. *J. Quant. Spectrosc. Radiat. Transf.*, 203:3 – 69, 2017.
- [114] A. V. Nikitin, O. M. Lyulin, S. N. Mikhailenko, V. I. Perevalov, N. N. Filippov, I. M. Grigoriev, I. Morino, Y. Yoshida, and T. Matsunaga. Gosat-2014 methane spectral line list. *J. Quant. Spectrosc. Radiat. Transf.*, 154:63 – 71, 2015.
- [115] R. A. Alvarez, S. W. Pacala, J. J. Winebrake, W. L. Chameides, and S. P. Hamburg. Greater focus needed on methane leakage from natural gas infrastructure. *Proc. Natl. Acad. Sci. USA*, 109:6435–6440, 2012.
- [116] M. J. Thorpe, D. Balslev-Clausen, M. S. Kirchner, and J. Ye. Cavity-enhanced optical frequency comb spectroscopy: application to human breath analysis. *Opt. Express*, 16:2387–2397, 2008.
- [117] S. A. Meek, A. Poisson, G. Guelachvili, T. W. Hänsch, and N. Picqué. Fourier transform spectroscopy around  $3\ \mu\text{m}$  with a broad difference frequency comb. *Appl. Phys. B*, 114:573–578, 2014.
- [118] S. Duval, M. Bernier, V. Fortin, J. Genest, M. Piché, and R. Vallée. Femtosecond fiber lasers reach the mid-infrared. *Optica*, 2:623–626, 2015.
- [119] L. A. Sterczewski, J. Westberg, C. L. Patrick, C. S. Kim, M. Kim, C. L. Canedy, W. W. Bewley, C. D. Merritt, I. Vurgaftman, J. R. Meyer, and G. Wysocki. Multi-heterodyne spectroscopy using interband cascade lasers. *Opt. Eng.*, 57:1–12, 2017.

- [120] C. Y. Wang, T. Herr, P. Del’Haye, A. Schliesser, J. Hofer, R. Holzwarth, T. W. Hänsch, N. Picqué, and T. J. Kippenberg. Mid-infrared optical frequency combs at  $2.5\ \mu\text{m}$  based on crystalline microresonators. *Nat. Commun.*, 4, 2013.
- [121] J. Zhang, K. Mak, N. Nagl, M. Seidel, D. Bauer, D. Sutter, V. Pervak, F. Krausz, and O. Pronin. Multi-mW, few-cycle mid-infrared continuum spanning from 500 to  $2250\ \text{cm}^{-1}$ . *Light Sci. Appl.*, 7:17180, 2018.
- [122] C. S. Kumar, A. Esteban-Martin, T. Ideguchi, M. Yan, S. Holzner, T. W. Hänsch, N. Picqué, and M. Ebrahim-Zadeh. Few-cycle, broadband, mid-infrared optical parametric oscillator pumped by a 20-fs Ti:sapphire laser. *Laser Photonics Rev.*, 8:L86–L91, 2014.
- [123] B. Kuyken, T. Ideguchi, S. Holzner, M. Yan, T. W. Hänsch, J. Van Campenhout, P. Verheyen, S. Coen, F. Leo, R. Baets, G. Roelkens, and N. Picqué. An octave-spanning mid-infrared frequency comb generated in a silicon nanophotonic wire waveguide. *Nat. Commun.*, 6:1–6, 2015.
- [124] A. Hangauer, J. Westberg, E. Zhang, and G. Wysocki. Wavelength modulated multiheterodyne spectroscopy using Fabry-Perot quantum cascade lasers. *Opt. Express*, 24:25298–25307, 2016.
- [125] R. W. Boyd. *Nonlinear Optics*. Academic Press, San Diego, 2008.
- [126] J.-Y. Mandin, D. Jacquemart, V. Dana, L. Régalia-Jarlot, and A. Barbe. Line intensities of acetylene at  $3\ \mu\text{m}$ . *J. Quant. Spectrosc. Radiat. Transf.*, 92:239 – 260, 2005.
- [127] A. S. Pine. *Tunable Laser Survey of Molecular Air Pollutants*. Final Report NSF/ASRA/DAR 78-24562, MIT, Lexington, MA, 1980.
- [128] G. B. Lebron and T. L. Tan. High-resolution Fourier transform infrared spectrum of the  $\nu_{11}$  band of ethylene ( $^{12}\text{C}_2\text{H}_4$ ). *J. Mol. Spectrosc.*, 288:11–13, 2013.
- [129] P. G. Schunemann, K. T. Zawilski, L. A. Pomeranz, D. J. Creeden, and P. A. Budni. Advances in nonlinear optical crystals for mid-infrared coherent sources. *J. Opt. Soc. Am. B*, 33:D36–D43, 2016.
- [130] G. R. D. Prabhu and P. L. Urban. In-oleo microgasometry of nanoliter-scale gas volumes with image-based detection. *Anal. Chem.*, 88:11368–11372, 2016.

- 
- [131] A. Dutt, C. Joshi, X. Ji, J. Cardenas, Y. Okawachi, K. Luke, A. L. Gaeta, and M. Lipson. On-chip dual-comb source for spectroscopy. *Sci. Adv.*, 4, 2018.



# List of Publications

## **A phase-stable dual-comb interferometer**

Zaijun Chen, Ming Yan, Theodor W. Hänsch, Nathalie Picqué

Nature Communications **9**, 3035 (2018)

## **Mid-infrared feed-forward dual-comb spectroscopy**

Zaijun Chen, Theodor W. Hänsch, and Nathalie Picqué

Proceedings of the National Academy of Sciences of the United States of America **116**, 3454–3459 (2019)

## **Up-conversion mid-infrared dual-comb spectroscopy**

Zaijun Chen, Theodor W. Hänsch, and Nathalie Picqué

In preparation (2019)

## **A low-loss lithium-niobate electro-optic microring platform for spectrally tailored dual-comb spectroscopy**

Amirhassan Shams-Ansari\*, Mengjie Yu\*, Zaijun Chen\*, Christian Reimer, Mian Zhang, Nathalie Picqué, and Marko Loncar

In preparation (2019)

## **An unstabilized femtosecond semiconductor laser for dual-comb spectroscopy of acetylene**

Jacob Nürnberg, Cesare G. E. Alfieri, Zaijun Chen, Dominik Waldburger, Nathalie Picqué and Ursula Keller

Optics Express **27**, 3190–3199 (2019)

## **Broadband molecular spectroscopy with optical frequency combs**

Marissa L. Weichman, P. Bryan Changala, Jun Ye, Zaijun Chen, Ming Yan, and Nathalie Picqué

Journal of Molecular Spectroscopy **355**, 66–78 (2019)

**Dual-comb thin-disk oscillator**

Kilian Fritsch, Jonathan Brons, Maksim Ianduskii, Ka Fai Mak, Zaijun Chen, Nathalie Picqué, and Oleg Pronin

In preparation (2019)

# Conference Contributions

## **Dual-comb up-conversion detection of fundamental molecular transitions**

Zaijun Chen, Theodor W. Hänsch, and Nathalie Picqué

74-th International Symposium on Molecular Spectroscopy, Urbana, United States (2019).

## **Doppler-limited broadband dual-comb spectroscopy at 3 $\mu\text{m}$**

Zaijun Chen, Theodor W. Hänsch, and Nathalie Picqué

73-rd International Symposium on Molecular Spectroscopy (Mini-symposium: Frequency-Comb Spectroscopy), Urbana, United States (2018).

## **Mid-infrared Dual-Comb Spectroscopy at High Signal-to-Noise Ratio around 3 $\mu\text{m}$**

Zaijun Chen, Theodor W. Hänsch, and Nathalie Picqué

OSA Mid-Infrared Coherent Sources in High-Brightness Sources and Light-driven Interactions Congress, paper MW4C.6., Strasbourg, France (2018).

## **Evanescent-Wave Gas Sensing with Dual-Comb Spectroscopy**

Zaijun Chen, Ming Yan, Theodor W. Hänsch, and Nathalie Picqué

Conference on Lasers and Electro-Optics, paper SF1M.7, San Jose, United States (2017).

## **Feed-forward coherent dual-comb spectroscopy**

Zaijun Chen, Ming Yan, Gwenaëlle Mélen, Theodor W. Hänsch, and Nathalie Picqué

OSA Fourier Transform Spectroscopy in Light, Energy and the Environment Congress, Leipzig, Germany, paper FTh3B.6 (2016).

## **Microring Electro-optic Frequency Comb Sources for Dual-Comb Spectroscopy**

A. Shams-Ansari\*, M. Yu\*, Z. Chen\*, C. Reimer, M. Zhang, N. Picqué, and M. Loncar,

Conference on Lasers and Electro-Optics, paper JTh5B.8, San Jose, United States (2019).

**High-power dual-comb thin-disk oscillator**

Kilian Fritsch, Jonathan Brons, Maksim Ianduskii, Ka Fai Mak, Zaijun Chen, Ferenc Krausz, Nathalie Picqué, and Oleg Pronin

Conference on Lasers and Electro-Optics/Europe, CF-1: High-power oscillators, Munich, Germany (2019).

**Dual-comb spectroscopy of acetylene with a single, free-running MIXSEL generating two frequency combs**

J. Nürnberg, C. G. E. Alfieri, Z. Chen, D. Waldburger, M. Golling, N. Picqué, and U. Keller

Conference on Lasers and Electro-Optics/Europe, ED-3.2, Munich, Germany (2019).

**Free-running, Femtosecond Dual-Comb MIXSEL for Spectroscopy of Acetylene**

J. Nürnberg, C. G. E. Alfieri, Z. Chen, D. Waldburger, M. Golling, N. Picqué, and U. Keller

Conference on Lasers and Electro-Optics, San Jose, United States, paper JW2A.157 (2018).

**Dual-Comb Spectroscopy with one unstabilized semiconductor laser**

J. Nürnberg, C. G. E. Alfieri, Z. Chen, D. Waldburger, M. Golling, N. Picqué, and U. Keller

Advanced Photonics 2018, paper IM3I.1, Zurich, Switzerland (2018).

# Acknowledgements

To begin with, I sincerely thank **Prof. Theodor W. Hänsch** and **Dr. Nathalie Picqué** for the opportunity to join the wonderful research group at Max-Planck Institute of Quantum Optics, to participate in the exciting research projects and experiments, and to work with the outstanding colleagues and collaborators.

**Prof. Hänsch's** curiosity and passion for science have stimulated me all the time. His advice is always very insightful. I gained knowledge from each discussion with him. He always comes up with simple and elegant solutions to all the complications.

I have my best thanks to my direct supervisor, **Nathalie Picqué**, who gave me a great research topic to explore and provided numerous supports throughout the thesis. I am impressed by her precision to every detail. Her way of thinking and decision making is logical, and new ideas always come to her mind. I thank her for sharing her insightful view and knowledge with me. I have learned a lot from her, and we have made many memorable accomplishments together.

Special thanks go to **Ming Yan**, who guided me in the researches in the early stage of this thesis. It was a very enjoyable time when he was around. “Dr. Ming” was extremely resourceful in the lab. I learnt various sets of skill from him. Apart from the work, we became good friends. I enjoyed a lot having dinner at his place (his cooking skill is almost comparable to his lab skills). We shared many wonderful moments together, and I wish him the best luck for his future.

**Kana Iwakuni** and **Pei-Ling Luo** were another two excellent postdocs in the group. We shared the office during their stay at MPQ. They were always very thoughtful and kind to everybody. It was very nice working with them. I thank them for sharing their knowledge and experience with me.

**Arthur Hipke** and **Simon Holzner** were doctoral students approaching their graduation at the time when I joined the group. They are very talented and always very nice and helpful. Many thanks to them for teaching me and sharing their experience and experimental

skills with me.

What has been said to Arthur and Simon applies to **Bernhard Bohn** and **Kathrin Mohler**, another two PhD students who joined the group approximately at the same time as me. Bernhard and Kathrin are always very thoughtful and helpful. They cheered me up all the time when things were not going well. I enjoy the time working with them and best wishes to their future.

**Bart Kuyken** is another nice postdoc from whom I learned a lot. I thank him for sharing his insightful knowledge and techniques about chip-based waveguides and nonlinear optics with me. **Gwénaëlle Mélen** was another postdoc that I worked with. Her skill of making presentations is very impressive.

In the later stage of the thesis, **Jeonghyun Huh** and **Qiang Wang** joined the group as postdoc researchers. Both of them are very nice. I am glad that they were here. I enjoy a lot talking to them and Working together with them.

During this thesis, I was involved in several collaborations. All of them were very fruitful. Many thanks to our excellent collaborators for making everything happened. I enjoyed my visit to the group of professor **Ursula Keller** at ETH Zurich (Switzerland). The time working with **Jacob Nürnberg** and **Cesare Alfieri** in their lab in Zurich was a very good experience. The project with the group of Professor **Marko Loncar** at Harvard University (United States) is going well, and I enjoyed visiting his labs and working with **Amirhassan Shams-Ansari** and **Mengjie Yu**.

Besides, many thanks to the nice colleagues in the Hänsch group, **Akira Ozawa**, **Fabian Schmid**, **Lukas Knips**, and **Massaki Hori**, etc. Everyone in the group is very positive and always trying to help. The discussions with them were always very helpful.

I thank the mechanical engineers, **Wolfgang Simon** and **Karl Linner**, and the electrical engineer, **Helmut Brücker**, for their constant technical supports for all the experiments.

Many thanks to Ms. **Ingrid Hermann** and Ms. **Gabriele Gschwendtner** for their efficient administration work, which had made the life much earlier.

Finally I would like to thank my family and friends for their supports.